wellcome trust wellcome trust

An Ultrastructural Study of the Role of Clathrin as an Inter-Microtubule Bridge in Kinetochore Fibres

Daniel George Booth

ID: 200512334

University of Liverpool

Thesis submitted in accordance with the requirements of the University of Liverpool for the degree of Doctor in Philosophy

September 2011

Daniel George Booth

Abstract

The mitotic spindle is required for the accurate segregation of an equal number of chromosomes, into two separate daughter cells. The movement of chromosomes is carried out by kinetochore fibres (K-fibres) of the spindle apparatus, these extend from the cell pole and terminate at attachment on the kinetochore. K-fibres are composed of bundles of individual kinetochore microtubules (kMTs). Microtubule (MT) bundling is coordinated by inter-MT bridges, which are thought to promote MT stability and organisation. The inter-MT bridges in K-fibres have never been fully characterised.

Clathrin is a triskelion-structured protein with a well-characterised role in membrane trafficking, where it forms the 'coat' of clathrin-coated vesicles. More recently clathrin has been shown to have an unrelated function during mitosis: a period of the cell cycle when membrane trafficking is dormant. The depletion of clathrin by RNAi results in a number of mitotic defects, all of which are a consequence of destabilised K-fibres. It has been proposed that a TACC3/ch-TOG/clathrin complex physically cross-braces kMTs to stabilise K-fibres.

This project set-up correlative light electron microscopy (CLEM) methods allowing mitotic, clathrin-depleted cells to be analysed from the level of light microscopy to electron microcopy. A dual-axis ultrastructural methodology was also developed allowing K-fibre bundles and inter-MT bridges to be measured. This project used CLEM to reveal that a clathrin complex functions as a population of short inter-MT bridges in K-fibres. The depletion of clathrin or TACC3 resulted in:

1) a loss of kMTs, 2) a decrease in kMT organisation and 3) a loss of a population of short inter-kMT bridges. Immunogold labelling confirmed that clathrin was a component of the inter-kMT bridge.

The literature typically refer to inter-MT bridges as electron dense 'struts' that cross-link MTs, however, a few classic EM studies have described bridges as 'filamentous' with 'multiple projections'. A highly resolved view of bridge structures was sought. Using high-pressure freezing with freeze-substitution, tomography and 3D rendering, this project revealed that a novel structure was present that cross-linked kMTs, we have termed this structure 'inter-kMT mesh'. The mesh was found exclusively between kMTs and appeared to promote kMT organisation through multiple contacts with MTs. The mesh responded to manipulated levels of TACC3 expression, resulting in disorganised K-fibre bundles, misshapen kMTs and an enhanced electron-dense inter-kMT mesh.

Collectively, these new data contribute to the existing knowledge of inter-MT cross-linkers in K-fibres by providing novel insights into their structure and how they confer kMT stability and organisation.

Table of Contents

Acknowledgements

An ‘acknowledgements page’, the only section of this thesis that will have never come into contact with red pen. Firstly, I would like to thank my supervisors Ian Prior and Steve Royle. Steve has been enthusiastic and supportive throughout my PhD, continually providing help and advice whenever requested. Thankyou to all the members of my lab and the EM unit, past and present, particularly to Anna, Fi and Ali who have given me help, advice and cake many times over the last four years. I would also like to thank the various post-doc, PhD and masters students that I have become friends with during my PhD, particularly Rob Jenn, who has been a great friend, formidable beer drinking partner and average player of FIFA. Several non-scientists also need acknowledging, these would include: my parents, who have provided me with support before, during and hopefully after my time at university; my friends from back home, many of whom I have now known for nearly 25 years. They have provided me with a sanctuary away from my scientific bubble whenever I have needed it; and finally to my long-suffering girlfriend Gemma, who I love and adore, who has (mostly) never complained that we have only been on one holiday together during the last four years.

The acknowledgements will finish with two quotes; the first is thought-provoking in both a scientific context and life in general, the second is a quote that has provided me with comfort and relief whilst writing this thesis.

“Not everything that can be counted counts and not everything that counts can be counted” – Albert Einstein

“The first draft of everything is sh*t.” – Ernest Hemingway

Abbreviations

2D	2-Dimensional
3D	3-Dimensional
aMT	Astral microtubules
APC/c	Anaphase promoting complex/cyclosome
APS	Ammonium persulfate
ARF	ADP-ribosylation factor
BSA	Bovine serum albumin
CCP	Clathrin coated pit
CCV	Clathrin coated vesicle
ch-TOG	Colonic-hepatic-tumour over expressed gene
CHC	Clathrin heavy chain
CHO	Chinese hamster ovary
CIP	Calf intestinal phosphatase
CLC	Clathrin light chain
DMEM	Dulbecco's modified eagle's medium
DNA	Deoxyribonucleic acid
EDTA	Ethylenediaminetetraacetic acid
EM	Electron microscopy
ER	Endoplasmic reticulum
FBS	Fetal bovine serum
FS	Freeze substitution
G1	Gap-phase 1
G2	Gap-phase 2

GGA	Golgi-localised, gamma adaptin ear-containing, ARF binding
HPF	High pressure freezing
IP	Immuno-precipitation
ipMT	Inter polar microtubules
K-Fibre	Kinetochore fibre
kMTs	Kinetochore microtubules
LM	Light microscopy
MAP	Microtubule associated protein
MIA	Multiple image alignment
MTs	Microtubules
PNK	Poly nucleotide kinase
PSe	Adobe Photoshop Elements
RT	Room temperature
SEM	Standard error of the mean
SpH	Synapto-pHluorin
TACC3	Transforming acidic coiled-coil protein 3
TBE	Tris-Borate EDTA
TBS	Tris buffered saline
TEM	Transmission electron microscopy
TEV	Tobacco etch virus
TGN	Trans-golgi network
UA	Uranyl acetate
UV	Ultra violet
βME	2-Mercaptoethanol

List of figures

Chapter 1 Introduction

Chapter 2 Materials and methods

Chapter 3 Establishing and optimising a series of EM techniques to analyse kMTs and inter-MT bridges

Chapter 5 K-fibres contain an inter-MT 'mesh'

Chapter 7 Appendices

1 Chapter 1: Introduction

1.1 The cell cycle

The cell cycle is a series of coordinated processes that includes; cell growth, DNA replication, distribution of the duplicated chromosomes to daughter cells and cell division. In eukaryotic cells, the cell cycle can be broadly divided into the two stages of interphase and mitosis. Interphase itself can be divided into several sub-phases; Gap-phase 1 (G1), synthesis (S) and Gap-phase 2 (G2) (Norbury and Nurse, 1992). In preparation for cell division cells must satisfy a number of checkpoints (**Figure 1.1**) before entering mitosis. Cyclin dependent kinase (CDK) proteins, through rapid phosphorylation, dephosphorylation and degradation, regulate cell cycle progression (Nakayama et al., 2001, Baldin et al., 1993). G1 is a phase characterised by cell growth and synthesis of new organelles. CDKs 2, 4 and 5 and their respective cyclin components, D and E, control G1 exit into S phase (**Figure 1.1**) (Sherr and Roberts, 1999, Buchkovich et al., 1989). During S phase the genome is duplicated, if this occurs without error then cyclin E is degraded and cyclin A (with CDK 2) promotes cell cycle progression into G2. G2 is the final phase before mitosis and lasts for ~7 hours in human, tissue cultured cells (**Figure 1.1**), here the cells undergo rapid growth and protein synthesis in preparation for mitosis (Rieder, 2011). If the DNA damage checkpoint is satisfied then the progression from G2 to mitosis is permitted, an event controlled by cyclin B and CDK1 (Sancar et al., 2004, Scholey et al., 2003).

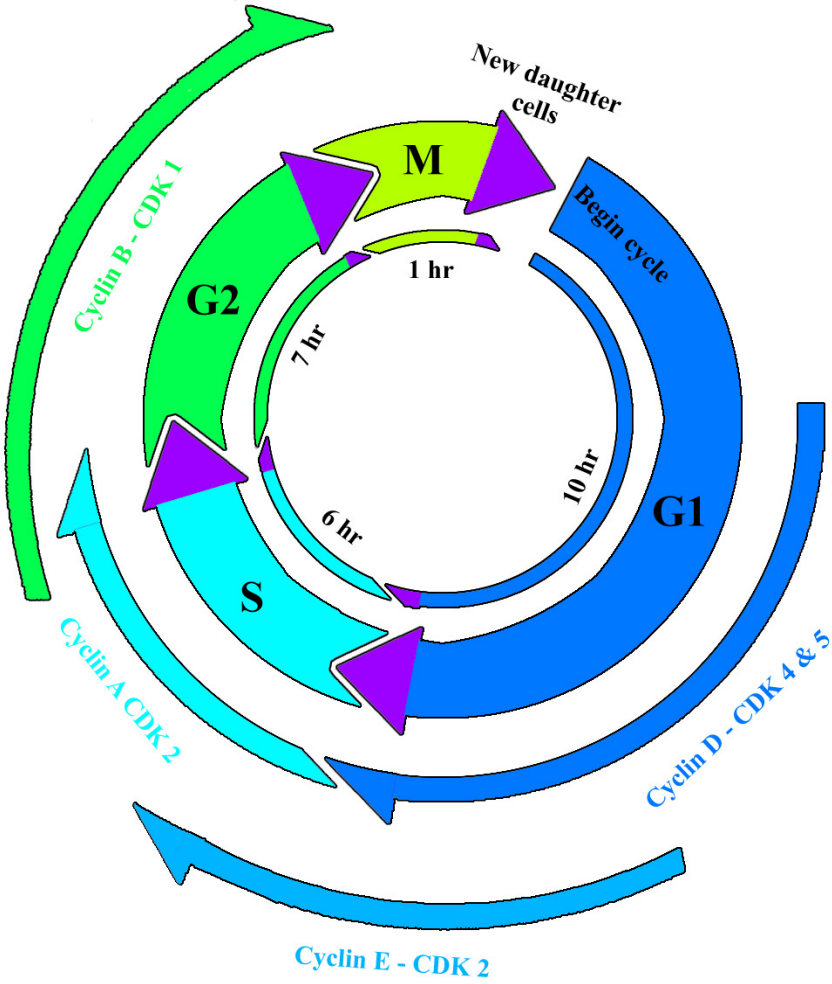

Figure 1.1 – Cell cycle regulation and progression. A schematic diagram of the cell cycle and its key regulators. Cyclins and cyclin dependant kinases (CDKs) are shown on the outside of the cell cycle wheel and the duration of each phase on the inside. Cyclins, are under the control of CDK, their rapid synthesis/degradation and phosphorylation/dephosphorylation is responsible for cell cycle progression from one phase to the next. These proteins are considered as positive regulators. The cell cycle also contains a number of negative regulators, which mainly consist of CDK inhibitors such as p27 and p21. The spatio-temporal activity of each of these proteins is tightly regulated, therefore any errors in expression or activity can result in check-point (purple arrows) activation, leading to cell senescence, aberrant cell division or programmed cell death.

Once the stages of interphase have been completed the cell can progress into mitosis. The purpose of mitosis is to equally segregate two copies of the genome into two daughter cells. To do this the mitotic spindle moves the sister chromatids to opposite poles of the cell (Rieder, 1982, Rieder, 2005, Scholey et al., 2003).

1.2 Stages of mitosis

1.2.1 Prophase

During prophase, chromatin condensation is initiated. Here, duplicate copies of DNA begin restructuring into chromosomes (Koshland and Strunnikov, 1996), this is due the condensin II complex of proteins (Hirano, 2005). The chromosomes are pairs of sister chromatids, one destined for each daughter cell. The centrosomes, which were duplicated during interphase, show an increase in microtubule (MT) nucleation and begin repositioning, one either side of the nucleus (**Figure 1.2 B**). Each centrosome nucleates a radial array of dynamically unstable MTs known as asters (Ault and Rieder, 1994). Finally, the breakdown of the nuclear envelope begins.

1.2.2 Prometaphase

The breakdown of the nuclear membrane is completed. This allows the cytosolic component condensin I to come into contact and interact with condensin II complexes, promoting the final stages of chromosome condensation (Hirano, 2005). Chromosomes start to become captured by MT asters (**Figure 1.2 C**). MT attachment is at the kinetochore, a protein-dense disk that sits at the centromere of the chromosome. Usually one sister chromatid is captured before the other, an event

known as mono-orientation. At this point, the chromosome remains only partially stable until bi-oriented by MT attachment of the other sister chromatid (Ault and Rieder, 1994). MTs that become stably attached to a kinetochore are referred to as kinetochore MTs (kMTs) (Tanaka, 2010). Other non-kinetochore MTs that do not associate with chromosomes begin to extend from the cell poles towards the cell equator. These inter-polar microtubules (ipMTs) can be diverse in length, but can also interact with other ipMTs from the opposite pole (Mastronarde et al., 1993). The aim of prometaphase is to align the chromosomes at a plane equidistant between the cell poles, this is known as the metaphase plate.

1.2.3 Metaphase

At this point in mammalian mitosis, the centrosomes are stable at the cell poles, positioned by pulling (Waters et al., 1993) and pushing (Cytrynbaum et al., 2003) forces of astral MTs (aMTs). All chromosomes have stable attachments with kinetochore fibres (K-fibres (bundles of kMTs)) and are bi-oriented and aligned on the metaphase plate (**Figure 1.2 D**). K-fibres are bundles of kMTs. If stable attachment and bi-orientation is achieved then the spindle checkpoint is satisfied, allowing progression into anaphase (Rieder and Khodjakov, 1997). The spindle checkpoint is satisfied when every kinetochore has accumulated sufficient kMTs and tension has been exerted at sister kinetochores (Hays and Salmon, 1990, Waters et al., 1996). The metaphase to anaphase transition is an event that requires the anaphase promoting complex/cyclosome (APC/c) and Skp, Cullin, F-box containing (SCF) complexes (Nakayama and Nakayama, 2005, Peters, 2002). These are complexes of E3 ubiquitin ligase subunits that target cell cycle proteins for degradation, allowing mitotic progression (King et al., 1996).

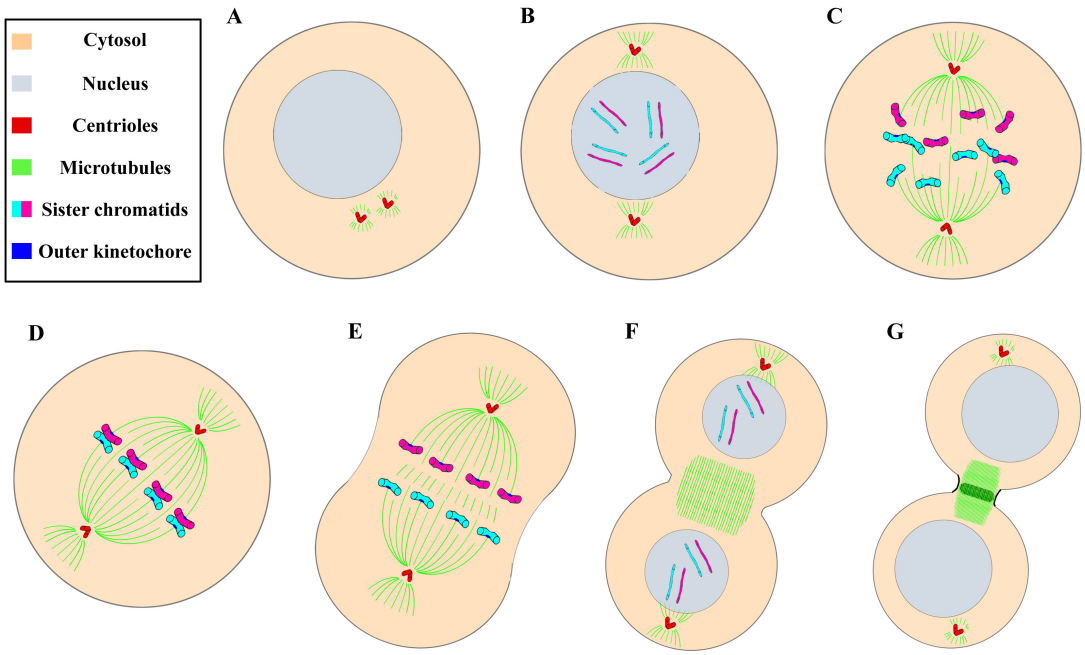

Figure 1.2 – A schematic diagram to show the stages of mitosis. **(A) Interphase (G2):** By this stage replicate copies of DNA have been synthesised and the centrosome has also been duplicated. **(B) Prophase**: The centrosomes begin repositioning to the cell poles and increase in MT nucleation activity. Chromosome condensation begins. **(C) Prometaphase**: Breakdown of the nuclear envelope is completed and MT asters begin chromosome capture. **(D) Metaphase**: Both copies of sister chromatids become stably attached by K-fibres. The chromosomes align on the metaphase plate. **(E) Anaphase**: The spindle checkpoint is satisfied and the sister chromatids are separated and begin segregation towards the cell poles. Invagination at the midzone begins. **(F) Telophase**: The nuclear envelope is reassembled, isolating the duplicate sets of DNA. Formation of the spindle midzone continues, as does ingression of the furrow. **(G) Cytokinesis**: The chromosomes begin to relax and the formation of the intracellular bridge is initiated in preparation for abscission, the final stage of cytokinesis, during which the cells are separated into two daughter cells.

The APC/c is activated by cell-division cycle protein 20 (cdc20), from here the APC/c mediates two primary functions; targeting securin (**see 1.2.4**) and cyclins for degradation (Peters, 2002), this drives chromosome separation and mitotic exit, respectively. The SCF ubiquitinates cyclin-dependent-kinase inhibitors (CKIs) such as p27 and p21 (Morgan, 1995), targeting them for proteosome degradation, hence promoting cell cycle progression (Nakayama and Nakayama, 2005).

1.2.4 Anaphase

The purpose of anaphase is to start the migration of sister chromatids towards the cell poles (**Figure 1.2 E**), an action facilitated by the pulling action of K-fibres of the spindle apparatus (Scholey et al., 2003). Before movement can occur, the sister chromatids must be separated from one another. Securin, a protein complex that binds to and inhibits separase throughout most of the cell cycle, becomes degraded during the metaphase-to-anaphase transition (Uhlmann et al., 1999). Cohesin, the central mediator responsible for the cohesion of sister chromatid arms, is cleaved by the active form of separase (Uhlmann et al., 2000). As chromosomes are pulled apart, the formation of the spindle midzone is simultaneously triggered (**Figure 1.2 E**). As late anaphase approaches, ipMTs are repositioned into the gap left between the dividing chromosomes (Straight and Field, 2000). Midzone microtubules consist of a tight bundle of mostly anti-parallel MTs, these dictate the position of the cleavage plane, an area the cell will later use as its division point (Field et al., 1999).

1.2.5 Telophase

One of the key features of telophase is the reformation of the nuclear envelope (**Figure 1.2 F**), where the majority of membrane is derived from the

endoplasmic reticulum (ER) (Larijani and Poccia, 2009). In addition, the MTs of the midzone become even more concentrated (**Figure 1.2 F**), with the continued recruitment of bundling proteins such as the protein regulator of cytokinesis 1 (PRC1). The CDK mediated phosphorylation of PRC1 during prophase renders it inactive until dephosphorylation during anaphase. The active form of PRC1 orchestrates the spatiotemporal regulation of midzone MTs (Zhu et al., 2006).

1.2.6 Cytokinesis

Cytokinesis can be described as the creation of two daughter cells, from one adult cell, following mitosis. During cytokinesis, invagination of the plasma membrane increases in response to the continued reorganization of actin and formation of the contractile ring (Salmon, 1989). The furrow continues to ingress synchronously from all sides of the cell until it becomes compressed against the MTs composing the central spindle, the result is the formation of the midbody (**Figure 1.2 G**) (Salmon and Wolniak, 1990). The spindle midbody is the focal point for abscission, the finale of cell division, where the two daughter cells become completely isolated from one another. Abscission events are driven by the ESCRT III membrane-remodeling proteins (Carlton and Martin-Serrano, 2007).

1.3 The mitotic spindle

Mitosis could not be completed in mammalian cells without the formation of the spindle apparatus. This highly dynamic piece of machinery is responsible for fulfilling numerous roles during mitosis and is also capable of radical restructuring to achieve these functions. The spindle is composed of MTs and hundreds of associated motor and non-motor proteins (Mandelkow and Mandelkow, 1995). As

this project is primarily concerned with the metaphase spindle, this introduction will focus on the structure of the spindle apparatus during this stage of mitosis.

1.3.1 Microtubules

Microtubules are non-covalent polymers of the protein tubulin. Like many other cytoskeleton proteins, tubulin is well conserved throughout evolution and is expressed in all dividing eukaryotic cells (Burns, 1991). MT subunits are composed of heterodimers of α-tubulin and β-tubulin. The α- and β-tubulin monomers share ~50% homology at the amino acid (AA) level (Sullivan, 1988). Tubulin heterodimers of mammalian MTs arrange into thirteen linear protofilaments, these are associated laterally into cylindrical tubes that contain a hollow lumen (**Figure 1.3**), the diameter of a MT is ~23 nm (Desai and Mitchison, 1997). Although protofilament number in mammals is thirteen, this can vary in other species and MT based organelles (**Figure 1.3 B**) (Bohm et al., 1984). To assemble into a MT the protofilaments form outwardly curved tubulin sheets, which gradually close to form MT cylinders (Vitre et al., 2008, Mahadevan and Mitchison, 2005). The study of MTs at the ultrastructural level is only possible using electron microscopy (EM).

To assemble into microtubules, α- and β- tubulin dimers bind to guanosine-5'-triphosphate (GTP). Following the energy transfer, β-tubulin, in a GTP bound state, is added onto MT plus-ends **(Figure 1.3 A)**. MTs are polar, the faster-growing GTP end is referred to as the plus end and the slower-growing GDP end is referred to as the minus end (Allen and Borisy, 1974). Once a new dimer is incorporated onto the plus-end it becomes hydrolysed into a guanosine-5'-diphosphate (GDP)-bound state (**Figure 1.3 A**).

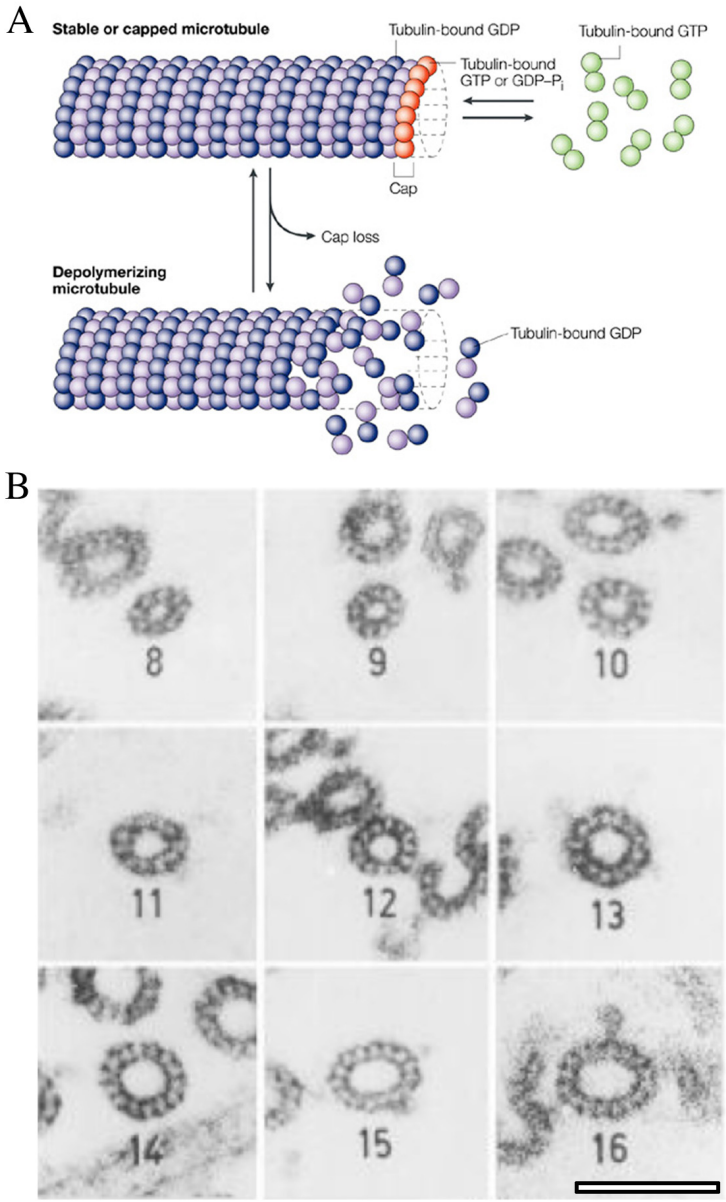

Figure 1.3 – Microtubule assembly and architecture. (**A**) A schematic diagram showing microtubule assembly from α- and β- tubulin dimers. GTP-bound tubulin (green) associates with MT plus ends, promoting polymerisation. If a MT does not contain a tubulin-GTP 'cap' (red) then the GDP-bound tubulin (blue/purple) can undergo deplymerisation (Jordan and Wilson, 2004). (**B**) Electron micrographs (Bohm et al., 1984) of MT cross-sections containing different numbers of protofilaments. Typically, most microtubules contain 13 or 14 protofilaments, however there are exceptions where a microtubule may contain an alternative number. Individual tubulin subunits have diameters of ~4 nm. Scale bar, 50 nm.

Whether or not a tubulin dimer is in a GTP or GDP bound state, directly influences MT stability, where GTP bound dimers favour polymerisation and GDP bound dimer favour deploymerisation (Heald and Nogales, 2002). A change in MT flux from polymerisation (growth) to deploymerisation (shrinkage) is known as catastrophe, the reversal of this process is referred to as MT rescue (Howard and Hyman, 2003).

1.3.2 Ultrastructure of the metaphase spindle

The metaphase spindle is composed of three major classes of microtubule: astral microtubules (aMTs), inter-polar microtubules (ipMTs) and kinetochore microtubules (kMTs) (**Figure 1.4**). During prophase and prometaphase, MT asters nucleate from the centrosomes, an event reliant of the presence of γ-tubulin, the key unit on the γ-tubulin ring complex, a structure that acts as a scaffold for MT polymerisation (Martin et al., 1997, Moritz and Agard, 2001). MTs in asters can follow one of three paths: 1) they nucleate towards and eventually attach to a chromosome, in which case they become kMTs; 2) they nucleate away from the cell cortex, towards the cell equator, but are not involved in chromatid capture, in which case they become ipMTs; 3) they nucleate towards the cell cortex, becoming aMTs (Ault and Rieder, 1994, Tanaka, 2010).

The metaphase spindle of a mammalian cell is dominated by kMTs and ipMTs, one classic study found the spindle to consist of 55-60% ipMTs and 40-45% kMTs (Brinkley and Cartwright, 1971). During the latter stages of mitosis the ipMT:kMT ratio is adjusted in favour of ipMTs, due to formation of the midzone (Brinkley and Cartwright, 1971). The density of aMTs varies greatly between species, for this reason and also due to their comparatively unorganised arrangement, very little ultrastructural information exists for aMTs (Mcintosh and Landis, 1971).

However, one study quantified that the spindle of the fungus, *Neetria haematococca,* contained 37% aMTs (Jensen et al., 1991). This number is unlikely to be representative for mammalian spindles due to the vast difference in cell size and overall spindle architecture.

1.3.2.1 Astral microtubules

Astral MTs nucleate from the centrosome and contact the cell cortex, here they associate with the actin cytoskeleton (Kunda and Baum, 2009), a relationship governed by the multisubunit motor complex, dynein (Markus and Lee, 2011, Millar et al., 2004). Astral MTs have a role in spindle orientation and therefore the positioning of the division plane during cytokinesis (Wuhr et al., 2009). Ultrastructurally, aMTs are not organised into compact bundles, rather, they remain freely isolated from one another (Vogel et al., 2007).

1.3.2.2 Inter-polar microtubules

The MTs of metaphase cells that extend from the cell pole towards the opposite pole but do not target a kinetochore, are known as inter-polar microtubules (ipMTs). These are diverse in length and sometimes interact with microtubules from the opposite pole. Inter-polar MTs are thought to provide spindle stability by coordinating the spindle poles and are also involved in spindle elongation during anaphase (Snyder et al., 1986, Mcdonald et al., 1992).

The number of microtubules assembled in the metaphase spindle of mammalian cells ranges from 1500-3400, depending on the cell type and position of the spindle analysed (Mcintosh and Landis, 1971).

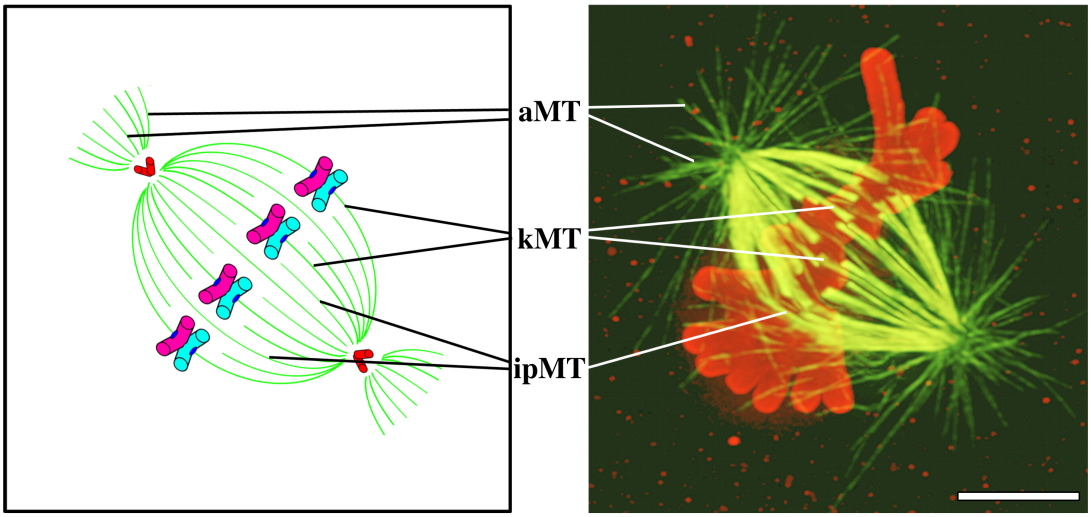

Figure 1.4 – Composition of metaphase microtubules. A schematic diagram (left) and fluorescence micrograph (right) showing an overview of a mitotic cell in metaphase. The spindle is assembled from three microtubule sub-types (green); astral microtubules (aMTs), that nucleate away from the spindle and usually towards the cell cortex; kinetochore microtubules (kMTs), that extend from the cell pole and terminate at an attachment on the kinetochore (located on the front of each sister chromatid); inter-polar microtubules (ipMTs), that extend from the cell pole towards the chromosomes, but have no kinetochore attachment, rather, they remain unattached at the MT plus end, or they interact with other ipMTs from the opposite spindle pole. Scale bar, 4 μm.

A peak in MT density is seen half way between the spindle pole and the metaphase plate, this frequency decreases at each side of this position, as either the cell equator or the cell pole is approached. Less than 25% of ipMTs terminate within 1 μm of the cell pole and only 10% extend from one cell pole and attach at the opposite pole (Mcdonald et al., 1992, Mcintosh and Landis, 1971). The remaining ipMTs terminate within their own half spindle or part way through the opposing half spindle. Although there is still a relatively high frequency of ipMTs within close proximity or passing through the cell equator, these show almost no preference for bundling (2 – 4 ipMTs per bundle), this preference is increased slightly as the onset of anaphase approaches (2 – 6 ipMTs per bundle). The ipMTs found close to the cell equator contain a mixture of parallel and anti-parallel MTs, where anti-parallel MTs comprise 55-70% of the total ipMT population (Brinkley and Cartwright, 1971). The parallel ipMTs are only weakly associated with one another, whereas the anti-parallel ipMTs are more strongly associated. The small bundles of anti-parallel ipMTs present during metaphase are thought to be the forerunners for MTs of stem bodies, the precursors of the spindle midbody (Mastronarde et al., 1993, Mcintosh et al., 1975). As mitosis progresses the distribution of inter-ipMT spacing become more uniform, an event that is attributed to the increase in anti-parallel ipMTs, i.e. the forming of stem bodies and eventually the midzone (Mastronarde et al., 1993).

1.3.2.3 Kinetochore microtubules

Kinetochore MTs extend from the cell pole and terminate at the kinetochore (**Figure 1.5 A & D**). These MTs are essential for the capture and congression of chromosomes to the cell equator during prometaphase and metaphase. They are also responsible for the propagation of poleward forces during anaphase (Bloom and

Joglekar, 2010, Compton, 2007, Rieder, 1981). These movements occur in large part due to the loss or addition of tubulin subunits to elongate or shorten the kMTs. Biophysical experiments suggest that K-fibres can exert large forces, far in excess of what is required to move a chromosome through the viscous cytosol (Nicklas, 1988). It is also possible for a K-fibre to move a chromosome through pushing (Mitchison and Kirschner, 1985).

Kinetochore MTs are packed into bundles (**Figure 1.5 B, C, E & F**) where they are referred to as kinetochore fibres (K-fibres). The number of kMTs per bundle varies between species and cell types, ranging from 1 in *Saccharomyces cerevisiae* to 120 in *Haemanthus* (Bajer, 1973). The K-fibres of higher mammals typically contain 20-40 kMTs per bundle (Bajer, 1973, Mcdonald et al., 1992, Mcintosh et al., 1975, Rieder, 1982) with human spindles containing ~30 kMTs per bundle (Mcintosh and Landis, 1971). Other examples would include the K-fibres of *Schizosaccharomyces pombe* (4-6 kMTs), *Drosophila melanogaster* (11 kMTs) (Ding et al., 1993, Maiato et al., 2006) and Chinese hamster ovary cells (13 kMTs) (Witt et al., 1980, Witt et al., 1981). The number of kMTs contained within a bundle is closely related to the diameter of the kinetochore and not necessarily the size of the chromosome (McEwen et al., 1998, Cherry and Johnston, 1987). Every chromosome possesses an inner- and outer-kinetochore (**Figure 1.5 B & C**), these are positioned on the outer face of the chromosome, but where the two daughter chromatids are closest in contact. The inner-kinetochore is closely associated with the centromere, a DNA region essential for kinetochore assembly (Mitchison, 1988).

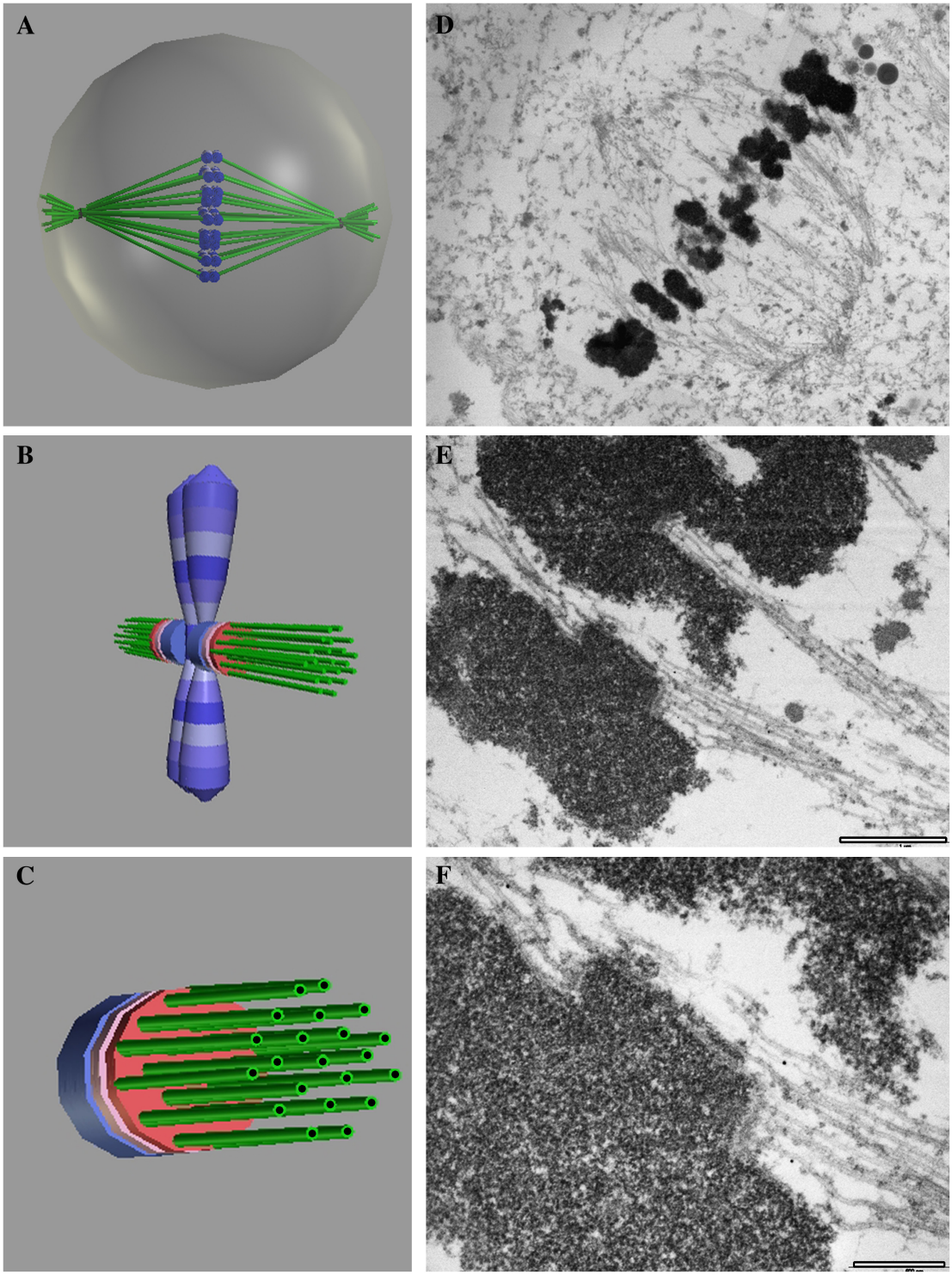
A
D
B
E
C
F

Figure 1.5 – K-fibres and kMT attachment at the kinetochore. 3D models (**A-C**) and electron micrographs (**D-F**) of a mitotic cell in metaphase. Electron micrographs were taken from a mitotic HeLa cell, sectioned longitudinally, that had undergone cytosolic wash-out, to improve K-fibre visibility. Each row shows a progressive higher magnification. (**A & D**) Low magnification images, giving a cell overview that shows a series of K-fibres extending from the cell pole and terminating at attachments on the chromosomes. (**B & E**) Medium magnifications reveal the individual kMTs of the K-fibre bundle. Human K-fibres contain 20-40 kMTs. Scale bar, 1 μm. (**C & F**) High magnification images show the kMTs terminating at the outer kinetochore (red), an electron-dense disk on the front of both of the sister chromatids, just in front of the inner kinetochore (pink) and the centromere (blue). As the chromatids are stably attached by K-fibres from both sides, the chromosome is bi-oriented at the metaphase plate. Scale bar, 500 nm.

The outer kinetochore is a structure that attaches the chromosome directly to kMTs (**Figure 1.5**). Both the inner and outer kinetochore are composed of dense protein clusters, such as the Ndc80 complex, a necessity for kMT-kinetochore attachment (Sullivan et al., 2001).

Unlike ipMTs, the MTs of a K-fibre are well organised and deviate very little from their course at the point of origin at the cell pole, until termination at the kinetochore (Mcdonald et al., 1992, McIntosh et al., 1979). It has been shown that ipMTs can infiltrate a K-fibre periodically throughout its length. Within close proximity to the kinetochore this infiltration is minimal, towards the cell pole the frequency of ipMTs within the K-fibre increases, an expected occurrence due to the sheer volume of MTs at the spindle pole. Although these ipMTs appear to be part of the K-fibre, they display large levels of displacement throughout the half spindle length and show no or a very weak association with kMTs (Mcdonald et al., 1992, Witt et al., 1981).

In summary, of the three types of MT in the metaphase spindle, only kMTs and anti-parallel ipMTs are well-organised into bundles. Of these the K-fibre is easily distinguished on the basis of its size. It is well established that MT bundles in cells are organised by cross-linking proteins (Peterman and Scholey, 2009, Rubinstein et al., 2009). The kMTs of a K-fibre are similarly organised by cross-linkers (Hepler et al., 1970, Witt et al., 1981).

1.4 Microtubule cross-linking proteins

MT cross-linking proteins or ‘bridges’ have been observed and studied in a variety of organisms. A bridge is defined as an electron-dense structure that connects two microtubules, in electron micrographs (**Figure 1.6**). In the literature

MT cross-linkers are almost exclusively referred to as 'bridges', although they are sometimes termed 'arms'.

1.4.1 Inter-MT bridges in K-fibres

Inter-MT bridges have been observed in K-fibres, where they are thought to promote kMT organisation and stability (Bastmeyer and Fuge, 1986, Hepler et al., 1970, Mcdonald et al., 1992, Witt et al., 1981), however, these have never been fully characterised in molecular terms. Inter-kinetochore microtubule (inter-kMT) bridges have been observed in a number of species. Examples include the African blood lily, *Haemanthus katherinae* (Hepler et al., 1970), the crane fly (Bastmeyer and Fuge, 1986), Chinese hamster (CHO) cells (Witt et al., 1980) and finally, human spindles (**Figure 1.6**) (Hepler et al., 1970). Regardless of the species, inter-kMT bridges appear structurally similar throughout, measuring 2-5 nm in width and 20-40 nm in length. In human cells they are most frequently ~20 nm in length (**Figure 1.6**) (Hepler et al., 1970).

Bastmeyer *et al*. analysed bridges in the meiotic spindle of the crane fly, observing that the dimensions of bridges were variable, ranging between 6 and 30 nm in length and 4 and 19 nm in thickness (Bastmeyer and Fuge, 1986). This study also revealed that the frequency of inter-MT bridges was directly proportional to MT density and frequency of paired MTs, i.e. the greater the number of paired MTs the higher the incidence of bridges. They suggested that a greater density of MTs would require more structural support and organisation, hence the increase in bridge frequency.

Witt *et al*. studied bridges in CHO cells, where they carried out cell lysis to remove cytosolic background (Witt et al., 1981).

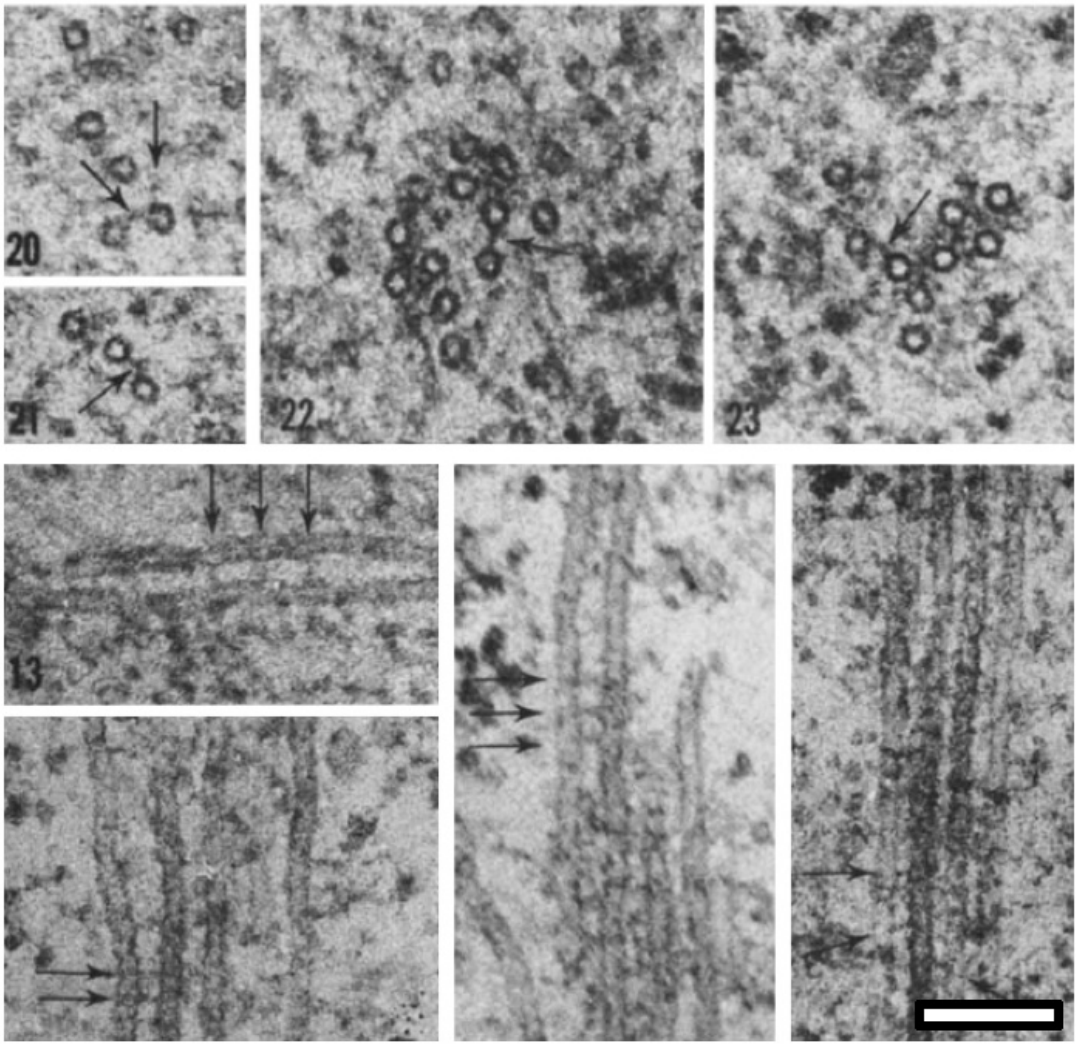

Figure 1.6 – Inter-MT bridges in human K-fibres. A gallery of electron micrographs showing inter-MT bridges (black arrows) between kMTs. The figure was taken from a classic EM study of HeLa and WI-80 cells by Hepler *et al* (1970). The bridges are described as electron dense structures that cross-link two MTs, they are 2-5 nm in diameter and 20-40 nm in length. Bridges were observed in both longitudinally and orthogonally sectioned K-fibres, appearing most frequently in longitudinal sections. Scale bar, 150 nm.

They observed a 'fine filamentous material' that cross-bridged kMTs. The bridges were approximately 5 nm wide and 30-40 nm long and often appeared to attach at an acute angle rather than perpendicular to the MT wall. In addition, they also noted that one MT can crosslink to at least four other MTs. Witt *et al*. went on to hypothesise that bridges could provide a structural role, by tethering the kMTs together into one mechanically coherent bundle, suggesting that this would be more efficient at propagating force from the cell pole to the chromosome (Witt et al., 1981).

Hepler *et al*. observed 'bridges' and 'arms' that cross-bridged kMTs and MTs of the midzone in human cells (**Figure 1.6**). They considered these bridges to be similar in appearance, measuring about 2-5 nm in width and 20-40 nm in length, regardless of the MT subtype they were associated with. They also noted that bridges were both straight and curved, occurring at various tilt angles relative to the MT surface and also that one MT could have multiple projections. This study also noted that inter-MT bridges appeared to be observed periodically along the length of MTs with gaps of 10, 20, 30 and 40 nm, suggesting that particular MT binding sites are available (Hepler et al., 1970).

1.4.2 Characterised inter-MT bridges

The identity of bridges in K-fibres may be elusive but some inter-MT bridges have been characterised, good examples are MAP2 (Harada et al., 2002, Kim et al., 1979) and PRC1. PRC1 is the most comprehensively studied and best-characterised bridge in the mitotic spindle (Kurasawa et al., 2004, Mollinari et al., 2002, Subramanian et al., 2010, Zhu et al., 2006, Elad et al., 2011).

During the later stages of mitosis, a dense network of anti-parallel MTs becomes bundled in the spindle midzone (Mastronarde et al., 1993). This contributes to the formation of the midbody (**Figure 1.2 F & G**) (Schiel and Prekeris, 2010). The midbody acts as a docking-station for a number of proteins essential for abscission, the finale of cytokinesis (Wheatley and Wang, 1996, Glotzer, 1997b, Glotzer, 1997a). Some well-known midbody proteins include: Aurora B (Terada et al., 1998), INCENP (Cooke et al., 1987), PlK (Carmena et al., 1998) and MKLP 1 and 2 (Nislow et al., 1992, Neef et al., 2003). Each of these is important in its own right, however, their correct localisation and function is reliant on the successful formation of the midbody, an event which is regulated by PRC1 (Mollinari et al., 2002). PRC1 and its binding partner KIF4 are the main MT bundling proteins during cytokinesis (Kurasawa et al., 2004). They localise to MTs of the midzone during anaphase, becoming more concentrated as the midbody assembles and mitosis progresses (Kurasawa et al., 2004). During early mitosis PRC1 remains as an inactive monomer in response to CDK-mediated phosphorylation. During the metaphase-to-anaphase transition, PRC1 is dephosphorylated, promoting dimerisation (Jiang et al., 1998). PRC1 dimers act as a physical cross-linker to bundle MTs, these bridges have been reconstructed *in vitro* (Mollinari et al., 2002, Subramanian et al., 2010) and have been observed *in vivo* (Elad et al., 2011). The functional importance of PRC1 or KIF4 is demonstrated either by knockdown or overexpression. In PRC1-depleted cells, midzone and midbody formation is disrupted, as is the correct localisation of Aurora B, MKLP1 and CENP-E (Kurasawa et al., 2004). Cells depleted of KIF4 exhibit poorly-organised MTs and loss of the electron dense midbody (**Appendix Figure 7.2**), an observation also seen in other

studies (Hu et al., 2011). Overexpression of PRC1 results in the extensive bundling of interphase MTs (Mollinari et al., 2002).

In summary, PRC1 is currently the best-studied inter-MT bridge in the spindle apparatus, where it functions by bundling non-kinetochore MTs during late mitosis. Depletion of PRC1 or its binding partner KIF4 results in a reduction of midzone integrity as a consequence of poorly organised MTs. The knock-on effect of this phenotype is the loss of midbody assembly and therefore a loss of docking sites for other essential abscission proteins.

1.4.3 Other MT-associated bridges

In addition to inter-MT bridges of the spindle, bridges have also been studied elsewhere, some examples would include: microtubules of flagella, cilia and axostyle (Tilney, 1971, Roth et al., 1970, Barton, 1969) or the interstitial cells of the adult cricket, *Gryllus assimili*, which contain microtubules that are interconnected by 12-14 nm long arm-like structures (Friedman, 1971). Another well-studied example is MAP2, one of the most abundant MAPs in the brain. MAP2 mainly localises to the somatodendritic compartments in neurons, where it has been shown to promote neurite-growth through stabilisation of MTs by cross-bridging (Matus, 1994). Overexpression of MAP2 resulted in excessive MT bundling (Hirokawa, 1994, Takemura et al., 1992). In addition, the Purkinje cell dendrites of MAP2 knock-out mice exhibit morphologically atypical inter-MT bridges, compared to those from controls (Harada et al., 2002).

Finally, bridges have also been studied cross-linking MTs with other structures, including organelles (as opposed to just other MTs), such as vesicles (Allen, 1975, Smith et al., 1977, Smith, 1971), mitochondria (Smith et al., 1977) and

membranes (Franke et al., 1971). Although bridges have been observed cross-linking a variety of structures, it is inter-MT bridges in K-fibres that are the least understood and the focus of this project.

1.5 Candidates for the inter-MT bridges of K-fibres

To test the function of inter-kMT bridges, the identity of this protein or complex of proteins needs to be discovered. A short list of potential candidates has been proposed, these include; HSET, hepatoma up-regulated protein (HURP) and clathrin.

HSET is a minus-end directed kinesin motor protein (Cai et al., 2009). HSET and its homologues have been shown to contribute to the structural integrity of the spindle and also the efficiency of spindle assembly through the focusing of microtubule minus ends (Walczak et al., 1997, Endow and Komma, 1997, Endow and Komma, 1996). As the exact mechanism of action of HSET is not fully understood, Mountain *et al.* suggested that its function is conferred through the physical cross-linking of kMTs (Mountain et al., 1999). They proposed that HSET, in cohort with the plus-end directed protein Eg5, generate MT sliding potential relative to one another, in doing so promote specific MT end convergence. Whilst Mountain *et al.* showed good evidence for HSET and Eg5 working together to promote spindle assembly and bipolarity, only one figure contained data that directly tested their bridge hypothesis. Here, they carried out immunogold labelling using anti-HSET antibodies, localising HSET to spindle MTs. They found that the gold label was 'predominantly' observed between kMTs (49%). The localisation of the remaining gold label was found on MT walls (34%), astral MTs (9%) and non-spindle associated (8%). Although this does provide some direct evidence for HSET

as an inter-MT bridge, some flaws in the experimental procedures were apparent. First, there is no mention of how gold label that was on or near to the MT wall is discriminated from particles 'between' MTs. This is odd given that it appears they have not taken into account the potential combined length of the primary and secondary antibodies (up to 16 nm (Ottersen, 1989)) in their proximity measurements. Second, although this study has proposed HSET as an inter-MT bridge and rightly used EM to test this, no mention has been given to the bridges present in their representative micrographs, which, although apparently poorly preserved (perhaps as a result of the cytosolic washout), did not appear to be associated with any gold particles.

HURP, is a MAP that is thought to promote spindle stability and enhance microtubule polymerisation by reducing the turnover rate of α/β-tubulin subunits on the spindle (Wong and Fang, 2006). Although HURP has not directly been tested as a bridge, dimerised HURP (Koffa et al., 2006) could still be considered as a potential bridge candidate. HURP has been shown to have a role in the efficient search and capture of kinetochores, timely congression of chromosomes and generation of proper tension across sister kinetochores (Sillje et al., 2006), furthermore, the kMT stability conferred by HURP is greater in cells where it is over expressed and concentrated on the spindle (Wong and Fang, 2006). HURP is localised in a gradient across the spindle MTs with the highest concentration at chromatin-proximal regions and decreasing in concentration as the spindle pole is approached (Wong and Fang, 2006). Currently, no data exists to show that the inter-MT bridge frequency in K-fibres, of any species, increases towards the kinetochore end of MTs. In addition, since MT density is at its greatest towards the cell poles, it is plausible that bridge frequency is at its densest here, this is a theory supported by other studies (Rieder,

1982). If this is true, then due to its localisation, HURP is unlikely to be a bridge in K-fibres.

The third candidate for inter-MT bridges is clathrin, the focus of this project.

1.6 Clathrin

1.6.1 Structure

Clathrin is triskelion-structured protein assembly composed of three heavy (190 kDa) and three light (25–27 kDa) chains (Kirchhausen and Harrison, 1981). During interphase, the triskelion shape of the clathrin molecule allows it to form the polyhedral lattice or 'coat' that covers clathrin coated vesicles (CCVs) and clathrin coated pits (CCPs) (Brodsky et al., 2001) (**Figure 1.7 B**). The molecular composition of a clathrin triskelion is defined in a model generated using electron cryo-microscopy combined with existing crystal-structure knowledge (Fotin et al., 2004). A single clathrin heavy chain (CHC) molecule possesses: an N-terminal seven-bladed β-propeller (residues 1-330), a linker region, eight clathrin heavy-chain repeat (CHCR0-7) segments (residues 395-1576), a proximal hairpin, a tripod region and a variable C-terminal segment (residues 1631-1675) (**Figure 1.7 A**). One CHC molecule is often described as resembling a human leg consisting of a foot (the N-terminal domain, linker and part of CHCR0), an ankle (corresponding to the remainder of CHCR0, CHCR1 and CHCR2) and the knee (CHCR5). The CHCR7 repeat extends into the trimerisation region of a triskelion hub, this together with CHCR6, form the proximal segment (**Figure 1.7 A**) (Fotin et al., 2004).

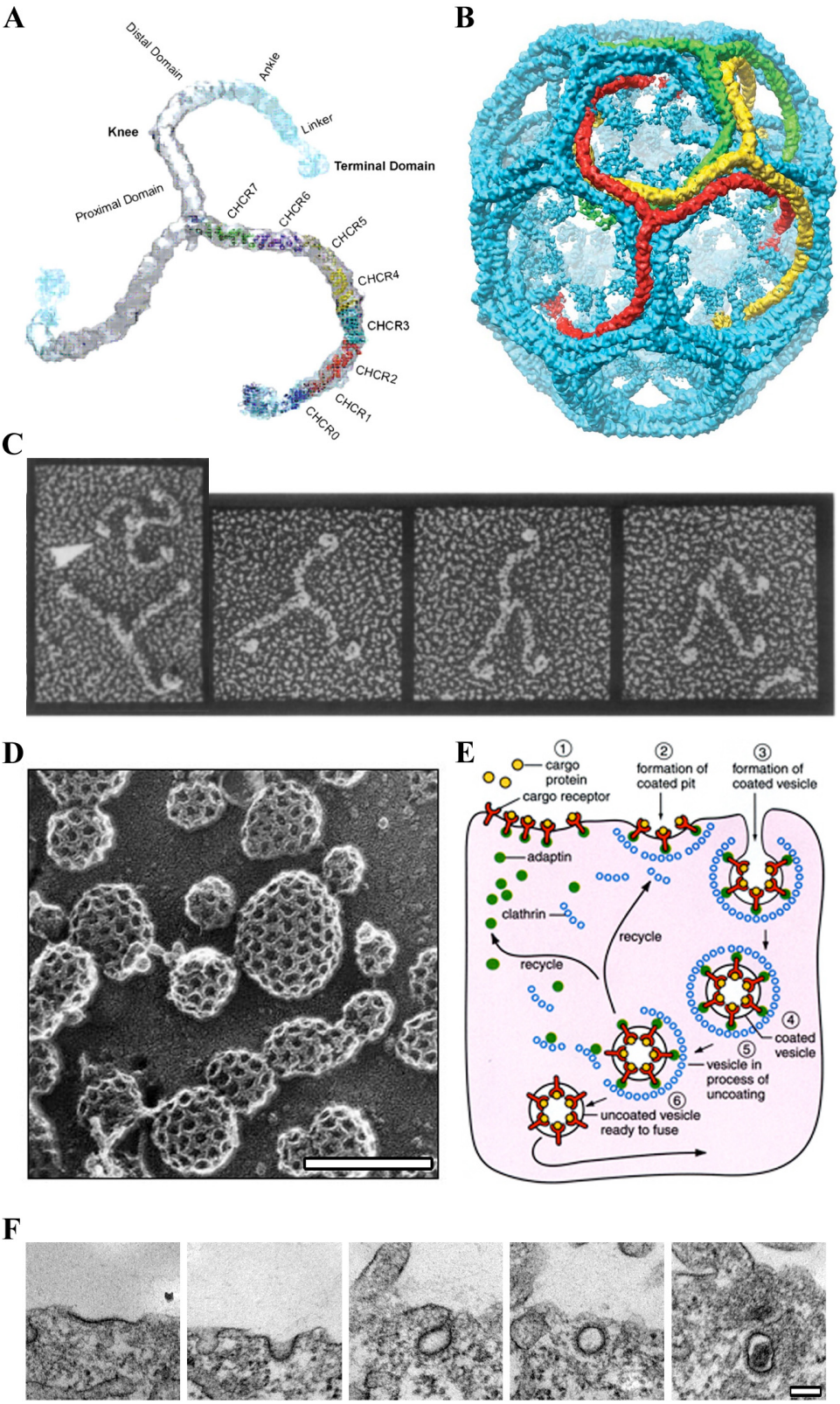
A
Distal Domain
Ankle
Linker
Knee
Terminal Domain
Proximal Domain
CHCR7
CHCR6
CHCR5
CHCR4
CHCR3
CHCR2
CHCR1
CHCR0
B
C
D
E
1
cargo protein
cargo receptor
2
formation of coated pit
3
formation of coated vesicle
adaptin
clathrin
recycle
recycle
4
coated vesicle
5
vesicle in process of uncoating
6
uncoated vesicle ready to fuse
F

Figure 1.7 – Clathrin triskelia, CCV architecture and endocytosis. **A**) An atomic model of the clathrin triskelion, highlighting the key CHC components. **B**) An image reconstruction of clathrin triskelia assembled into a hexagonal barrel. The CCV contains 36 individual clathrin triskelions within the structure. **A** & **B** were taken from Fontin *et al*, 2004. **C**) Electron micrographs showing examples of clathrin triskelia prepared using freeze-etching and platinum mica sheets (Heuser and Kirchhausen, 1985). The individual triskelia exhibit a large degree of structural flexibility. Box width is 100 nm. **D**) Deep-etch electron micrographs containing fully assembled clathrin cages, isolated from calf brain (Heuser and Kirchhausen, 1985). Scale bar, 150 nm. **E**) A schematic diagram showing the role of clathrin during the internalisation of cargo at the plasma membrane. Schematic was adapted from (Mousavi et al., 2004) **F**) A panel of electron micrographs showing the life cycle of clathrin during endocytosis (left to right), from clathrin recruitment to the plasma membrane, pit formation and finally, vesicle budding. Scale bar, 100 nm.

Atomic force microscopy of isolated clathrin triskelia show that each leg has a contour length of ~52 nm and a radius of ~2 nm (Jin and Nossal, 2000). Individual clathrin triskelia are capable of huge structural diversity due to the potential bending angles at the triskelion hub, knees and ankles, this is best shown using a specialist type of electron microscopy, pioneered by John Heuser, known as 'deep-etch' (**Figure 1.7 C**). This technique yields 3D micrographs that contain high levels of topological detail (Heuser, 1981, Heuser, 2011). Heuser has published numerous studies containing images of clathrin triskelia in a variety of geometric positions (Heuser, 1980, Heuser and Kirchhausen, 1985, Heuser and Keen, 1988), some examples are shown in **Figure 1.7 C**. The panel on the far left shows a particularly nice example of two triskelia in remarkably different configurations. The length of the triskelion at the top of the panel, from N-termini to N-termini is approximately half the length of the triskelion at the bottom of the image (**Figure 1.7 C**).

1.6.2 Clathrin and membrane trafficking

To function in membrane trafficking, clathrin triskelia assemble into a polyhedral lattice, becoming a CCP and eventually a CCV (**Figure 1.7 B, D & F**). CCVs can form at different compartments in the late secretory and in the endocytic pathway, such as the trans-golgi network (TGN), endosomes and the plasma membrane (Mukherjee et al., 1997, Mousavi et al., 2004). One of the best-known roles of clathrin is during clathrin-mediated endocytosis, which can be defined as, the cellular uptake of material from the plasma membrane. This is a process used by all eukaryotic cells where extracellular cargo at the plasma membrane is internalised into vesicles and distributed to various intracellular destinations (Mukherjee et al., 1997). Briefly, cargo is recognised at the plasma membrane by cargo-specific

receptors, leading to the recruitment of adaptor-proteins such as the AP2 protein complex (Edeling et al., 2006). AP2 complexes mediate the recruitment and binding of clathrin, with the help of accessory proteins, in a spatio-temporal regulated manner (Edeling et al., 2006). The accumulating triskelia begin assembling into a lattice along the inside of the plasma membrane (**Figure 1.7 E & F)**. Next, the cargo is internalised into a clathrin-coated pit, which continues to 'bud' from the plasma membrane (**Figure 1.7 E & F)**. Eventually the vesicle, encased within a clathrin coat, is pinched off from the membrane, an event mediated by dynamin (**Figure 1.7 E & F) (**Robinson, 1994). The fully formed CCV begins migrating towards its intended intracellular destination. During migration CCV 'uncoating' occurs, where the clathrin triskelia and associated adaptors disassemble and detach from the vesicle. Once the coat has been shed, the remaining vesicle fuses with endosomes and proceeds down the endocytic pathway. Clathrin and adaptors are recycled in preparation for more endocytosis (Robinson, 2004, Edeling et al., 2006). In addition to the role of clathrin in vesicle formation at the plasma membrane, clathrin also functions in the packaging and trafficking of cargo from the trans-golgi network (TGN) (McNiven and Thompson, 2006). In this capacity, CCVs bud from the TGN and transport mannose-6-phosphate receptor (and associated enzyme complexes) to late endosomes and lysosomes (Wu et al., 2003). The formation of CCVs at the TGN is regulated via proteins such as ADP-ribosylation factor (ARF) GTPase and by extension, the recruitment of clathrin adaptors, including AP1 and golgi-localised, gamma adaptin ear-containing, ARF binding (GGA) proteins (Puertollano et al., 2001, Robinson and Bonifacino, 2001).

1.6.3 Clathrin in mitosis

In addition to its role in membrane trafficking, clathrin also performs a 'moonlighting' role during mitosis (Royle and Lagnado, 2006, Royle et al., 2005, Royle, 2006). It is generally accepted that mitosis is a phase of the cell cycle where endocytosis remains dormant (Warren, 1993), however, this notion has been challenged on occasion (Boucrot and Kirchhausen, 2007). During some periods of mitosis the surface area of the cell decreases (Ohnuma et al., 2006, Boucrot and Kirchhausen, 2007). For this reason, Boucrot *et al* hypothesised and tested that the observed reduction in receptor-mediated endocytosis of transferrin, during mitosis, could be related to the decrease in the surface area of the cell, and not necessarily a net reduction in endocytic activity (Boucrot and Kirchhausen, 2007).

The association between clathrin and mitosis began in 1985, when an immunocytochemical investigation into the distribution of membranous organelles, during early mouse development, revealed that clathrin localises to the spindle of unfertilised mouse eggs (Maro et al., 1985). Nothing further was reported until the spindle localisation was re-confirmed in several cell lines and using three different primary antibodies to detect clathrin (Okamoto et al., 2000). Shortly after, clathrin was shown to interact with mitotic microtubule asters assembled *in vitro*, in a study where mass spectrometry was used to identify the proteins associated with microtubules assembled in a cell-free mitotic extract (Mack and Compton, 2001). Interestingly in this study they claim that the clathrin was a contaminant. This is probably one of the reasons why no comprehensive study of clathrin at the spindle was carried out until Royle *et al* (2005). The depletion of CHC using RNAi induced a number of mitotic defects. First, problems with chromosome congression,

demonstrated by a disorganised metaphase plate and an increase in the number of cells with misaligned chromosomes. Second, an increase in inter-kinetochore distance as a consequence of a reduction in K-fibre tension (Waters et al., 1996). Third, a twofold reduction in proliferation, as a result of an increase in the mitotic index, i.e. cells had difficulty progressing through mitosis. These mitotic defects could be attributed to destabilised K-fibres, demonstrated by a loss of kinetochore attachment or a lack of tension, leading to the continued activation of the spindle checkpoint (Royle et al., 2005). A role of clathrin in mitosis is further supported by similar results observed in tobacco BY-2 cells (Tahara et al., 2007), porcine oocytes (Holzenspies et al., 2010) and other human studies (Fu et al., 2010, Lin et al., 2010).

1.6.4 The function of clathrin in mitosis is distinct from membrane trafficking

As clathrin plays an essential role during membrane trafficking it has been tested whether the defects observed during mitosis, following RNAi, were just an extension of this function, rather than an isolated one. First, clathrin at the spindle is not thought to be associated with vesicles. Although the occasional study has reported the presence of CCVs in the spindle (Robbins and Jentzsch, 1969) these were not found to be enriched. This is the case with membranes in general, tested by the labelling of membranes with an amphiphilic styryl dye (FM4-46), which found no membranes in the spindle region (Waterman-Storer et al., 1993, Royle et al., 2005). Membranes, although present in mitosis, are generally excluded from the spindle apparatus (Tooze and Hollinshead, 1992) and found more at the cell periphery, where they are thought to play a role in mitosis through intracellular partitioning (Zheng, 2010). Second, if the clathrin enriched at the spindle was

assembled into coated vesicles then major endocytic adapters should also be present (Robinson, 2004). This was tested using indirect immunofluorescence, where none of AP-1, AP-2 or AP-3 were present at the spindle (Royle et al., 2005). Third, a clathrin mutant was generated that could not function in endocytosis, but could rescue mitosis (Royle and Lagnado, 2006). Another clathrin mutant has been tested that cannot localise to microtubules but can still function in endocytosis (Hood and Royle, 2009). More recently, clathrin mutants that can only dimerise and therefore not assemble into a coated lattice, could still function in mitosis (Blixt and Royle, 2011). Collectively, these data imply that clathrin at the spindle is functioning independently from its role in membrane trafficking.

Royle *et al*. showed that the NTD is required for spindle binding multimerising is required for mitotic function, they hypothesised that this would allow clathrin to cross-link MTs of the spindle.

1.6.5 Clathrin as an inter-MT bridge

There are several lines of evidence that suggest clathrin could act as an inter-MT bridge, the first test however was to assess whether clathrin localises specifically with K-fibres.

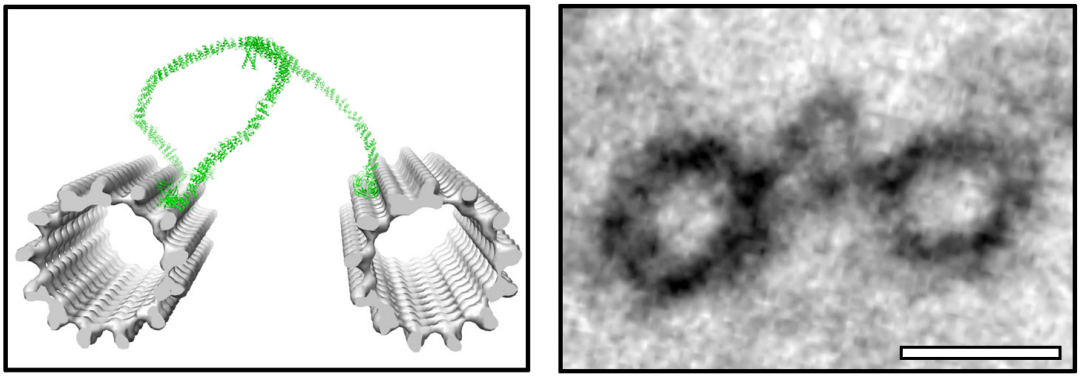

Figure 1.8 – Clathrin is a candidate for an inter-MT cross-linker in K-fibres. A scaled atomic model of how clathrin may cross-link microtubules (**left**) and an electron micrograph showing an inter-kMT bridge (**right**), taken from the K-fibre of an orthogonally sectioned, resin embedded HeLa cell. Scale bar, 25 nm.

This was confirmed by the cold-treatment of mitotic cells to depolymerise all other MT subtypes, followed by anti-clathrin immunocytochemistry (Royle et al., 2005).

Second, replacement experiments expressing clathrin mutants have been carried out, where several observations were noted, including: a clathrin mutant lacking the N-terminal 'foot' domain, could not localise to the spindle or rescue mitosis; a mutant containing the NTDs but lacking a trimerisation domain was able to localise to the spindle but could not function in mitosis; a 'stunted' clathrin mutant that contained both the N terminal and trimerisation domains, but lacked a significant fragment of 'leg', was able to localise to the spindle and rescue mitosis (Royle et al., 2005). Interestingly this mutant was not able to function in endocytosis, but could still function in mitosis (Royle and Lagnado, 2006). These results suggest that trimeric clathrin, containing essential regions of the NTD, are capable of functioning to promote K-fibre stability (Royle and Lagnado, 2006). This observation has been reproduced and studied more recently, where dimeric clathrin mutants have also been shown to function in mitosis (Blixt and Royle, 2011). This functional data shows that the mere presence of clathrin at kMTs is not sufficient for it to participate in spindle stability, rather it has to multimerise into a protein assembly capable of localising and binding to, more than one MT at once, moreover its localisation suggests it could be a bridge in K-fibres. The third piece of evidence was a more direct test using cryo-electron microscopy (EM) and immunogold labelling. Here, clathrin was localised to areas close to and between kMTs (Royle et al., 2005). Unfortunately, although this method of EM is good for immunogold labelling, the resolution of fine structures is sometimes compromised, therefore the bridges themselves cannot be identified in the representative micrographs. In contrast, an inter-kMT bridge, prepared using resin-embedding, reveals bridges comparatively

similar to a scaled model of a clathrin/MT assembly (**Figure 1.8**). It appears that this type of direct testing, analysing the bridges ultrastructurally, provide the best evidence for screening bridge candidates.

1.6.6 Clathrin requires MT binding partners to localise to the spindle

Clathrin alone cannot directly bind to microtubules *in vitro*, rather, it requires the presence of mitotic cytosol (Booth et al., 2011). This suggests that, much like the clathrin in membrane trafficking, adaptors are required for the alternative function of clathrin at the spindle. Several independent groups have shown clathrin at the spindle to be in a complex with two other spindle proteins; transforming acidic-coiled coil protein 3 (TACC3) and colonic-hepatic tumour overexpressed gene (ch-TOG) (Booth et al., 2011, Fu et al., 2010, Hubner et al., 2010, Lin et al., 2010). Using quantitative proteomics, Hubner *et al*. tested for phosphorylation-specific interactors of TACC3 and identified clathrin (Hubner et al., 2010). Lin *et al*. confirmed this association *in vitro* using truncated glutathione S-transferase (GST)-TACC3(522-577) fusion proteins. This truncated region is thought to contain an essential Aurora A kinase phosphorylation site at serine558. The recombinant GST-TACC3 was phosphorylated with Aurora A kinase before incubation in mitotic extracts from synchronised HeLa cells. An immunoprecipitation (IP) of GST-TACC3 (but not a non-phosphorylatable mutant) identified a single band of >170 kD. This was confirmed as clathrin using mass spectrometry (Lin et al., 2010). These data also suggest that the TACC3/clathrin association is mediated by phopho-S558 of TACC3 and no other potential Aurora A phosphorylation sites. Fu *et al*. identified clathrin as a TACC3 binding partner through a similar method to Lin *et al*,

only using Xenopus TACC3 (maskin) and Xenopus cytostatic factor (CSF) extract (Fu et al., 2010).

Of these four studies, Booth *et al*. was the only one to isolate and purify the native TACC3/ch-TOG/clathrin complex, from mitotic spindle preparations. This complex was only found to be present at the spindle and not assembled in the cytosol (Booth et al., 2011).

1.6.6.1 TACC3 RNAi phenotype is similar to clathrin but not ch-TOG

TACC3 depletion causes mitotic defects that include; misaligned chromosomes, issues with chromosomes congression and continued activation of the spindle checkpoint (Gergely et al., 2003, Booth et al., 2011). This is a strikingly similar phenotype to that seen following clathrin RNAi (Royle et al., 2005). The mitotic defects associated with the individual depletion of either TACC3 or clathrin are equivalent to the depletion of both proteins together (Lin et al., 2010). Although chTOG-depleted cells exhibited similar types of defects, the severity of these was far greater, including; a five fold increase in the mitotic index and poorly assembled spindles as a result of chromosome misalignment and extra cell poles (Gergely et al., 2003). These data suggest that clathrin and TACC3 work in cohort to promote K-fibre stability and that independent roles are unlikely. In contrast, although ch-TOG is clearly associated with the TACC3/chTOG/clathrin complex it is likely that ch-TOG also fulfills extra roles, since it induces additional, different mitotic defects. Interestingly, the depletion of either ch-TOG or TACC3 results in a decrease in K-fibre intensity, as shown by fluorescence of tubulin, suggesting a loss of kMTs or at least a decrease in kMT organisation (Gergely et al., 2003). The basis of these results is not clear and no ultrastructural work has been carried out.

1.6.6.2 Recruitment of the TACC3/ch-TOG/clathrin complex

Whilst the four groups that identified the TACC3/ch-TOG/clathrin complex are in agreement that spindle clathrin is in a complex with TACC3 and ch-TOG, the order of recruitment to the spindle is contentious.

There are two models for the recruitment of the TACC3/ch-TOG/clathrin complex to K-fibres. In the first, clathrin recruits TACC3 and ch-TOG to kMTs (Lin et al., 2010, Fu et al., 2010, Hubner et al., 2010), in the other, TACC3 is the primary recruitment factor (Booth et al., 2011). The best evidence for clathrin as the mediator of recruitment is that, depletion of clathrin reduces the amount of TACC3 at the spindle (Lin et al., 2010, Hubner et al., 2010, Fu et al., 2010, Booth et al., 2011), however, this is contradicted by other results suggesting it is TACC3 that is the primary recruitment factor. The depletion of TACC3 has been shown to block clathrin recruitment (Booth et al., 2011). Furthermore, the overexpression of TACC3 enhances clathrin recruitment to the spindle, whereas overexpression of clathrin has no effect on TACC3 recruitment (Booth et al., 2011). In addition, clathrin cannot bind directly to microtubules, instead, it requires the presence of mitotic cytosol (Booth et al., 2011). In contrast, maskin, a TACC3 homolog expressed in *Xenopus*, can bind directly to microtubules, with an equivalent K_d to other MAPs (Peset et al., 2005, O'Brien et al., 2005)

The role of ch-TOG in the recruitment of the complex components is currently more vague, where the overexpression does not enhance the recruitment of other complex members and depletion of ch-TOG induced some reduction in TACC3 or clathrin recruitment, but was less pronounced (Booth et al., 2011). More work is required to refine the models for the recruitment of the TACC3/ch-TOG/clathrin complex to the spindle (Hood and Royle, 2011).

2 Chapter 2: Materials and Methods

2.1 Molecular biology

2.1.1 Reagents

Wizard® Plus SV Miniprep Kit (#1581MB09_9A) was purchased from Promega (Southampton, UK). Midiprep (#27106), gel extraction (#28604) and PCR purification (#28704) kits were all obtained from QIAgen (Crawley, UK). All restriction enzymes: *Hin*dIII, *Bgl*II, *Eco*RI, *Nhe*I and *Apa*LI; NEB buffers; Quick-Loading 1kb DNA ladder (#NO468G); calf intestinal phosphatase (#M0290S); T4 polynucleotide kinase buffer (#B0201S); T4 polynucleotide kinase (#M0201S); Quick ligase buffer (#B2200S); Quick ligase (#M2200L); $MgSO_4$ (#B0254S) were purchased from New England BioLabs (Hertfordshire, UK). Bovine serum albumin (BSA) (#A8022); Kanamycin disulfate salt (#K1876); Tryptone (#T9410); sodium chloride (#S8875); Trizma®base (T1503); ethylenediaminetetraacetic acid disodium salt dihydrate (EDTA) (#E1644) and all oligonucleotides were ordered from Sigma Aldrich (Poole, UK). Yeast extract (#BP1422) and boric acid (#B376053) were obtained from Fisher Scientific (Loughborough, UK). Pfu Turbo® DNA polymerase (#600250-52) and Pfu 10X reaction buffer (#600152-82) were obtained from Agilent (Edinburgh, UK).

2.1.2 Generation of DNA constructs

The molecular biology carried out during this project was focused on generating two classes of DNA construct: 1) pBrain-GFP-shRNA and 2) pTRE2hyg-GFP-TACC3(KDP).

The rationale for using the pBrain series of vector was to generate a dual promoter plasmid capable of expressing an shRNA together with a fluorescent reporter. To express shRNA targeting TACC3 or ch-TOG, complementary sense and anti-sense oligonucleotides were designed. These were annealed to become a double stranded DNA cassette that could be directly ligated into a pBrain-SpH vector. The oligonucleotide RNAi regions were designed according to published sequences where efficient knock down had been reported (Gergely et al., 2003). This pBrain-SpH-shRNA vector expressed synapto-pHluorin (SpH) as the fluorescent reporter. A fragment of pBrain-SpH-shRNA was removed and inserted into a pEGFP-C1 vector, to change the fluorescent reporter to give pBrain-GFP-shRNA (**Figure 2.1 A**). See **4.3.1** for a more comprehensive methodology.

The pTRE2hyg-GFP-TACC3(KDP) vector (**Figure 2.1 B**) is compatible with HeLa Tet-On® cells from Clontech (Mountain View, CA, USA), allowing the stable inducible expression of proteins. The construct was generated using polymerase chain reaction (PCR) to amplify a GFP-TACC3(KDP) cassette out of a plasmid (available from previous work in the laboratory) and insert it into a pTRE2hyg vector (Clontech). See **2.2.6** for a more comprehensive methodology.

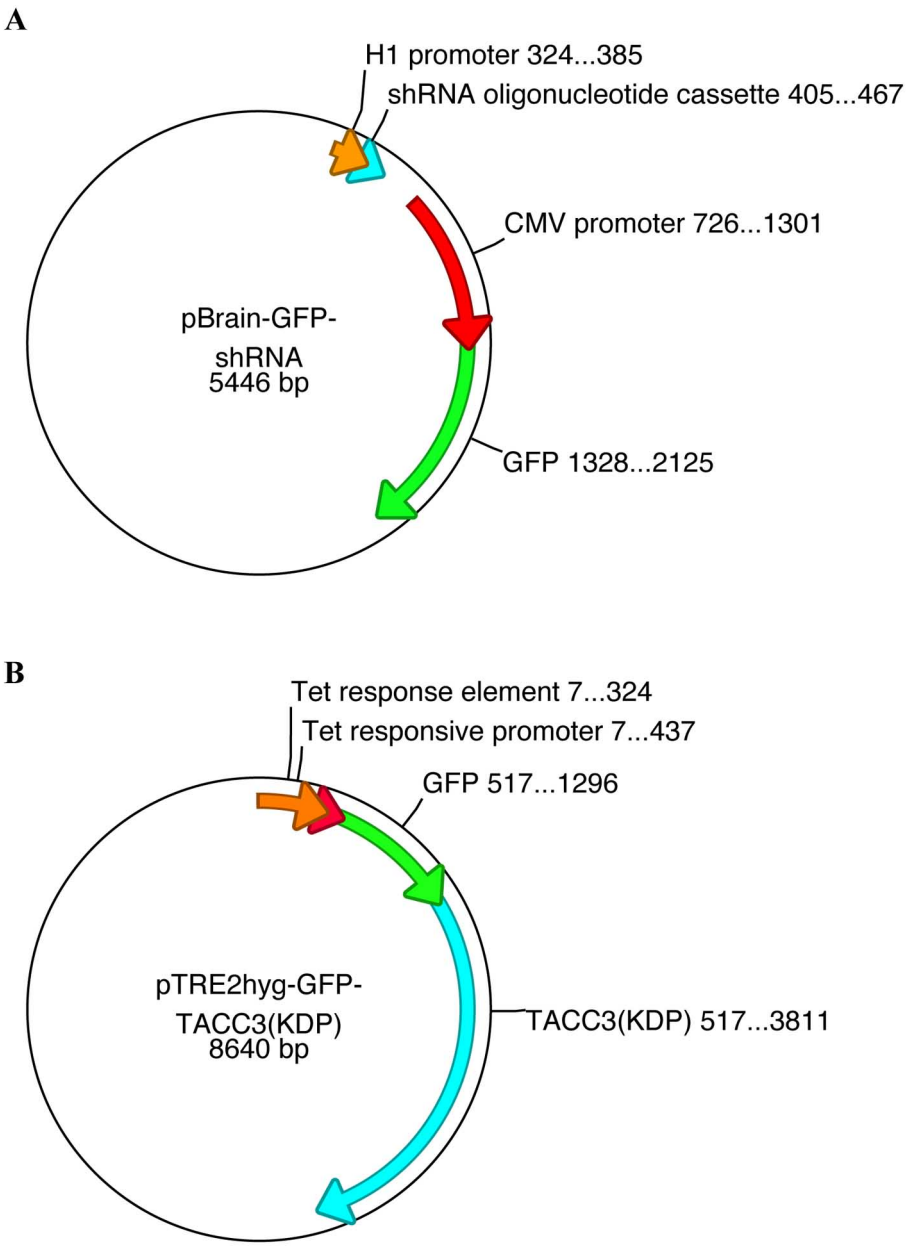

Figure 2.1 – Vector maps for pBrain-GFP-shRNA and pTRE2hyg-GFP-TACC3(KDP). (A) pBrain-GFP-shRNA individually expresses GFP (green) and an shRNA (cyan) under the control of H1 (orange) and CMV (red) promoters. **(B)** pTRE2hyg-GFP-TACC3(KDP) contains a Tet (tetracycline) response element (orange) that, once introduced into TetOn HeLa cells, allows the inducible expression of a gene of interest (green and blue). Schematic maps were created using ApE v2.0.36.

2.1.3 PCR amplification of DNA

DNA was amplified by PCR using a Techne TC-312 thermocycler, in the following 50 µl reaction: DNA template, 100 ng; deoxyribonucleotide triphosphate (dNTP), 2.5 mM; 10X Pfu reaction buffer, 5 µl; DMSO, 5% v/v; magnesium sulfate ($MgSO_4$), 1.0 mM; sense and anti-sense oligonucleotide primers, 0.5 µM; Pfu Turbo® DNA polymerase, 2.5 U; to a final volume of 50 µl using dH_2O. The thermocycler parameters were set as:

- Denaturing - 95°C, 40 s
- Annealing - primer Tm –5°C, 1 min
- Extension – 72°C, 1 min per 1 kb DNA
- Cycles - 36

Prior to usage, the DNA products amplified by PCR were resolved using agarose gel electrophoresis, extracted from the gel and finally, purified.

2.1.4 Separation of DNA by agarose gel electrophoresis

Gels were prepared by combining electrophoresis grade agarose (0.8 - 1.1% v/v) with 100 ml 0.5X TBE (Tris-base, 45 mM; boric acid, 45 mM; EDTA, 10 mM, pH 8.3), the solution was heated in a microwave until the agarose was fully dissolved. Ethidium bromide was added to a concentration of 0.5 µg/ml. The gel was poured into a mould and left to set at room temperature. Samples were mixed with 6X loading buffer (bromophenol blue, 0.25%; xylene cyanol FF, 0.25%; glycerol, 30%; in water) and the DNA resolved in a horizontal midi electrophoresis tank containing 0.5X TBE, at ~100 V using a BioRad PowerPack™. A 1 kb DNA ladder standard was loaded along side the test samples. The DNA was visualised

using an ultra violet (UV) light source. If the DNA was required for further stages of cloning, gel extraction and purification of the appropriate band was performed.

2.1.5 Extraction of DNA from agarose gels

All centrifugations during the QIAquick Gel Extraction Kit (Qiagen) purification were for 1 min at 16,000 x g unless otherwise stated. The appropriate band was excised from an agarose gel and dissolved in Buffer QG at 50°C. The DNA was precipitated using isopropanol before collection in the membrane of a QIAquick spin column, by centrifugation. DNA was washed using 750 µl of Buffer PE. The flow through was discarded and the column centrifuged once more, removing any remaining residual ethanol that was present in the wash buffer. The DNA was eluted into a clean 1.5 ml microfuge tube with 50 µl of Buffer EB and centrifugation. DNA abundance was estimated by measuring the optical density of the DNA solution at 260nm wavelength (OD_{260}), using a spectrophotometer (Eppendorf, BioPhotometer).

2.1.6 Restriction endonuclease digestion of DNA

The digestion of DNA, using restriction enzymes, was carried out in either 50 µl or 10 µl reactions, depending on the intended use of the DNA. The lower volume 'test digest' was used to screen vectors for successful insertion of DNA cassettes, whereas the larger volume reactions were carried out when the DNA was used in the generation of a construct. A typical 50 µl digestion reaction would contain the following (scale down appropriately for smaller volume digestions): DNA, 1 µg; 10X NEB buffer, 5 µl; bovine serum albumin (BSA), 5 µg; restriction enzyme, 10 U; make up to 50 µl using water. The reaction was incubated at 37°C for

2 h. In the case of vector digestions, 10 U of calf intestinal phosphatase (CIP) was introduced after ~1.5 h.

2.1.7 Ligation of DNA insert into vector

A typical 21 µl ligation reaction was made up as follows: vector, 1 µl (or 50 ng); DNA insert, 2 µl (or a 1:3 molar ratio of vector:insert); water, 7 µl; Quick ligation buffer (2X), 10 µl; Quick ligase, 1 µl. The reaction was incubated at room temperature for 10-15 min. A negative control of digested vector only (1 µl vector and 9 µl water, i.e. no DNA insert), was also assembled in preparation of transformation into ultra-competent bacteria.

2.1.8 Bacterial transformation of DNA constructs

Post-ligation, DNA constructs were amplified by transformation into chemically ultra-competent E-Coli DH5α bacteria (donated by Maria Blixt) using the following protocol: 100 µl of DH5α bacteria was added to 1 µl of ligation mix and chilled on ice for 30 min prior to a 42^{o}C heat shock for 42 s, this was followed by an immediate cooling on ice (2 min). The solution was made up to 1 ml by the addition of 900 µl room temperature antibiotic free Luria-Bertani (LB) media (1% tryptone, 0.5% yeast extract, 1% NaCl, made up in water, pH7.0). The transformations were cultured in an orbital shaker for 1 h at 37^{o}C, 200 rpm, before centrifugation (7,000 rpm, 2 min). A majority of supernatant (900 µl) was removed and discarded, the remaining ~100 µl of LB was used to resuspend the bacterial pellet. The transformed bacterial concentrate was transferred onto an LB agar plate containing the appropriate antibiotic (kanamycin or ampicillin, both 50 µg/ml) and spread using a sterile glass rod. Agar plates were incubated overnight at 37°C.

The following morning, single colonies were selected and removed using a 10 µl pipette tip, suspended in 5 ml LB (containing 50 µg/ml of appropriate antibiotic) and incubated overnight in an orbital shaker (37°C, 200 rpm).

2.1.9 Recovery of DNA from bacterial cultures

Depending on the scale of bacterial culture either a Wizard® Plus SV Miniprep Kit or Qiagen HiSpeed Midi Kit was used for the recovery of DNA. Miniprep kits were used when DNA was required for cloning and midi-kits were used when the DNA was required for transfection.

Prior to DNA recovery, 850 µl of bacterial culture was retained and combined with 150 µl glycerol. With the glycerol serving as a cryo-protectant, the DNA transformed bacterial stock was stored at -80°C.

2.1.9.1 Wizard® Plus SV Miniprep Kit

All centrifugations were for 1 min at 16,000 x g and at room temperature (RT) unless otherwise stated. Bacterial culture (1-5 ml) was pelleted by centrifugation for 5 min at 10,000 x g. The supernatant was discarded and 250 µl of cell re-suspension solution added. Pellets were completely resuspended by vortex or pipetting. Cell lysis solution was added (250 µl) and the sample incubated at RT until the suspension cleared (1-5 min). Following the introduction of 10 µl alkaline phosphatase, neutrilisation solution was added (350 µl). The cleared lysate was decanted into a spin column and centrifuged for 10 min. The DNA retained in the spin column membrane was washed using 750 µl and then 250 µl of column wash solution. Following wash centrifugations the spin column was transferred to a clean 1.5 ml microfuge tube and the DNA eluted in 100 µl of nuclease free water by centrifugation. DNA abundance was measured using a spectrophotometer.

2.1.9.2 Qiagen HiSpeed Midi Kit

The bacterial culture (~100 ml) was pelleted by centrifugation at 4°C for 15 min at 6000 x g. The supernatant was discarded and the pellet homogenously resuspended in 4 ml Buffer P1, added to this was 4 ml of Buffer P2. The bacterial lysate was mixed thoroughly and incubated at RT for 5 min after which 4 ml of chilled Buffer P3 was added. The bacterial lysate was decanted into a QIAfilter Cartridge and left for 10 min, during which time a HiSpeed Midi Tip was equilibrated by applying 4 ml of Buffer QBT. The column was allowed to empty by gravity flow. The bacterial lysate was then filtered through a QIAfilter Cartridge into the previously equilibrated HiSpeed Tip using a syringe. The cleared lysate was allowed to enter the resin by gravity flow. The HiSpeed Tip was washed with 20 ml of Buffer QC after which the DNA was eluted using 5 ml of Buffer QF. The eluted DNA was precipitated using 3.5 ml of isopropanol, mixed and left to incubate at RT for 5 min. The DNA precipitate was transferred into a QIAprecipitator where it was washed with 2 ml of 70% ethanol, it was then eluted using 1 ml of Buffer TE.

2.2 Cell Biology

2.2.1 Reagents

All cell culture reagents were obtained from Sigma Aldrich (Poole, UK), unless otherwise stated and all plasticware was purchased from Greiner bio-one (Gloucester, UK) unless otherwise stated. GeneJuice (#D00109034) and Oligofectamine (#679208) were purchased from Novagen (distributed by Merck Chemicals Ltd., Nottingham, UK) and Invitrogen (Paisley, UK), respectively.

2.2.2 Cell lines

HeLa cells are a human cell line derived from epithelial cervical carcinoma. HeLa cells (#93021013) were purchased from HPA Cultures (Solisbury, UK).

HeLa Tet-On cells® (Clontech) are a human cervical epithelioid carcinoma-derived cell line that expresses the reverse tetracycline - controlled transactivator (rtTA). An inducible, gene expression system can be generated by stably transfecting these cells with a plasmid that expresses the gene of interest under the control of a Tet Response Element (TRE), (see **2.2.6** for the methodology used to generate a stable cell line).

2.2.3 Cell culture

Cells were routinely cultured at 37°C in a humidified 5% CO_2 incubator in plastic tissue culture flasks containing Dulbecco's Modified Eagle's Medium (DMEM) (Invitrogen), supplemented with 10% foetal bovine serum (FBS) and 1% penicillin/streptomycin sulphate. In the case of HeLa Tet-On cells, the medium was also supplemented with G418 (300 μg/ml).

Adherent cells were passaged upon reaching 80 – 95% confluency using 0.25% trypsin EDTA (#T4049). To passage, the cell media was removed and cells washed with warm phosphate buffered saline (PBS) (Fisher Scientific), before incubation in trypsin EDTA at 37°C until the cells had become detached. Cells were resuspended in fresh DMEM (containing supplements) and re-seeded into a new flask at an appropriate density (typically a 1:10 dilution).

2.2.4 Transfection of DNA plasmids

Cells were transfected using the lipid transfection reagent GeneJuice (#70967, Merck Biosciences). Cells were seeded into a 12 well plate (containing

glass coverslips when necessary) 24 hours prior to transfection. On the day of transfection the cell media was replaced with 1 ml fresh DMEM (containing supplements) and the following protocol used per well: 1.5 µl of GeneJuice was added to 50 µl of Optimem (Invitrogen) and incubated for 10 min; 0.5 µg of DNA was added and incubated for a further 10 min. The transfection solution was added to the cells and the plasmid left to express for an appropriate length of time.

2.2.5 Transfection of siRNA

The procedure for transfecting cells with siRNA was as follows: 17 µl of oligofectamine (Novagen) was added to 73 µl of Optimem media (containing no supplements), in parallel, 11 µl of siRNA (20 µM), was added to 1000 µl of Optimem media. Both the oligofectamine and siRNA solutions were left to incubate separately for 10 min. The two solutions were then combined and incubated for a further 10 min. The transfection solution was added to the 10 cm dish (making a total volume of ~5.5 ml). The media was replaced with fresh DMEM (containing supplements) after 6 hr. Cells were left to allow protein depletion for the appropriate amount of time, in the case of TACC3 this was 72 hr.

2.2.6 Generation of a stable cell line

HeLa TetOn® pTRE2hyg-GFP-TACC3(KDP) cells are a dual stable HeLa cell line capable of expressing GFP-TACC3(KDP) after induction using doxycycline (doxycycline was a gift from Professor Bill Earnshaw, University of Edinburgh). This cell line was generated by stably transfecting HeLa TetOn® cells with a pTRE2hyg-GFP-TACC3(KDP) construct, as described in **2.2.4** (scaled for a 10 cm dish). Following a 48 h expression period the cell medium was supplemented with

G418 (300 µg/ml and hygromycin (200 µg/ml). The antibiotics killed any cells that were not stable TetOn® HeLas or stable with pTRE2hyg. Selection was carried out over a course of 7-14 d, until colonies of cells (comprising ~100 – 200 cells per colony) could be seen under a tissue culture dissection microscope. Approximately 75 individual, lightly trypsinised colonies were picked using a 10 µl pipette tip and suspended (in fresh DMEM containing G418 and hygromycin) into a 12 well plate, one colony per well. Over a number of days the colonies were expanded, first into a 6 well plate and eventually into 10 cm dishes. During passaging a small proportion of cells were seeded onto glass coverslips and screened for stable expression and functionality of GFP-TACC3(KDP) using fluorescence microscopy (**2.3.2.1)** following induction with doxycycline (0.5 µg/ml, 24 h). As a result of the fluorescence screen it was possible to identify six appropriate clones, these were chosen for continued culturing, in addition, liquid nitrogen stocks were also created (see below). The remaining clones were discarded.

2.2.6.1 Generating liquid nitrogen cell stocks

Cells in a confluent T75 flask were trypsinised as described in **2.2.3**, but rather than passaging, the trypsinised cells were centrifuged (300 x g, 2 min) and resuspended in 10 ml ice cold cell storage medium (70% DMEM, 20% FBS, 10% sterile glycerol). Resuspended cells were aliquoted into Cryo.s vials (#E110103G) and steadily chilled to -80°C using a Tarsons Cryo 1°C Cooler, after which the vials were transferred into a liquid nitrogen Dewar for long-term storage.

2.3 Microscopy

2.3.1 Reagents

Paraformaldehyde powder (#15812-7) was purchased from Sigma Aldrich (Poole, UK). Microscope slides (#ISO 8037/1) were purchased from Thermo Scientific. Triton X 100 (#BP151-500) was purchased from Fischer Scientific.

All reagents for TEM were purchased from Agar Scientific (Essex, UK) unless otherwise stated. The Dip Miser Set (#T083) was purchased from ProSciTech (Thuringowa, Australia).

2.3.2 Light Microscopy

2.3.2.1 Routine fixation and mounting

Cells were fixed using paraformaldehyde (3% PFA, 4% sucrose in PBS) at RT for 15 min or using 100% methanol for 15 min at -20°C. Cells were washed with PBS before the cover slips were mounted onto glass slides using mowiol (a gift from Samantha Williams). The mountant was left to set at RT overnight.

2.3.2.2 Indirect immunofluorescence

Following fixation, cells were washed in permeabilising solution (0.5% Triton-X100 in PBS) for 10 min at 4 °C after which cells were washed twice with PBS and incubated in blocking solution (3% BSA, 5% goat serum in PBS) for 1-2 h. Cells were incubated with the appropriate primary antibody in blocking solution for 1 h, after which three x 5 min PBS washes were carried out. Cells were incubated with the appropriate secondary antibody in blocking solution for 1 h, after which the cover slips were washed with PBS (3 x 5 min) and mounted as described in **2.3.2.1**.

2.3.3 Electron Microscopy

2.3.3.1 Preparation of formvar coated copper grids

Hexagonal 200 mesh copper grids (#G2410C) were coated with formvar (#T083) (0.2% formvar in 100% chloroform). A new glass slide was polished using chamois leather before being inserted into a Dip Miser containing formvar. The glass slide was withdrawn from the Dip Miser at an appropriate speed, generating a slide homogenously coated with a thin layer of formvar plastic. Once dry, the edges of the formvar coat were scored using a razor and the slide immersed in water, allowing the plastic coat to become detached from the glass slide and reside on the surface of the water. Factory fresh copper grids were transferred onto the plastic using forceps before being collected onto a new, clean, glass slide. Coated grids were left to dry for at least 2 h before use.

2.3.3.2 Correlative light electron microscopy (CLEM) processing

HeLa cells were seeded and transfected with the appropriate DNA plasmids (**2.2.4**) and left to express for an appropriate length of time. The day prior to CLEM processing, cells were split into glass bottomed, gridded dishes (MatTek Corporation, USA), for the rest of the thesis these will be referred to as CLEM dishes. On the day of CLEM processing, the appropriate reference images were taken using a Nikon TE2000U microscope allowing the correlative identification of cells of interest, at a later date, by electron microscopy. On completion of imaging, cells were fixed for 1-2 h (2.5% glutaraldehyde, 1.5% paraformaldehyde, in 0.05 M PB containing 5 µg/ml dapi). Following fixation, samples underwent routine electron microscopy processing. Cells were washed in buffer A (0.1 M sucrose in 0.05 M PB) before osmication (1% osmium tetroxide in buffer A) for 1 h, after

which samples were washed, firstly using buffer A (3 x 20 min) and secondly with ddH_2O (2 x 20 min). Cells were then washed in 30% ethanol (30 min) before incubation in uranyl acetate (0.5% in 50% ethanol) for 1 h, after which cells were dehydrated in a series of eight graded ethanol washes (30 - 100%) at 5 – 10 min per incubation. Samples were incubated in 100% ethanol (2 x 20 min) followed by infiltration with ethanol:resin mixes (2:1 and 1:1 respectively) for 20 min per mix, before being covered in 100% resin. At this stage cells were left for 30 min before curing at 60°C for ~48 h.

If cells were to be analysed longitudinally, then prior to placement in the oven, a gelatin capsule (#G29211) of resin would be placed on top the cell(s) of interest. Following resin polymerisation, samples were trimmed and sectioned using a Leica UC 6 microtome and DiATOME Ultra diamond knife. Before TEM, the grids were routinely post-stained using lead citrate and uranyl acetate (5% in 50% ethanol). See Chapter 3 for comprehensive details on CLEM processing.

2.3.3.3 Immunogold labelling

HeLa cells were seeded into CLEM dishes and transfected (as described in **2.2.4**) with plasmids expressing GFP-CHC or GFP-α-Tubulin. Following a 48 h expression period the cell media was supplemented with taxol (5 µg/ml) for 5 min (37°C). DMEM was removed and cells incubated in 1 ml of PTEML buffer (PIPES, 50 mM; EGTA, 10 mM; MgCl2, 1 mM; Triton X-100, 0.2%; latrunculin B, 2 µg/ml; protease inhibitor cocktail, 1X; okadaic acid, 100 nM; beta-glycerophosphate, 20 mM; Taxol, 5 µg/ml) for 5 min. PTEML buffer was removed and the cells fixed (1.5% glutaraldehyde, 2.0% paraformaldehyde in 0.05 M PB) for 1 h. Following two x 5 min washes in buffer A cells were incubated in 1 ml of blocking solution for

1.5 h after which cells were labelled with one of: anti-GFP, anti-CHC (X22) or anti-α-tubulin primary antibodies in blocking solution for 1 h. Cells were washed in buffer A three x 5 min, before incubation in the appropriate gold-conjugated secondary antibody, in block, for 1 h. Following secondary antibody labelling the cells were washed with buffer A (three x 5 min) and post-fixed (3% glutaraldehyde in buffer A) for 15 min. At this stage, cells exhibiting spindle GFP fluorescence were chosen for CLEM using a Nikon TE2000U microscope and subjected to EM processing and resin embedding (as described in **2.3.3.2**). Following resin polymerisation, samples were trimmed and sectioned using a microtome and diamond knife. See Chapter 3 for more comprehensive details on CLEM processing.

2.3.3.4 Preparation of cells for high pressure freezing (HPF) and Freeze substitution (FS)

Cells were seeded into 10 cm dishes and synchronised to enter mitosis at the time of HPF. Cells were treated with 2 mM thymidine for 19 h, washed (with PBS) and released for 7 h, before incubation in 40 ng/ml nocodazole for 12 h. Cells were released from the nocodazole block for ~40 min, allowing an enriched population of cells in metaphase to be harvested using a mitotic shake-off. The media was collected and cells pelleted by centrifugation (2 min, 300 x g). The supernatant was removed and the cells resuspended in 10 µl of DMEM (containing 20% BSA). At this point the cells were ready for freezing using a Leica EM PACT2 and its associated equipment. To freeze, 0.5 µl of cell suspension was added to the indent of a HPF copper disk. The copper disk was inserted into a rapid loader and fed into the Leica HPF. The pressure-frozen cells were transferred, in liquid nitrogen, to a freeze substitution robot (Leica) for staining, dehydration and embedding in resin.

2.4 Data Collection and Analysis

2.4.1 Longitudinal analysis of inter-microtubule bridges by TEM

Random areas of the spindle were chosen at a low magnification (~12,000 x), after which a high magnification 4x4 multiple image alignment (MIA) was taken at 60,000 x. Images were taken at 100 kV using an FEI Tecnai G2 Spirit BioTWIN microscope. Following image capture the MIAs were analysed using AnalySIS® (Soft Imaging System). The following were measured: total microtubule (MT) length, paired MT length (regions of single MTs within 80 nm bridging distance of each other), bridge frequency and length of inter-MT bridges. Data were imported into Microsoft Excel spreadsheets where parameter means and SEM were calculated. Multi-peak fitting was done using Multipeak Fitting 2 in Igor Pro 6.12. Data analysed using Igor Pro was carried out by or with the help of, Steve Royle.

2.4.2 Orthogonal analysis of kinetochore fibre microtubules

K-fibres within 1.5 μm of the metaphase plate were imaged using a single-axis tilt series. An audio-visual interleave (*.avi) file of the tilt was imported into ImageJ where MTs were mapped and annotated allowing a matrix of co-ordinates to be generated. Using this matrix, the inter-MT distance, MT frequency and K-Fibre cross-sectional area were calculated.

2.4.3 Gold particle quantifications

Immunogold labelling of GFP-α-tubulin and GFP-CHC was quantified using a similar method to **2.4.2**, where a matrix was created based on the positions of four monitored coordinates **(Figure 2.2)**: 1) A gold particle. 2) The nearest MT. 3) The nearest MT on the opposite side of the gold particle. 4) The nearest bridge.

2.4.4 Tomography and 3D rendering

Tilt series of resin sections were acquired using a tilt range between -60° and +60°. All *.mrc files (the output file produced when generating a tilt series) were reconstructed into tomograms using IMOD 4.1 (Boulder Laboratory for 3-Dimensional Electron Microscopy of Cells and the Regents of the University of Colorado). Serial join tomography was carried out using the 'tomogram join' sister-software of IMOD. All *.rec files (the output file format of IMOD) were rendered into 3D models using the Amira 3.1 software package.

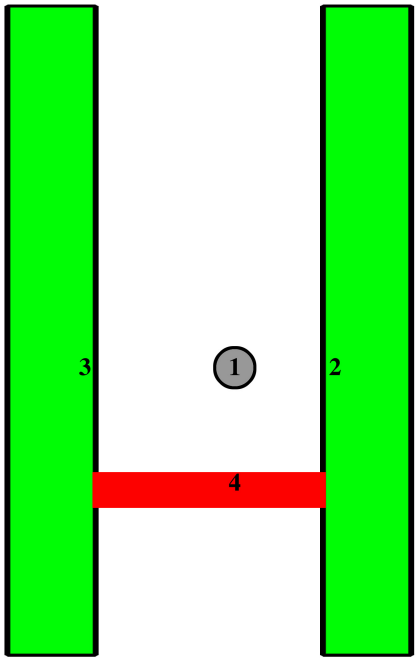

Figure 2.2 – Method for gold labelling quantifications. A schematic to show the parameters measured for immunogold labelling. The coordinates of four parameters were taken: 1) Gold particle. 2) The nearest MT. 3) The nearest MT on the opposite side of the gold particle. 4) The nearest bridge. These coordinates allowed a number of parameters to be calculated, including: proximity of gold particles with bridges and MTs, gold particles found between paired MTs.

2.4.5 Statistical testing

Throughout this PhD the data collected was subjected to statistical testing. For the most part either the mean (average) or median (numerical value separating the higher half of a sample from the lower of half) was sufficient, however, when a value of significance was required, then a students t-test was calculated using Microsoft Excel. A statistical significance value was set at $p=<0.05$. A Ripley's L function was used in Chapter 5 for detecting deviations from spatial homogeneity. Using this test the Euclidean distance between microtubules of K-fibers from control samples was compared from those of 'test' samples. Any statistical tests used during this thesis are referred to in the text or figure legends.

3 Chapter 3 – Establishing and optimising a series of EM techniques to analyse kMTs and inter-MT bridges

3.1 Introduction

In order to investigate the function of clathrin in mitosis, the ultrastructure of the spindle apparatus needed to be analysed by TEM. Two problems meant that it was not possible to take cells at random for this analysis. First, in an asynchronous population of cells, mitotic cells make up ~4% of the population, with only one third of these at the appropriate stage of mitosis (Robbins and Marcus, 1964). Second, in order to deplete a protein, certainty of efficient knockdown was required. To overcome these issues, correlative light electron microscopy (CLEM) was employed. CLEM is a powerful multimodal technique used to visualise cells at two levels of resolution. Light microscopy (LM) is a powerful tool in its own right, where multi-channel labelling allows cellular interactions and dynamics to be observed, however, a lack of fine detail can be an issue, where the ~200 nm resolution limit of conventional light microscopy, means a concentrated fluorescent area/spot could represent an organelle sub-domain, protein aggregate or even a whole organelle (van Rijnsoever et al., 2008). Electron microscopy (EM) has nanometer resolving power, allowing the ultrastructure of cells, organelles (Lamond and Earnshaw, 1998) and even individual proteins to be studied (Nathke et al., 1992, Heuser and Keen, 1988, Heuser and Kirchhausen, 1985).

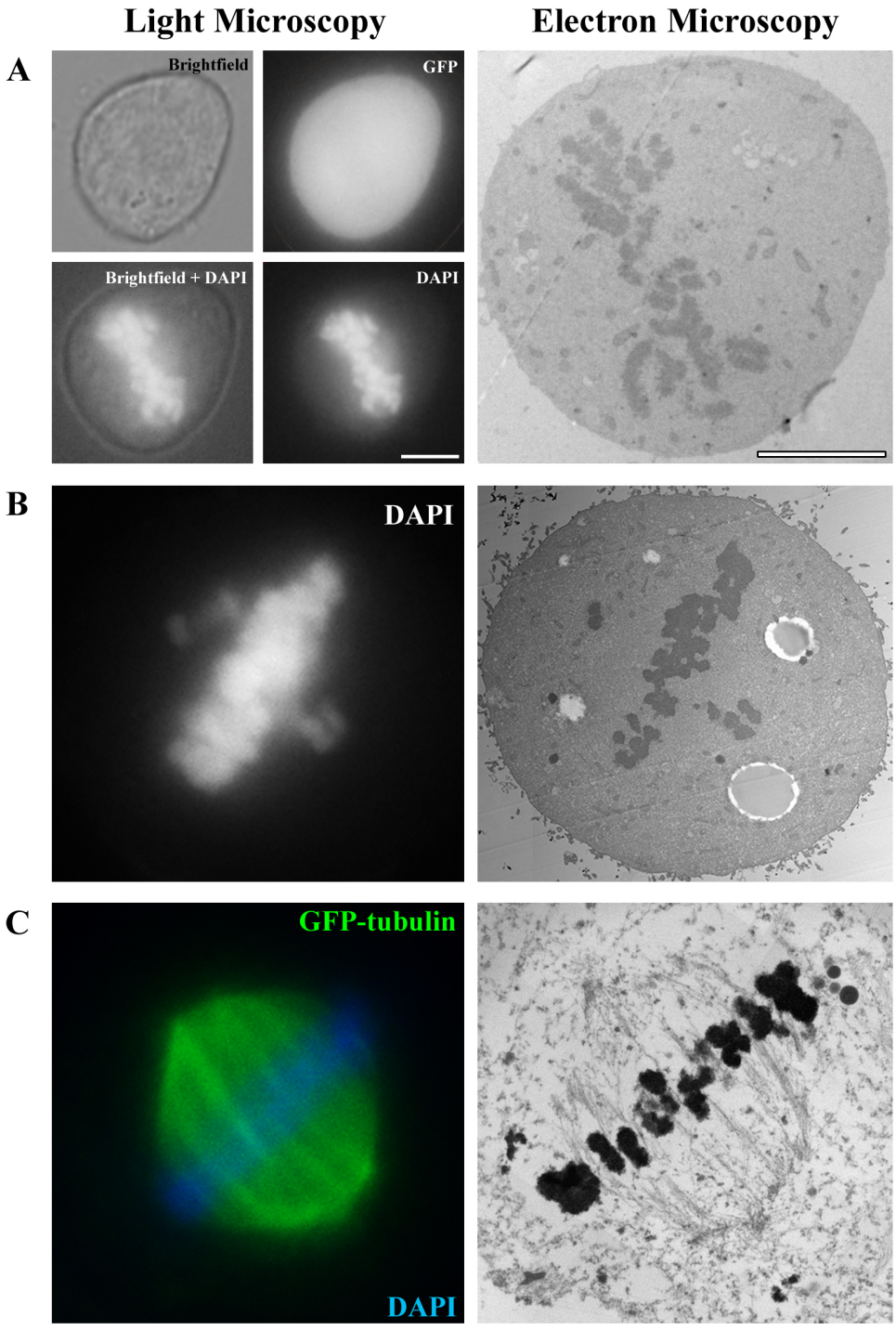

Figure 3.1 – Correlative Light Electron Microscopy (CLEM) – Examples of cells successfully processed using CLEM **(A - C)**. **(Left)** Light microscopy reference images for the re-identification of a cell of interest by TEM (**right**). The cells expressed GFP and were mitotic, as shown by the DAPI staining of condensed chromatin. CLEM can be used to monitor sub-cellular structures such as misaligned chromosomes (**B**) or microtubules (**C**). Scale bar, 5 μm.

The shortfalls of electron microscopy (other than the laborious nature of sample preparation) are that: 1) only static (i.e. dead) samples can be analysed. 2) EM alone does not allow for the specific following of individual cells of interest, such as cells expressing a fluorescent reporter or perhaps a particular cell type amongst a mixed population of cells. The limitations described can be overcome using CLEM, this allows both light and electron microscopy to complement each other to analyse a single sample. Using light microscopy it would be possible to assess whether a cell is at the appropriate stage in mitosis. This can be done by examining the morphology of the cell and by using a DNA stain to see the position of the chromosomes (**Figure 3.1 A & B**). In addition, if a reporter system is used that couples a fluorescent reporter (**Figure 3.1 A**) to shRNA expression, knockdown cells can be identified with certainty. This chapter sets out the methods required to correlate the LM images to the EM level in order to study the ultrastructure of the spindle. Examples of CLEM are shown in **Figure 3.1**.

Beyond the correlation of LM and EM, methods were required to study the ultrastructure of the spindle apparatus. It was necessary to consider which sectioning methods would yield the most useful images. Longitudinal sectioning is by far the most commonly used mode of sectioning for visualising cells by TEM, where sections are taken starting at the coverslip and progressively upwards through the cell (**Figure 3.2 A**), however, the analysis of mitotic cells also benefits from orthogonal sectioning (Mcdonald et al., 1992). For orthogonal analysis, sections are taken moving progressively through the spindle apparatus from one pole to the other (**Figure 3.2 A**).

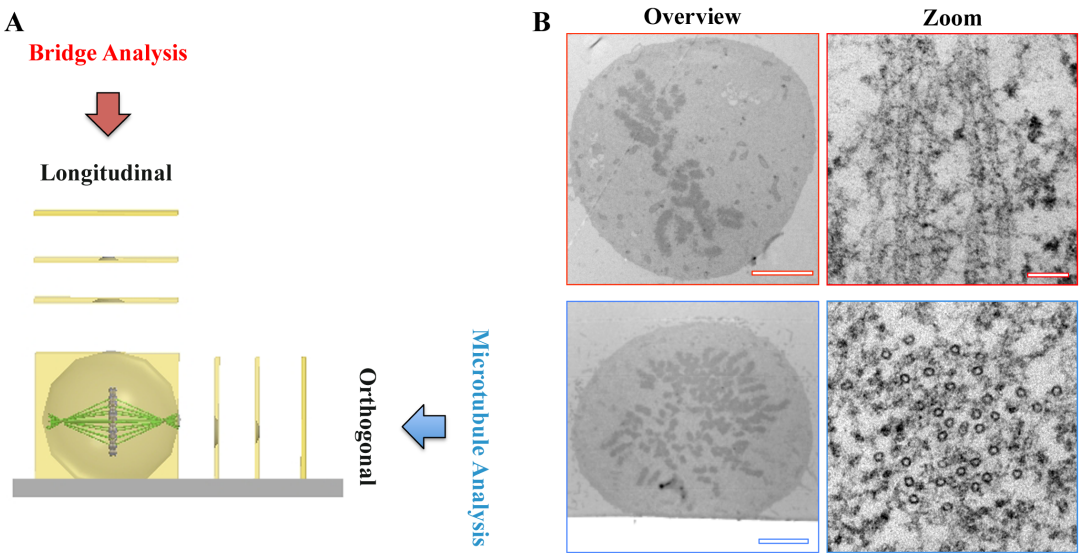

Figure 3.2 – Two axes for sectioning through the mitotic spindle – (**A**) A schematic diagram of sectioning axes. (**B**) Representative electron micrographs showing examples of mitotic cells sectioned along two different axes, and there usefulness. Longitudinal sectioning shows a neatly aligned metaphase plate and long stretches of MTs. Orthogonal sectioning revealed a cross-section through the metaphase disk and cross sections of kMTs. Scale bar: overview, 4 μm; zoom, 50 nm.

Used together both modes of sectioning are complementary. Longitudinal sections of the mitotic spindle contain large stretches of kMTs that often extend from the cell pole and terminate at an attachment on the kinetochore (**Figure 3.1 C**). Being able to visualise such large stretches of MTs increases the number of inter-MT bridges that can be counted (**Figure 3.2 B**). However, the composition of the K-fibre cannot be measured i.e. the number of kMTs per K-fibre cannot be quantified. It was proposed that an orthogonal analysis, taking cross-sections through the spindle, would allow whole K-fibers to be more easily mapped (**Figure 3.2 B**). The obvious limitation with this mode of sectioning is the poor frequency of bridge observations. In light of this, any spindle analysis approached would use longitudinal sectioning for inter-MT bridge analysis and orthogonal sectioning for kMT analysis.

3.2 Aims

This chapter will discuss the development of a series of EM based techniques designed to facilitate the ultrastructural analysis of mitotic, GFP-expressing cells. The primary aim of this chapter was to: 1) develop methods to allow the correlative analysis of mitotic, GFP-expressing cells. 2) preserve kMTs and inter-MT bridges, allowing these structures to be studied. 3) section a mitotic spindle along two different axes, enabling kMTs to be identified, followed, mapped and quantified. 4) observe and quantify inter-MT bridges.

3.3 Method

HeLa cells were transfected as described in **2.2.4** and were prepared for EM using the method described in **2.3.3.2**, unless otherwise stated.

3.4 Results and discussion

3.4.1 Correlative microscopy dishes and seeding density

The correlative microscopy carried out during this project required the use of specialised gridded dishes (MatTek), termed, CLEM dishes. These are 35 mm diameter, tissue culture-grade plastic dishes that contain a glass coverslip located on the base of the dish (**Figure 3.3 A**). The coverslip contains etched coordinates, that act as reference points for cells of interest, allowing the cell to be analysed using both LM and EM. Coordinates can be observed using brightfield LM and because the coordinates are raised from the glass, they leave an imprint on the bottom of polymerised resin. This allowed accurate re-locating of the area for sectioning and therefore correlative EM of the same cell. Coverslips are made from 0.19 – 0.23 μm thick, high-quality glass, this reduces the optical distance, allowing a better quality of image to be acquired. Glass-bottomed dishes were more desirable than the available alternative CLEM dishes, which are composed solely of plastic (Ibidi, Berlin, Germany). The plastic increases the optical distance and therefore reduces the imaging quality. In addition, the plastic dish adheres very tightly to the resin, making resin/dish separation extremely difficult. Most cell lines (HeLa, HEK293 and DT40) exhibited contrast using brightfield LM, resulting in a restricted visibility of coordinates, it was therefore important that cells were seeded into CLEM dishes at an appropriate density. **Figure 3.3 B** demonstrates the importance of seeding densities on coordinate visibility, where ~40,000 HeLa cells per dish was found to be optimal. Once the cells became too confluent this severely impaired coordinate visibility, making correlative microscopy very difficult (**Figure 3.3 B**).

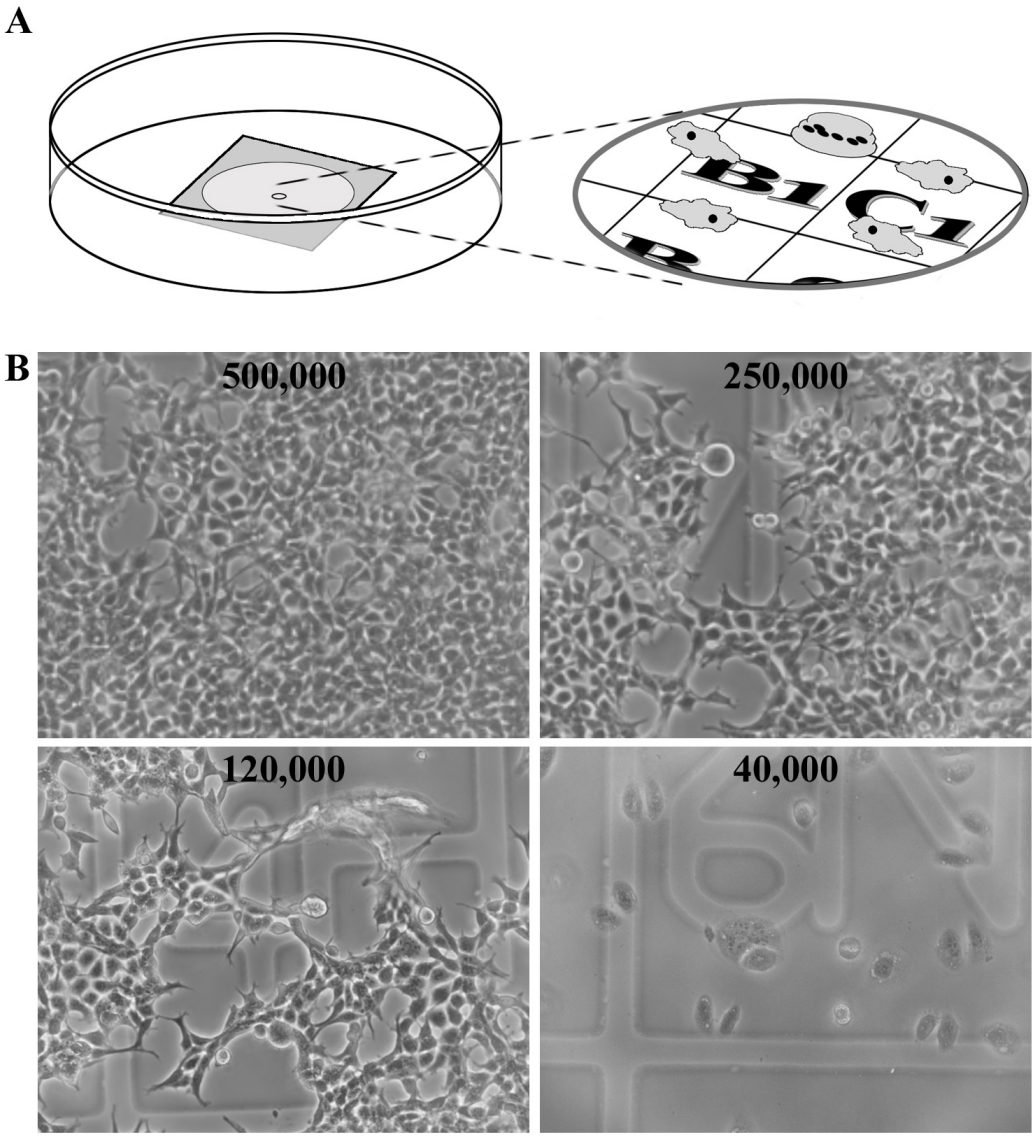

Figure 3.3 – Gridded dishes and optimal seeding densities for CLEM. (A) A schematic representation of a gridded dish used for correlative light electron microscopy (CLEM). The dish contains etched coordinates on the glass base. The 600 μm^2 coordinates boxes allow the re-identification of cells for electron microscopy. **(B)** Phase microscopy images show appropriate seeding density. Cell seeding density was titrated over four CLEM dishes. Typically ~40,000 cells was the most efficient, whereas greater densities often resulted in partially or fully masked coordinates and too few reduced the chances of finding a cell of interest. The number of cells seeded per dish is shown at the top of each pane. Scale, coordinate and box edges are 40 nm wide.

3.4.2 Optimising spindle preservation

Although most EM processing conditions have deviated little over the past 60 years, this project tested a number of fixation conditions to see if the fine-tuning of commonly-used fixation media could improve the preservation of the spindle apparatus. The osmolarity of fixative and wash solutions is an aspect of EM processing that has been well studied in the past (Hegelehartung et al., 1989, Mathieu et al., 1978, Bone and Ryan, 1972), however, during recent years emphasis on the importance of osmolarity has faded. The physiological osmolarity of mammalian tissue is ~290 mOsm, depending on species, tissue type and hydration status (Mathieu et al., 1978, Loqman et al., 2010). Fixative solutions should mimic physiological osmolarity, providing an iso-osmotic equilibrium between intracellular and extracellular fluids. The effect of fixative osmolarity on cell preservation was tested using three types of fixation solution during the EM processing (**2.3.3.2**) of three, otherwise identical, batches of HeLa cells.

An orthogonal analysis revealed that a fixation medium providing hyper-osmotic potential resulted in a significant amount of cell shrinkage (**Figure 3.4 Overview**), an occurrence also noted by other studies (Mathieu et al., 1978). In poorly preserved cells MTs could either not be identified, or, if they could be observed, they appeared infrequently and surrounded by an unusually compact, electron dense, cytoplasm (**Figure 3.4 Zoom)**. Although it was still possible, at least to some extent, to observe MTs, it was clear that these atypical cells had far inferior spindle preservation than was expected or required.

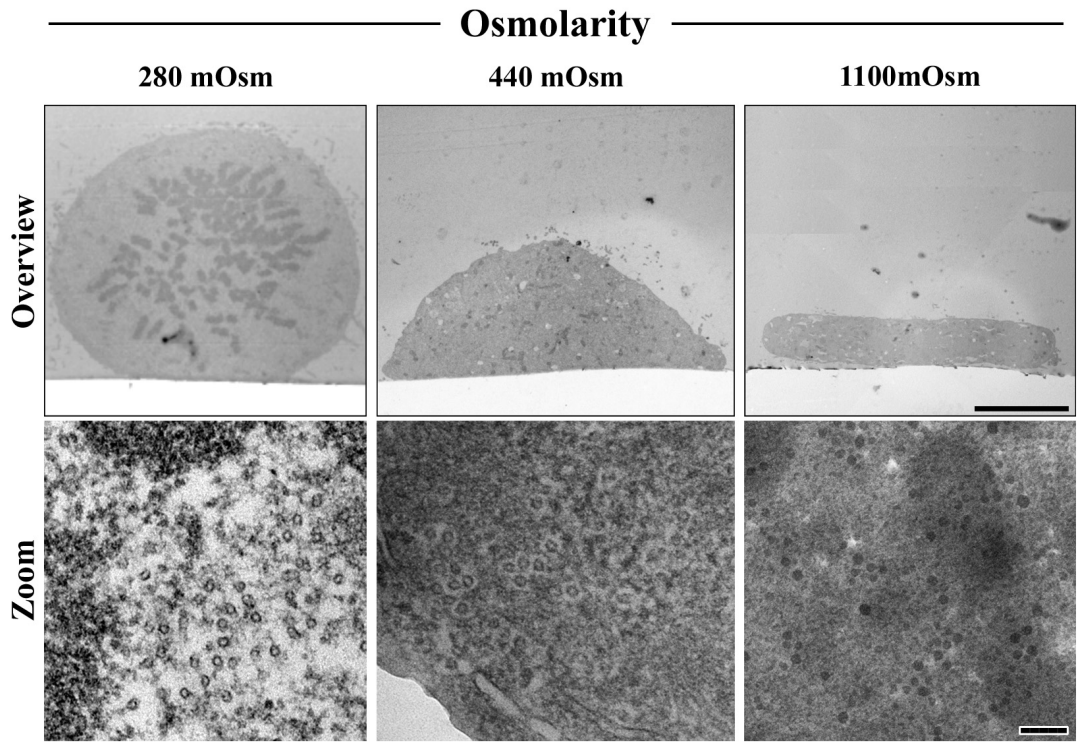

Figure 3.4 – Osmolarity of fixative solutions influences cell preservation. Representative electron micrographs of cells fixed in solutions with different osmolarities. Following fixation, the mitotic HeLa cells were sectioned orthogonally and screened for overall cell and spindle preservation. The top row shows an overview of whole cells. The bottom row shows high magnification images of spindle regions. The osmolarities of the fixation media were; 280, 440 and 1100 mOsm. Scale bars, 5 μm (top), 100 nm (bottom).

In contrast, a fixative solution that mimicked physiological osmolarity preserved mitotic cells far better (**Figure 3.4 Overview**), where traditional looking MTs were observed, exhibiting a good level of contrast (**Figure 3.4 Zoom**). In light of these results a fixative solution consisting of 2.5% glutaraldehyde, 0.5% PFA in 0.05 M PB was used throughout the rest of this study.

3.4.3 Preparation of CLEM samples for longitudinal sectioning

The purpose of establishing this method was so that mitotic, GFP expressing cells could be analysed through a longitudinal axis.

Following resin polymerisation a series of steps were necessary to achieve CLEM, these steps are shown in the pictorial guide of **Figure 3.5**. The primary objective was to separate the CLEM dish from the polymerised resin. Using pliers, the plastic edge of the dish was trimmed away leaving only the CLEM dish base remaining, still attached to the resin. With the edge removed it was possible to insert a razor between the dish and the resin. The glass coverslip possesses very little pliability, therefore, too much leverage by the razor generates too much force on one area of the dish and fractures the glass. Due to the differing thermal expansion temperatures of the resin and glass, immersing the sample into liquid nitrogen for 1-2 s improved the chances of separating the glass from the resin. Following separation, excess resin was removed using pliers, leaving only the gelatin capsule remaining. The coordinate containing the cell of interest was marked. A junior hacksaw and razor were used to remove unwanted resin. The marked perimeter helped minimise the risk of losing the cell. Following 'rough' trimming, a microtome was used to fine-trim the block.

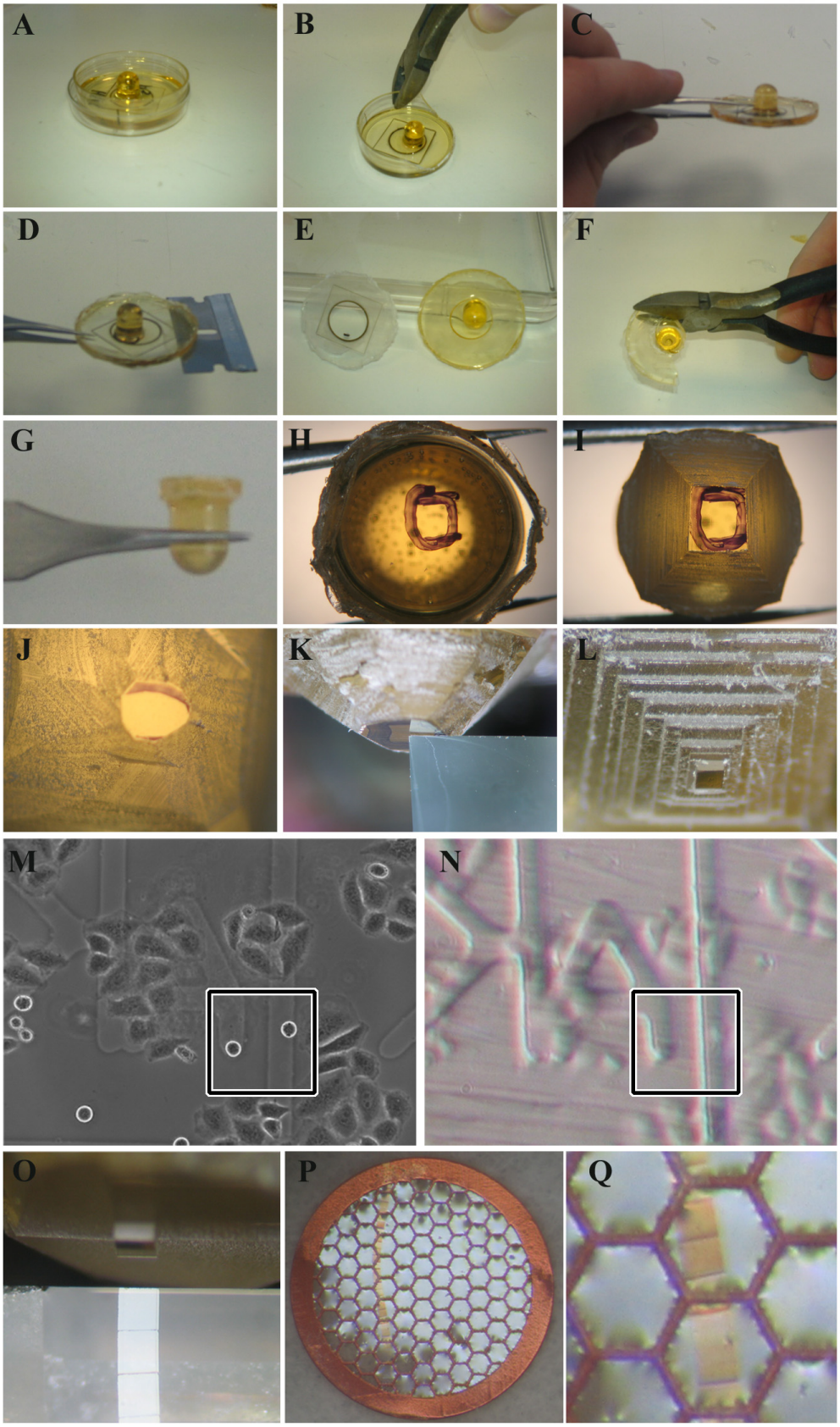
A
B
C
D
E
F
G
H
I
J
K
L
M
N
O
P
Q

Figure 3.5 – A pictorial guide to block preparation for longitudinal CLEM. Following polymerisation, resin was separated from the CLEM dish. Unwanted plastic was removed from the edges of the dish using pliers **(A-C)** allowing a razor to be inserted between the resin and the dish base **(D)**. Following the separation of resin and dish **(E)** excess resin was removed using pliers **(F)** until just the capsule remained **(G)**. The cell of interest was marked **(H)** with the aid of LM images **(M)** and resin coordinates **(N)**. Unwanted resin was removed using a junior hacksaw **(I)** and a razor **(J)**. Resin was trimmed using a microtome and a glass knife **(K)** until a neat block was generated at the top of a pyramid **(L)**. Blocks were sectioned using a diamond knife **(O)** and ribbons collected using 100 mesh copper grids **(P & Q)**, coated with formvar.

At this point, correlative LM reference images were used to sculpt a precise block, using a glass knife, around the cell of interest. This was possible as cells from the reference pictures could still be seen once embedded in resin. Following fine shaping of the block, ultrathin sections were taken using a diamond knife and collected on formvar-coated copper grids.

The size of the block face should be kept as small as possible, this allows for a greater number of consecutive sections to be captured per grid. The example in **Figure 3.5 P & Q** contains ~30 sections, equating to ~2.4 consecutive μm of cell that could be analysed Sections were post stained (**2.3.3.2**) and were ready for imaging by TEM.

3.4.4 Preparation of samples for orthogonal sectioning

The purpose of establishing a protocol for orthogonal sectioning was so that cross-sections of K-fibres from mitotic, GFP-expressing cells could be analysed. **Figure 3.6** provides a step-by-step pictorial guide to this mode of block preparation. To section a cell orthogonally, through the mitotic spindle, a more complicated method of sample preparation is necessary. At the resin-embedding stage of EM processing the addition of a gelatin capsule containing resin (essential for longitudinal sectioning), was no longer necessary, leaving a CLEM dish covered with a flat layer of polymerised resin. The plastic edge of the dish was removed using pliers, allowing a razor to be inserted between the dish base and the resin to carefully separate the two. At this stage, LM reference images were used (**Figure 3.6 E-G**), not only to relocate the cell of interest, but also to determine the correct orientation for a cross-sectional analysis of the spindle. LM images revealing the position of the metaphase plate were the most helpful. The cell of interest was

marked on the resin, the block was then rotated so that the metaphase plate was at 90° to the sectioning axis (**Figure 3.6 H & I**). A rectangle was marked onto the resin in this desired orientation before excision using a junior hacksaw and a hand built mitre block. The excised resin block was inserted directly into a microtome chuck, meaning no re-embedding in resin was necessary. A fine block was sculpted using a glass knife, before serial sections were taken through the cell of interest. Image **Q** is a mock representation of the resin block, using the LM image (**G**) to demonstrate how the resin was re-oriented and trimmed. Image **R** is the actual resin block containing the cell of interest that has been sectioned orthogonally half way through the mitotic spindle. Sections were collected on copper grids, similarly to longitudinal sections.

3.4.5 Characterising K-fibres

Although orthogonal analysis is best suited for observing MT organisation, an important question was now addressing, how kMTs can be discriminated from other populations of MTs, such as ipMTs and aMTs. This was tested by serial sectioning a mitotic HeLa cell **(Figure 3.7)**. A pole-to-pole orthogonal analysis revealed that, upon reaching the metaphase disk, it was possible to choose a chromosome and follow it through consecutive sections until the kinetochore/K-fibre boundary was breached (**Figure 3.7 – left to right**). A maintained orthogonal progression from this position revealed the adjoining K-fibre and associated kMTs (**Figure 3.7, far right**). Being able to recognise and identify kMT termination at the kinetochore satisfies the criteria for differentiating between kMTs of a K-fibre and all other populations of MTs.

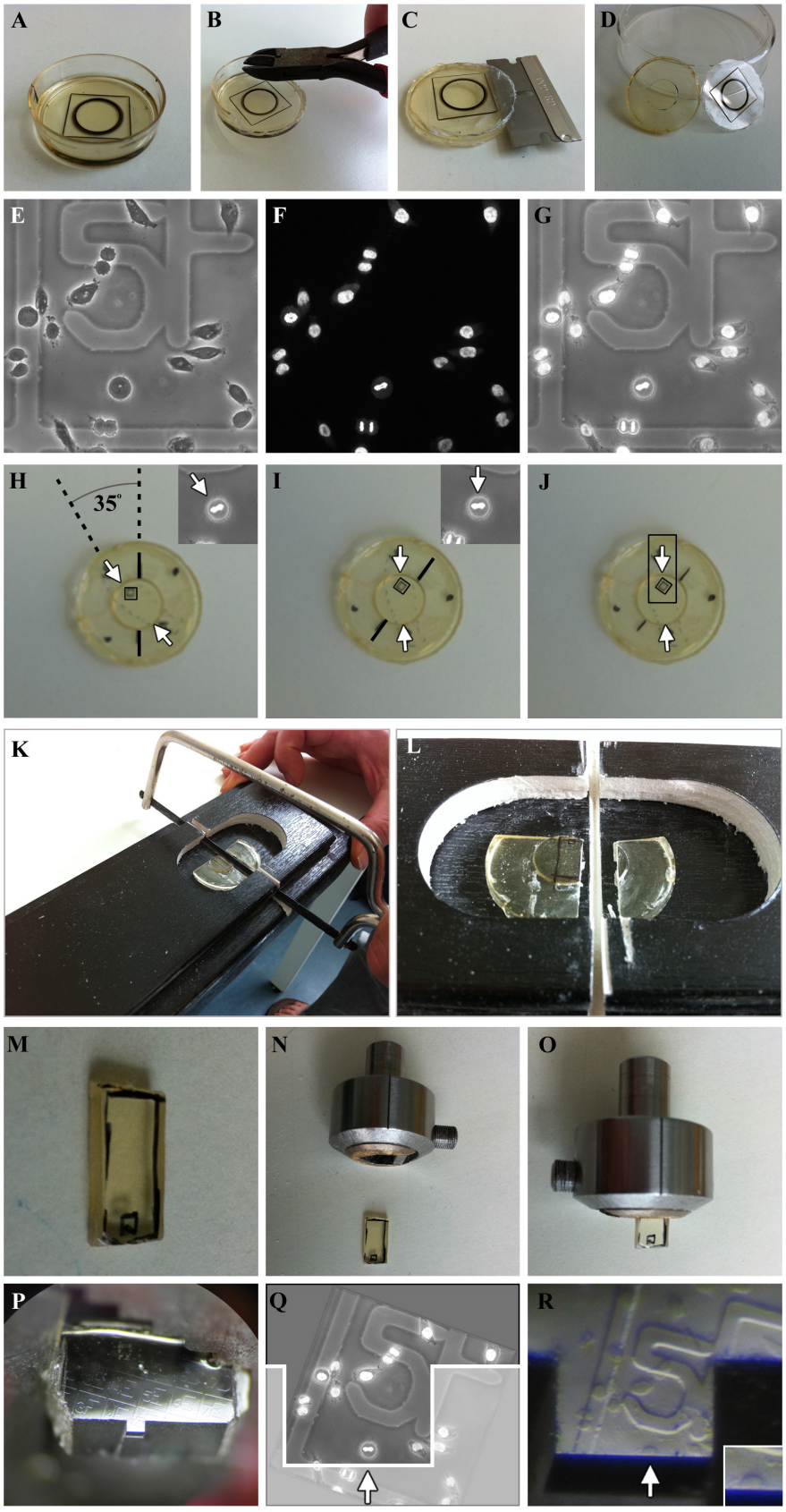
A
B
C
D
E
F
G
H
35°
I
J
K
L
M
N
O
P
Q
R

Figure 3.6 – A pictorial guide to block preparation for orthogonal CLEM. Following polymerisation, resin was separated from the CLEM dish. Unwanted plastic was removed from the edges of the CLEM dish using pliers (**B**) allowing a razor to be inserted between the resin and the dish base (**C**). Following separation (**D**) the position of the spindle was estimated using the reference LM images (**E-G**). These images allowed the re-orientation of the resin (**H & I**) so that an appropriate block could be marked (**J**) before excision using a junior hacksaw and a mitre block (**K & L**). The excised block (**M**) was inserted into a microtome chuck (**N & O**) and fine trimmed using a glass knife (**P**) before serial sections were taken of the cell, in the desired orientation (**Q & R**).

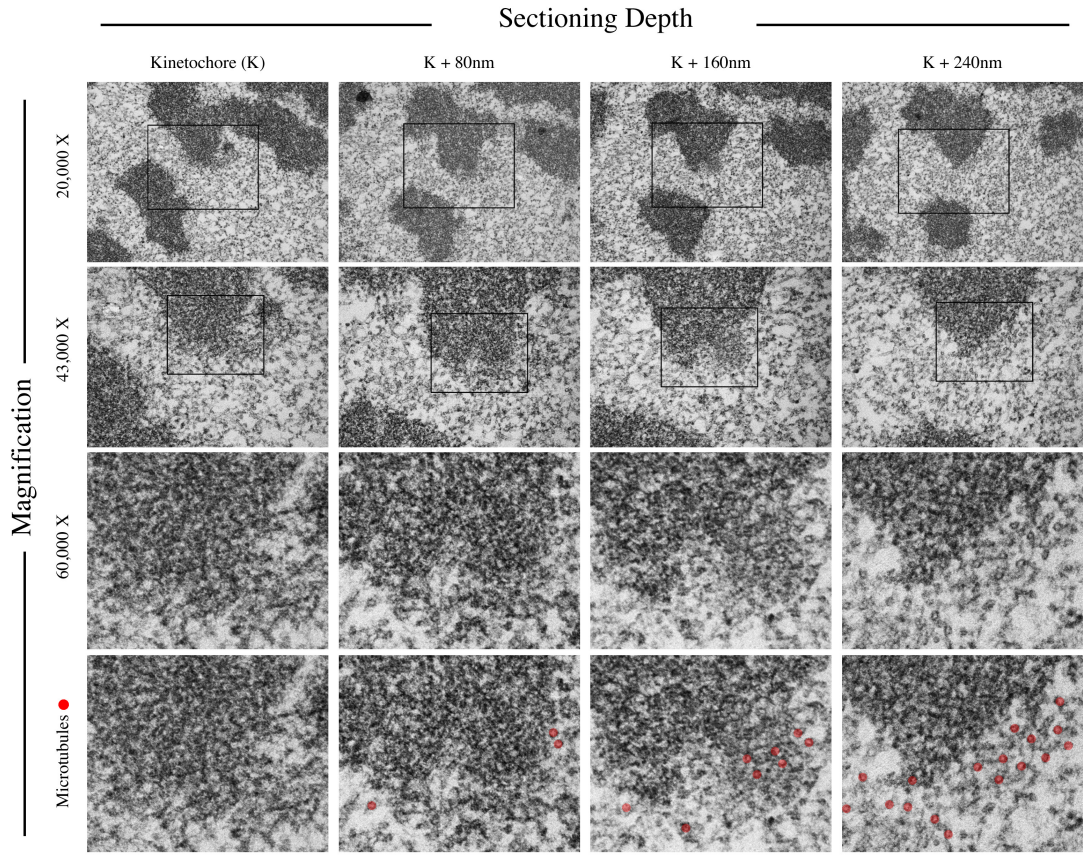

Figure 3.7 – Serial sections discriminate kMTs from other MT populations. A panel of electron micrographs of a K-fibre, followed through consecutive serial sections. The imaging started at the kinetochore (left column) and progressed through the kinetochore and into the origin of its adjoined K-fibre (right column). Micrographs from top to bottom show increasing magnifications. Higher magnifications allow the kMTs to be mapped (red dots, bottom panels).

Recognising K-fibres using this method would provide a high level of confidence, but it would not always be practical due to the laborious nature of the technique, especially considering the number of K-fibres needing to be analysed.

The number of kMTs per K-fibre in mammalian cells is 20-40 (Rieder, 1982). Although ipMTs exhibit some degree of bundling, during metaphase any ipMT bundles within close proximity to the metaphase disk do not exceed six ipMTs per fibre (Mastronarde et al., 1993). This project took advantage of this by limiting a kMT analysis to bundles only containing more than eight MTs and restricted the study to areas only in close proximity to K-fibre termination points. By establishing these criteria our analysis was sufficiently robust to have minimal contamination by other MT populations.

3.4.6 Is 2D imaging sufficient for a kMT analysis?

After the criterion had been established to differentiate between kMTs and other MT populations, a new issue was raised. Due to the structure of the mitotic spindle, K-fibres extend from a single origin at the cell poles and extend outwards until they terminate at the kinetochore (Mcdonald et al., 1992, Rieder, 2005). In order to create this structure a certain degree of MT curvature is needed**.** Acquiring only single-angle images, regularly resulted in only a few of the total kMTs being revealed, this can be seen in any one of the images in **Figure 3.8**. It became apparent that using orthogonal sections to analyse K-fibres would require more than standard 2D imaging and that it was likely a more complex method for mapping MTs was necessary.

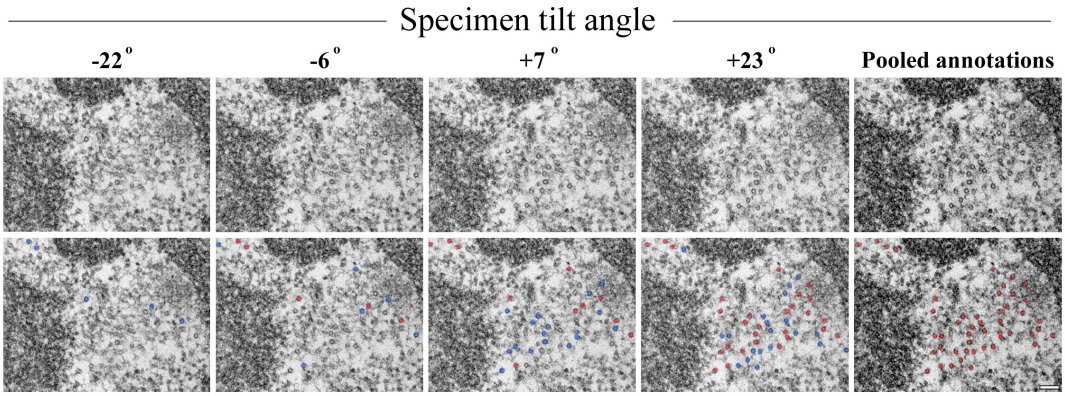

Figure 3.8 – A tilt series improves kMT coverage – Electron micrographs taken from a -45° to +45° tilt series of a K-fibre. A selection of frames, taken at various tilt increments, are shown. Observable MTs are marked with dots (bottom row). Blue dots represent MTs that are unique to that tilt frame. Red dots represent the accumulating MTs identified in previous tilt frames. The total number of MT annotations were pooled together onto one frame (far right) giving a fair overview of the whole K-fibre.

It was found that, by tilting the specimen and capturing images of the sample throughout a range of tilt increments (**Figure 3.8 – left to right)** it was possible to identify a majority of the kMTs comprising the total K-fibre. These MTs could be annotated and pooled onto one single frame (**Figure 3.8 - far right**).

3.4.7 A single tilt analysis is sufficient for a kMT study

Following the development of a kMT quantification protocol it was important to consider whether carrying out a single tilt analysis would be an efficient enough method for kMT analysis. This study had already uncovered that a tilt series revealed a far greater number of MTs in a K-fibre bundle than routine no-tilt imaging. Was it possible that a dual-tilt series could reveal an even greater number of kMTs? To test this, a dual tilt analysis was carried out on a K-fibre (**Figure 3.9**).

A single tilt would rotate only around the X-axis, a dual tilt however can rotate around both the X and Y axes. This usually requires a specialised specimen holder for the microscope, which, unfortunately we did not have access to. Instead, for this experiment, an X-axis tilt series was taken, the specimen arm was retracted from the TEM and the grid rotated manually 90° about its Z-axis and re-inserted. A second X-axis tilt series of the same K-fibre would now effectively act as a Y-tilt.

It was found that, regardless of the tilt axis chosen, almost 80% of the total kMTs within a K-fibre could be revealed (**Figure 3.9 A & B**). The X-axis tilt identified 78% and the Y tilt 77% of the total kMTs potentially observable, with 55% appearing common between the tilts (**Figure 3.9 B)**.

Although the dual tilt did reveal ~20% more MTs overall, even at this stage it was apparent that should this format of analysis be necessary for every K-fibre analysed, it would be laborious and impractical, predominantly for two reasons:

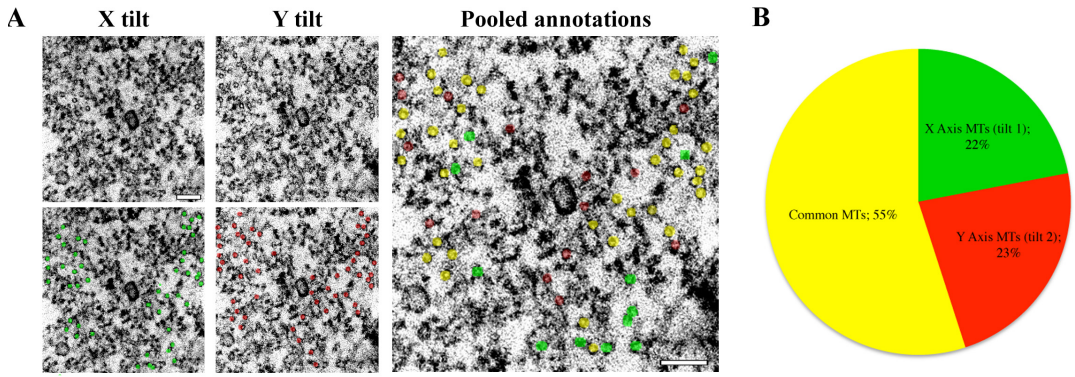

Figure 3.9 – Single tilt series offer high coverage of kMTs - A dual tilt series of one K-fibre was carried out. (**A**) Representative electron micrographs taken from the central region of both X and Y tilts (**A-top**). All MTs observed in each tilt series were annotated (**A-bottom**). The sum of MTs from both tilts were pooled together on to a single frame taken from the Y axis tilt series, any MTs that were common to both tilts were marked yellow. Scale bar, 100 nm. (**B**) A pie chart showing the percentage of total MTs that were unique to each tilt and also the common ones.

1) Re-identifying the same section, cell and K-fibre, once manually rotated, was a difficult task. 2) A single tilt series can take anywhere between 10 – 30 min to complete, so the addition of a second tilt would extend this already lengthy analysis. It was decided that single-tilt analysis, yielding 80% of the MTs would be sufficient for this study.

Although a protocol for viewing kMTs was now established, a system for data quantification still needed to be designed. This study was able to develop a variety of ways to extract and quantify data from the tilt series videos, allowing kMT frequency, K-fibre cross sectional area and inter-MT distances to be measured.

3.4.7.1 Counting/quantifying kMTs

The output file of a tilt series is a *.mrc file, this file format for electron density has become industry standard in electron microscopy where the result of the technique is a three-dimensional grid of voxels (volumetric pixels) each with a value corresponding to density of electrons. Unless a tilt video was to be used for a part of a representative figure, analysis of a *.avi file (compressed *.mrc file) was sufficient. In order to quantify kMT numbers the *.avi file had to be imported into ImageJ where the 'stack sorter' plug-in allowed the video to be viewed as a series of stills. The MTs were mapped in each image of the tilt series and pooled together onto one frame (**Figure 3.10 A**), allowing total MT frequency to be quantified. To ensure that each kMT was only annotated once, only MTs unique to each tilt image were annotated.

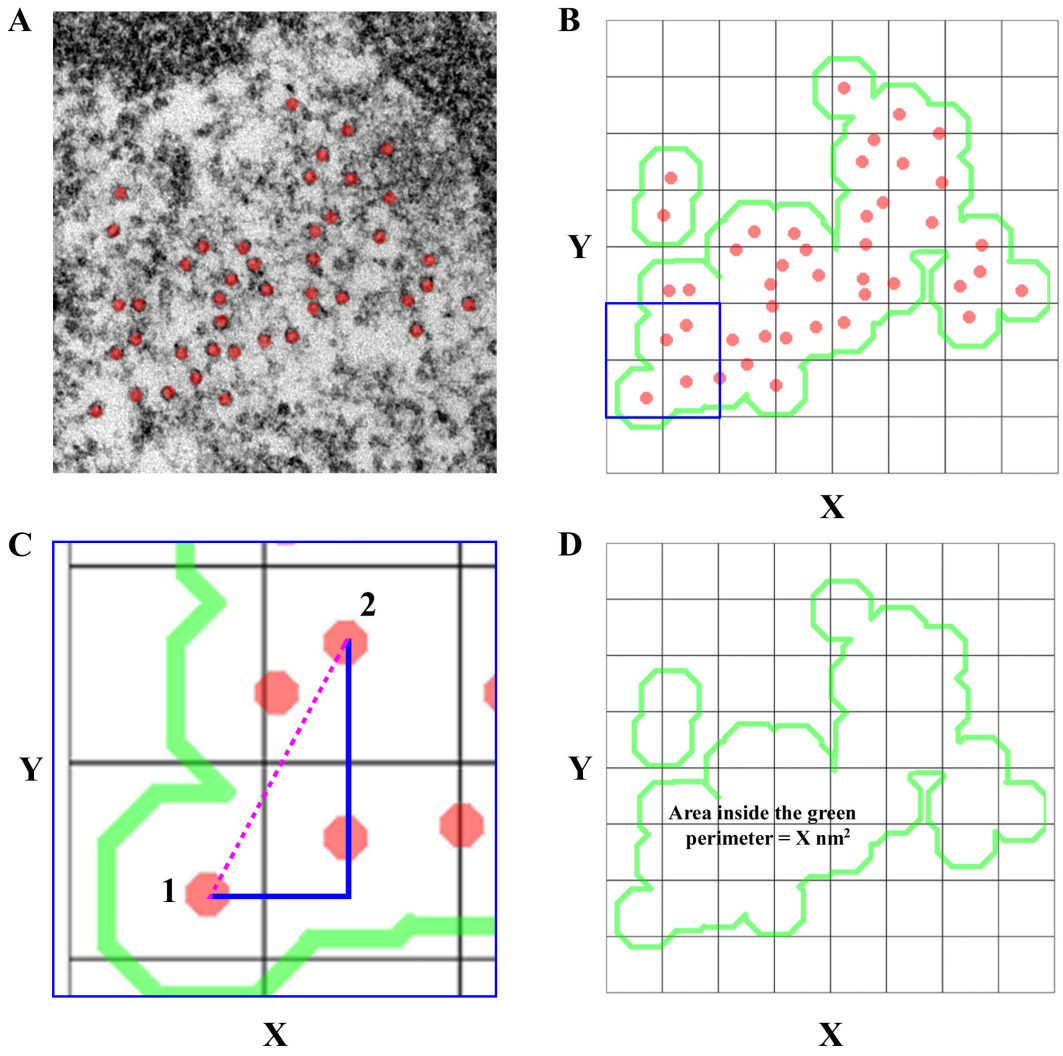

Figure 3.10 – Methods for quantifying kMT number, inter-MT spacing and cross-sectional area. (**A**) An example of a fully annotated K-fibre bundle. (**B**) The MTs in **A** were traced onto a new layer in Photoshop Elements, allowing the MTs to be easily counted. A synthetic perimeter was created by 'expanding' outwards from the most peripheral MTs of the K-fibre, the 'stroke' tool added the green border. (**C**) Zoomed of area shown in B. Inter-MT distances could be calculated using Pythagoras theorem. (**D**) Using ImageJ the cross-sectional area of the K-fibre was estimated by measuring the area inside of the green perimeter.

3.4.7.2 Inter-MT distances

Using the image of mapped MTs (**Figure 3.10 A**) it was possible to analyse changes in inter-MT spacing. In order to quantify this, the *.jpg created in PSe of mapped MTs (**Figure 3.10 B)** was imported into ImageJ, here it was possible to dock the MTs onto a background matrix of coordinates. The reference positions of the MTs were tabled and copied into a specifically designed Excel spreadsheet. This allowed the Euclidean distance between all MTs and every other MT within the K-fibre to be calculated automatically (**Figure 3.10 C**). A typical K-fibre analysis would yield a spreadsheet containing ~1000 individual measurements per tilt series. At this stage it was not possible to determine which distances would be the most important, however the spreadsheets were designed robust enough for any particular statistic to be extracted, as an example, Excel's 'MIN' function could isolate the distances between any MTs and their nearest neighbouring MTs, a group of figures carrying potential interest.

3.4.7.3 K-fibre cross sectional area

In order to estimate K-fibre cross sectional area a *.jpg of a tilt image containing the pooled MT annotations (**Figure 3.10 A**) had to be imported into Adobe Photoshop Elements (PSe), here the MTs were traced onto a new layer, resulting in a sheet of painted dots on a transparent background, this was saved as a *.jpg. It was found that using PSe, it was possible to highlight all the annotations and generate a synthetic prediction of the K-fibre perimeter (**Figure 3.10 D**). This perimeter was created using the "grow" function to expand 20 pixels outwards from the most peripheral MTs of the fibre, followed by the "stroke" tool to craft a green border around the predicted edge of the K-fibre (the stroke was made onto a new

layer). The green perimeter was then imported back into ImageJ where the internal area could be calculated using a standard "measurement" tool (**Figure 3.10 D**). The 20 pixel 'grow' was a predetermined size, as this was the largest inter-MT bridge identified in the longitudinal study (discussed in Chapter 4). The use of a synthetic perimeter minimises potential bias deciding if MTs are or are not part of a K-fibre.

3.4.8 Establishing inter-MT bridge analysis

Following the development of a strategy for analysis of MT number and K-fibre cross-sectional area, an analytical strategy for bridge frequency and length needed to be created. This study had already uncovered that longitudinal sectioning would be the most appropriate for analysis of inter-MT bridges (**Figure 3.2**), due to the greater number of bridges observable using this mode of sectioning. In order for the bridge analysis to remain as fair and unbiased as possible a number of criteria had to be met before the analysis of any images was permitted, these are discussed below.

3.4.8.1 Maintaining a consistent sectioning depth

To ensure that a similar region of the spindle would be studied in the cells used during the longitudinal analysis, the sectioning depth was kept as constant as possible, i.e. only sections taken between a depth of ~6-8 μm were retained for analysis. This depth typically contains the central region of the spindle and, if possible, only a spindle region where a centriole was visible were considered. By restricting the spindle depth analysed, this should limit any variability in K-fibre numbers seen at different depths of the spindle apparatus.

3.4.8.2 Analysed spindle regions were chosen at random

At low magnifications (~4,800 x), chromosomes aligned at the metaphase plate can be observed, but kMTs can not be resolved (**Figure 3.11 A**). To rule out any bias related to MT density, random regions of the spindle were chosen for analysis at low magnifications (**Figure 3.11 A**). High magnification MIAs (**Figure 3.11 B**) were taken of the randomly selected area in **Figure 3.11 A**. A 4 x 4 MIA at 60,000 x covers >15% of a spindle region (**Figure 3.11 A**), therefore where possible, taking a 4 x 4 MIA of each side of the metaphase plate was sufficient as a representative examination of the section.

3.4.8.3 Extracting data from MIAs

Figure 3.11 B illustrates the parameters that were measured: 1) Total MT length. 2) Paired MT lengths (any MTs within 80 nm from one another). 3) Bridge numbers. 4) Bridge lengths. The guidelines for bridge identification were defined using established criteria (Hepler et al., 1970): A 2-5 nm thick, electron dense structure, that cross-links two adjacent MTs.

To allow bridge counts to be comparable between cells and treatments it was necessary to express bridge frequency as a proportion of MT length. The measuring of paired MTs consisted of any MTs within 80 nm of bridging distance of one another (**Figure 3.11 B & C**). The rationale for measuring this variable was to try and account for any potential MT loss, incurred by depletion of clathrin and other proteins of interest. Although this measurement makes the analysis more stringent, it should be noted that in measuring the length of paired MTs the incidence of one MT being measured twice, as part of two separate paired regions, could occur.

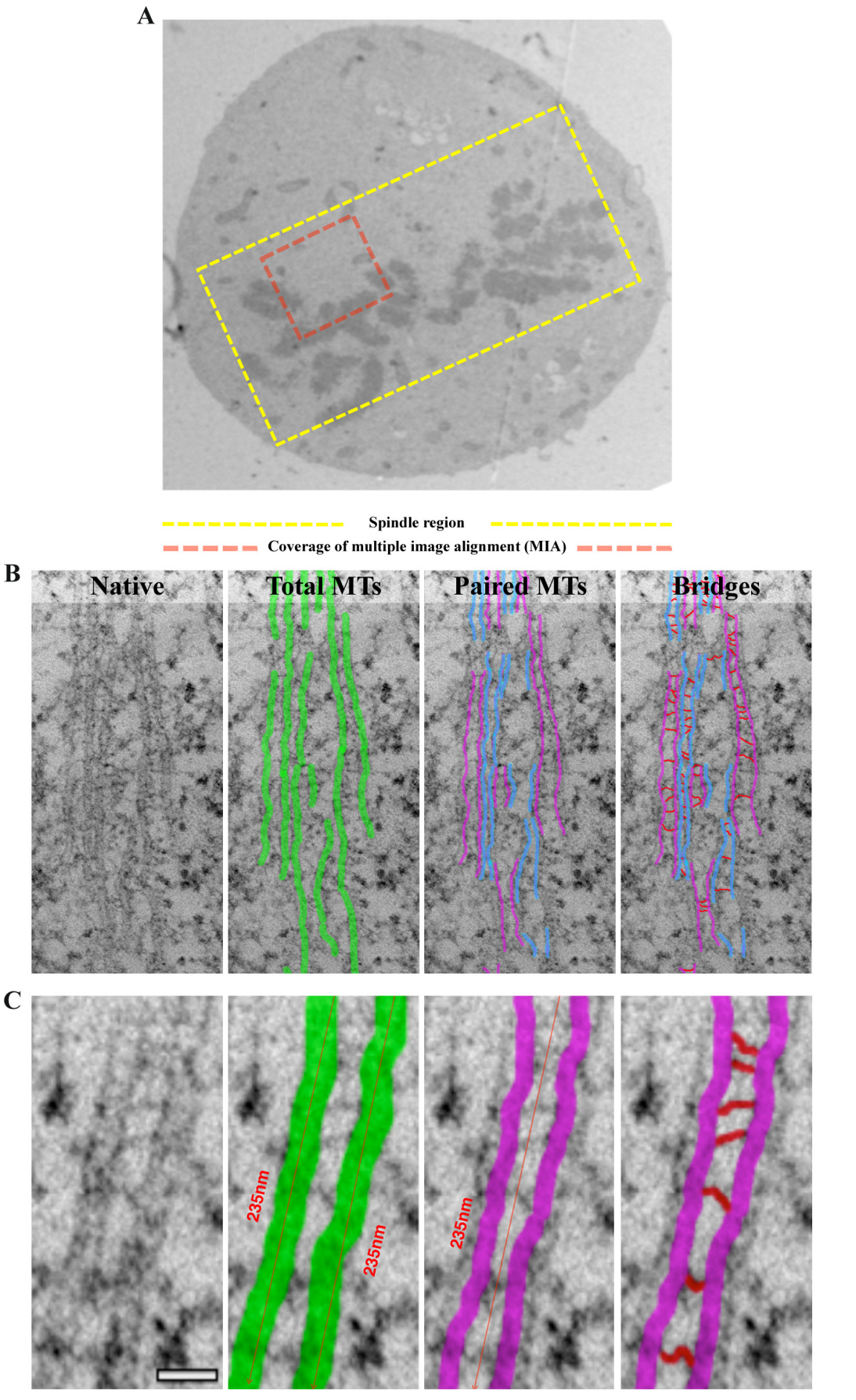
A
Spindle region
Coverage of multiple image alignment (MIA)
B
Native
Total MTs
Paired MTs
Bridges
C
235nm
235nm
235nm

Figure 3.11 – Quantification methods for longitudinal bridge analysis – Electron micrographs demonstrating how inter-MT bridges were quantified during this study. At low magnification a random area of the spindle (yellow) was chosen for a high magnification MIA to be taken (**A)**. Any K-fibres observed in the MIA (red) were subjected to kMT analysis. (**B**) A representative K-fibre (native) displaying all of the parameters measured, such as; total MT length (green), paired MT regions (pink/blue) and inter-MT bridge frequency & length (red). (**C**) Zoomed examples of the measurements described in **B**. Paired MT regions were defined as two MTs within 80 nm bridging distance of one another. Note that one MT can be part of two separate MT pairs (pink and blue). Scale bar, 40 nm.

3.5 Conclusion

To test the hypotheses of this project it was necessary to carry out an ultrastructural analysis on mitotic cells, depleted of proteins of interest. This chapter has established a methodology allowing the correlative microscopic analysis of GFP expressing, mitotic cells. This allows the use of the pBrain series of vector (**Figure 2.1 A**) for the RNAi of target proteins. The preservation of these cells has been improved by optimising the fixation conditions, accounting for the effects of osmolarity, a major contributor of cell shrinkage. Since this study is interested in the spindle apparatus, a protocol for sectioning along orthogonal and longitudinal axes has been established, providing the opportunity to analyse the spindle in the most appropriate orientation, for the particular structure of interest. In addition, this chapter has also created a series of methods allowing K-fibres to be analysed for changes in MT organisation and inter-MT bridge loss/alteration.

4 Chapter 4 – A TACC3/ch-TOG/Clathrin complex stabilises kinetochore fibres through inter-MT bridging

4.1 Introduction

Inter-MT bridges have been observed in K-fibres, where they are thought to promote kMT organisation and stability (Hepler et al., 1970, Rieder, 1982, Witt et al., 1981, Mcdonald et al., 1992). Despite being first reported over 40 years ago, their identity has remained elusive. To gain a better understanding of the function of these bridges their identity needs to be uncovered. A short list of potential candidates has been proposed, with clathrin being the most suitable. Clathrin at the spindle was recently shown to be in complex with TACC3 and ch-TOG (Booth et al., 2011, Fu et al., 2010, Hubner et al., 2010, Lin et al., 2010). These proteins are known to be involved with K-fibre stability (Fu et al., 2010, Gergely et al., 2003, Kinoshita et al., 2005, Royle et al., 2005). Based on several lines of evidence (reviewed in Chapter 1) it has been suggested that clathrin, in complex with TACC3 and ch-TOG, uses its unique triskelion structure to promote K-fibre stability and organisation through the physical cross-bridging of kMTs. There is currently no direct evidence to support this hypothesis. If the clathrin complex is indeed a physical cross-linker of kMTs, then depletion of any of the complex members should induce an ultrastructural phenotype.

4.2 Chapter aims

The aim of this chapter was to carry out an ultrastructural study, analysing the phenotype of clathrin, TACC3 and ch-TOG depletion in mitotic cells. Using the methods developed in Chapter 3 a number of structures were analysed following RNAi, including:

- The organisation of kMTs in K-fibres
- Inter-MT bridge frequency and distribution
- Gold particles following immunogold labelling of clathrin

4.3 Materials and methods

4.3.1 Generation of pBrain vectors to express GFP and shRNA

Using tested RNAi sequences (**Figure 7.1**) (Gergely et al., 2003), oligonucleotides were designed for the shRNA component of the pBrain vector system, targeting TACC3 or ch-TOG (**Figure 7.1**). The pBrain-GFP-shRNA construct targeting clathrin was already generated and available for use (Royle et al., 2005).

4.3.1.1 Generation of pBrain-SpH-shRNA

Oligonucleotides were resuspended in nuclease free H_2O to 3 μg/μl before being annealed into a double stranded DNA cassette. To anneal, 2 μl of oligonucleotides were added to 48 μl annealing buffer (100 mM NaCl, 50 mM HEPES pH 7.4) and heated: 90°C, 4 min; 70°C, 10 min; slowly cooled to 10°C. The DNA cassette was phosphorylated to improve ligation efficiency into the dephosphorylated vector, using the following oligonucleotide mix: annealed oligo

mix, 2 µl; T4 PNK buffer, 1 µl; 10 mM ATP, 1 µl; T4 PNK, 1 µl and ddH_2O, 5 µl. This was heated for 30mins at 37°C. Oligonucleotides were now prepared for ligation into pBrain-SpH vector. The pBrain-SpH vector was prepared by restriction endonuclease digestion in a 50 µl reaction using *Bgl*II and *Hin*dIII (**2.1.6**). The DNA cassette was ligated into pBrain-SpH (**2.1.7**) and amplified via bacterial transformation (**2.1.8**) before DNA recovery using a miniprep (**2.1.9**).

4.3.1.2 Generation of pBrain-GFP-shRNA

To generate pBrain-GFP-shRNA constructs a DNA cassette containing shRNA and H1 promoter sequences was restriction-enzyme digested out of pBrain-SpH-shRNA using *Apa*LI and *Nhe*I (**2.1.6**), an eGFP-C1 vector was digested in parallel, using the same enzymes. Following agarose gel purification (**2.1.4 & 2.1.5**) the DNA cassette was ligated into the eGFP-C1 vector (**2.1.7**) before transformation (**2.1.8**) and DNA recovery using a midiprep (**2.1.9**). This construct was now referred to as pBrain-GFP-shRNA.

4.3.2 Immunofluorescence microscopy

HeLa and PtK1 cells were fixed for immunofluorescence (**2.3.2.2**) and labelled with anti-CHC (X22), anti-β-tubulin or anti-TACC3 primary antibodies, all at a concentration of 1 in 1000 (in blocking solution). For ch-TOG labelling, HeLa cells were fixed in methanol for 15 min at -20°C, anti-ch-TOG was used at 1 in 2000 concentration. The appropriate fluorescently labelled secondary antibodies were used to detect mouse (clathrin and TACC3) or rabbit (ch-TOG) primary antibodies. Cells were mounted as described in **2.3.2.1**.

4.3.2.1 Testing RNAi efficiency of pBrain constructs using immunofluorescence microscopy

HeLa cells were transfected with a pBrain vector expressing shRNA that targeted clathrin, TACC3, ch-TOG or control shRNA and left to express for 5 days (clathrin & control) or 3 days (TACC3 and ch-TOG). Cells were fixed and labelled with the appropriate antibodies (**4.3.2**). Knockdown efficiency of pBrain-GFP-CHC was measured by comparing the total cell fluorescence of clathrin in control cells with that of knockdown cells. Knockdown efficiency of pBrain-GFP-TACC3 or ch-TOG was measured by comparing the spindle fluorescence of TACC3 or ch-TOG in control cells with those from knockdown cells. Total cell and spindle fluorescence was measured using ImageJ.

4.3.3 Correlative light electron microscopy (CLEM)

EM processing and preparation for CLEM was carried out as described in **2.3.3** and throughout **Chapter 3**. Immunogold labelling was carried out as described in **2.3.3.3**.

4.3.3.1 Quantification of CCVs at the spindle

HeLa cells were sectioned orthogonally, through and past the metaphase disk. At a depth of ~1.0 μm past the last chromosome (**Figure 4.2 A**), 4 X 4 MIAs were acquired and the number CCVs quantified. The cell was divided into three sections (**Figure 4.2 B**): spindle region (green), non-spindle region (red) and a 'void' region (yellow). CCVs (purple) and clathrin-coated pits (blue) were counted and annotated in the green and red zones. The yellow section acted as a buffer zone in-between the two to avoid any overlap. It was possible to discriminate between CCVs (black arrow) and non-CCVs (white arrow) vesicles and pits (**Figure 4.2 C**).

4.4 Results

4.4.1 Clathrin localises to the spindle during mitosis

Clathrin localises to spindle apparatus during mitosis (Okamoto et al., 2000, Royle et al., 2005), an observation that this study was able to reproduce in PtK1 cells (**Figure 4.1**). In metaphase and anaphase, clathrin co-localised with tubulin on the spindle. Clathrin did not appear to co-localise with astral microtubules (aMTs) or interphase MTs. Clathrin is known to localise on K-fibres (Royle et al., 2005), however the possibility that it is also found on inter ipMTs cannot be ruled out.

4.4.2 Clathrin at the spindle is not assembled in CCVs

Is it possible that clathrin, localising at the spindle during mitosis, could just be CCVs concentrating within the spindle? CCVs are known to interact with interphase microtubules (Gruenberg et al., 1989, Bananis et al., 2004, Imhof et al., 1983) and also microtubules during cytokinesis (Robbins and Jentzsch, 1969). As reviewed in **Chapter 1** it is very unlikely that clathrin at the spindle represents an accumulation of CCVs, for example key adaptors such as AP-1, 2, 3 and 4 do not localise at the spindle (Royle et al., 2005). However, TEM was used here as final confirmation (**Figure 4.2**). Clathrin-coated structures were counted in spindle and non-spindle regions of orthogonally-sectioned mitotic cells. By taking serial sections of cells through and past the metaphase disk (**Figure 4.2 A**), it was possible to accurately predict and mark spindle and non-spindle zones (**Figure 4.2 B**). Clathrin coated and non-clathrin coated structures could be discriminated by the density of the vesicle coat (**Figure 4.2 C**).

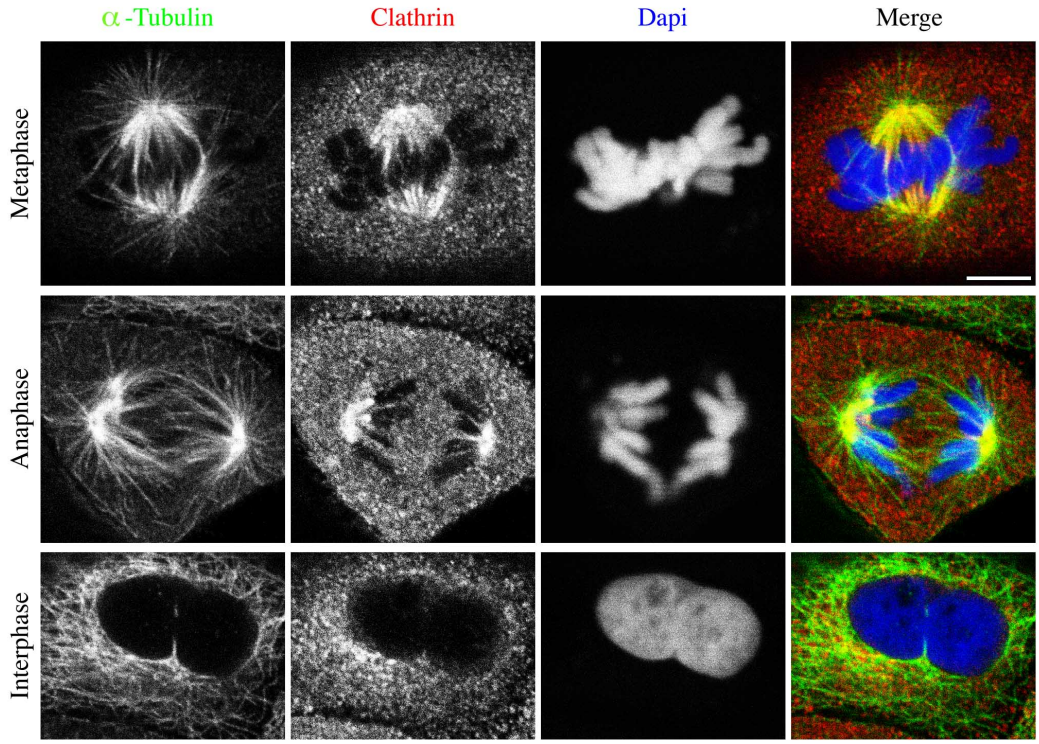

Figure 4.1 – Clathrin localises to the mitotic spindle. Representative confocal images of PtK1 cells fixed for immunofluorescence and labelled with antibodies targeting α-tubulin and clathrin. DNA was stained using dapi. Micrographs show the localisation of both clathrin and tubulin during metaphase, anaphase and interphase. Scale bar, 7 μm.

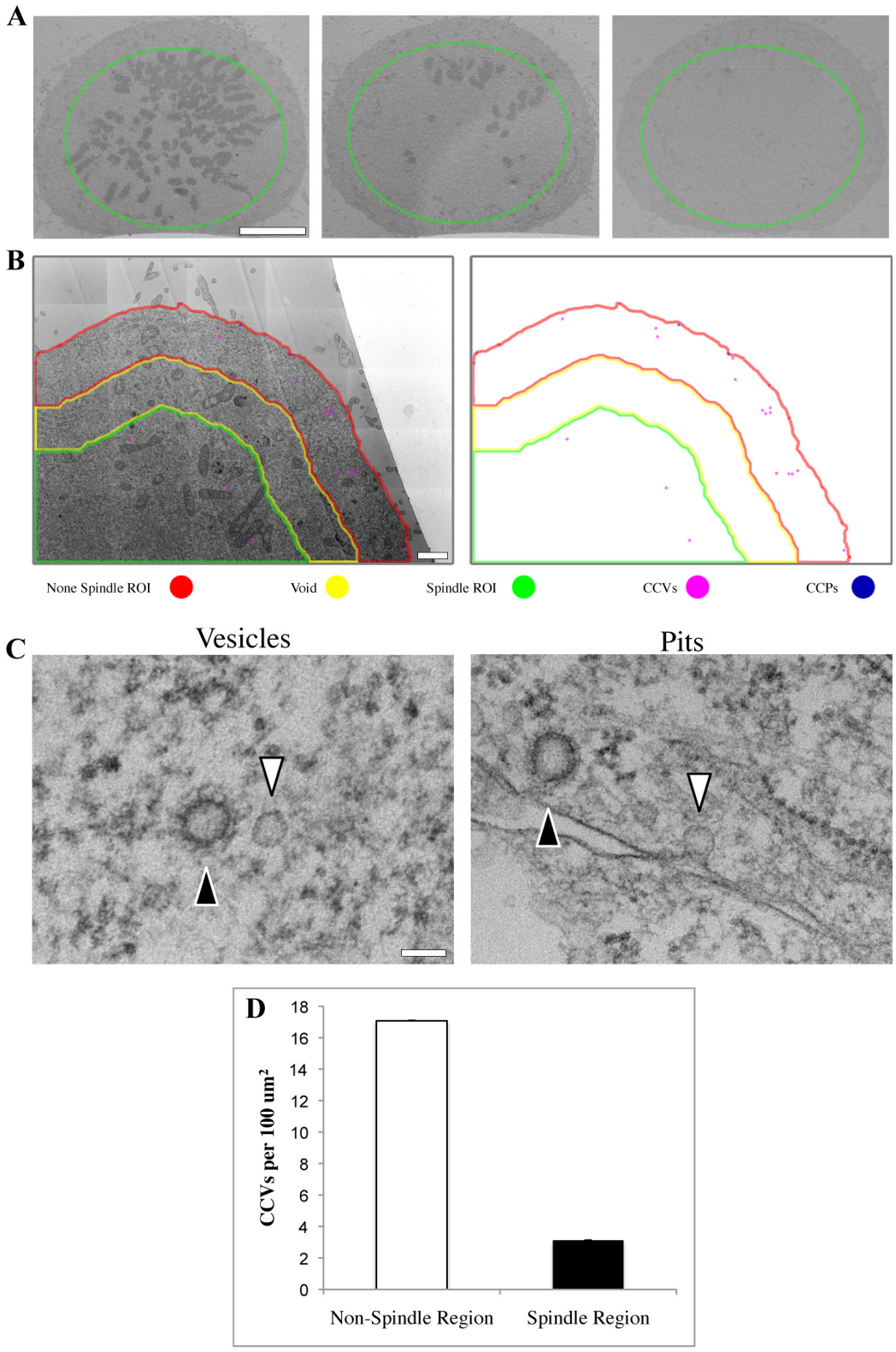
A
B
None Spindle ROI
Void
Spindle ROI
CCVs
CCPs
C
Vesicles
Pits
D
CCVs per 100 um²
18
16
14
12
10
8
6
4
2
0
Non-Spindle Region
Spindle Region

Figure 4.2 – CCVs are not enriched in the mitotic spindle. HeLa cells were processed for EM and sectioned orthogonally through the spindle. **(A)** Electron micrographs showing which cross-sectional area of the spindle was analysed. MIAs (5x5) were taken of cells ~1.0 μm past the metaphase disk. A cross section through the centre of the disk can be seen (A – left). Progressive serial sections no longer contain chromosomes, but a spindle region can still be predicted (green). Scale bar, 4 μm. **(B)** A representative MIA demonstrating the quantification method. Cells were divided into three zones: spindle region (green), non-spindle region (red) and a "void" buffer zone (yellow). CCVs and CCPs were counted and annotated in each zone. Scale bar, 500 nm. **(C)** Representative images of clathrin-coated (black arrows) and non-clathrin-coated (white arrows) vesicles and pits. Scale bar, 100 nm. **(D)** A bar chart showing vesicle quantifications. Annotated vesicles were quantified and interpreted as CCVs per 100 μm^2. $n_{cell} = 3$; $P < 0.001$, bars are mean ± s.e.m

A comparative analysis revealed that the density of CCVs in non-spindle regions (17.1 CCVs per 100 μm^2) was far greater than in spindle regions (3.1 per 100 μm^2) (**Figure 4.2 D**). This argues that the accumulation of clathrin at the spindle apparatus is not an enrichment of CCVs.

4.4.3 Target proteins can be depleted using pBrain vectors

In order to study the ultrastructure of spindles in cells depleted of target proteins, an RNAi vector system was used. The pBrain vector is a dual promoter DNA construct, which expresses an shRNA together with a fluorescent reporter (**Figure 2.1 A**), an approach that is necessary for correlative analysis using light and electron microscopy (**Figure 3.3**). Other projects in the lab had uncovered that spindle clathrin is in a complex with TACC3 & ch-TOG (Booth et al., 2011), therefore three pBrain-GFP-shRNA vectors were generated/used. To test the knockdown efficiency of the constructs, cells were transfected with the appropriate pBrain-GFP-shRNA vector and processed for immunofluorescence (**Figure 4.3**). The level of fluorescence observed in knockdown cells was measured and compared with that of control cells. Clathrin, TACC3 and ch-TOG pBrain plasmids induced an 81%, 83% and 82% reduction in fluorescence, respectively (**Figure 4.3 A, B & C**). In addition many clathrin and TACC3 depleted cells exhibited mitotic defects such as chromosome misalignment. Cells depleted of ch-TOG exhibited a far stronger phenotype. The levels of knockdown reported were an acceptable level, the constructs were therefore appropriate for use in an ultrastructural study.

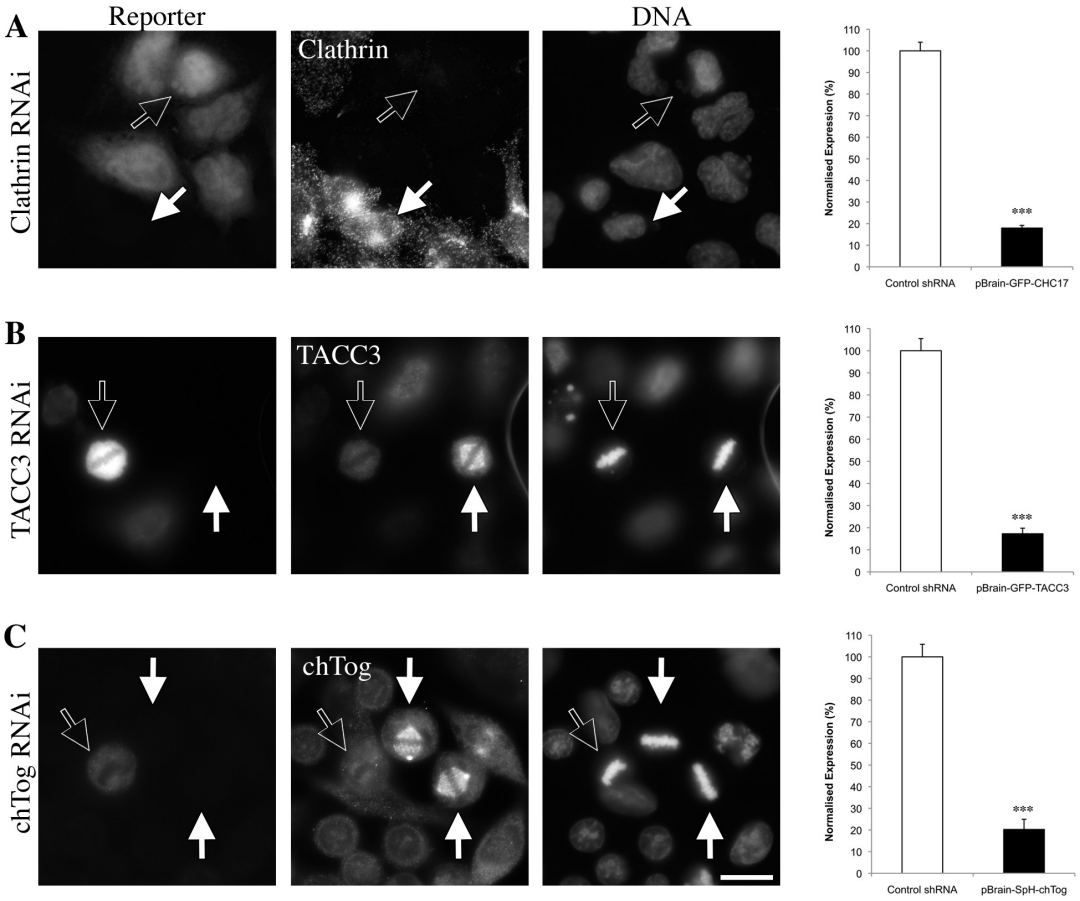

Figure 4.3 – pBrain vectors allow efficient depletion of target proteins. HeLa cells transfected with pBrain plasmids targeting CHC, TACC3 or ch-TOG were assessed for knockdown efficiency using immunofluorescence. Knockdown periods were for 2 days (TACC3 and ch-TOG) or 5 days (CHC). (**A, B & C - images**) Representative fluorescence images showing that transfected cells (black arrows) were depleted of the target protein. Untransfected cells (white arrows) showed no depletion. Scale bar, 20 ⌠m. (**A, B & C – bar charts**) The level of endogenous protein remaining in transfected cells was quantified and compared to control cells transfected with pBrain-GFP-shRNA targeting rat CHC. Bars are mean ± s.e.m., *** = $p < 0.001$. n_{cell} = 26-94.

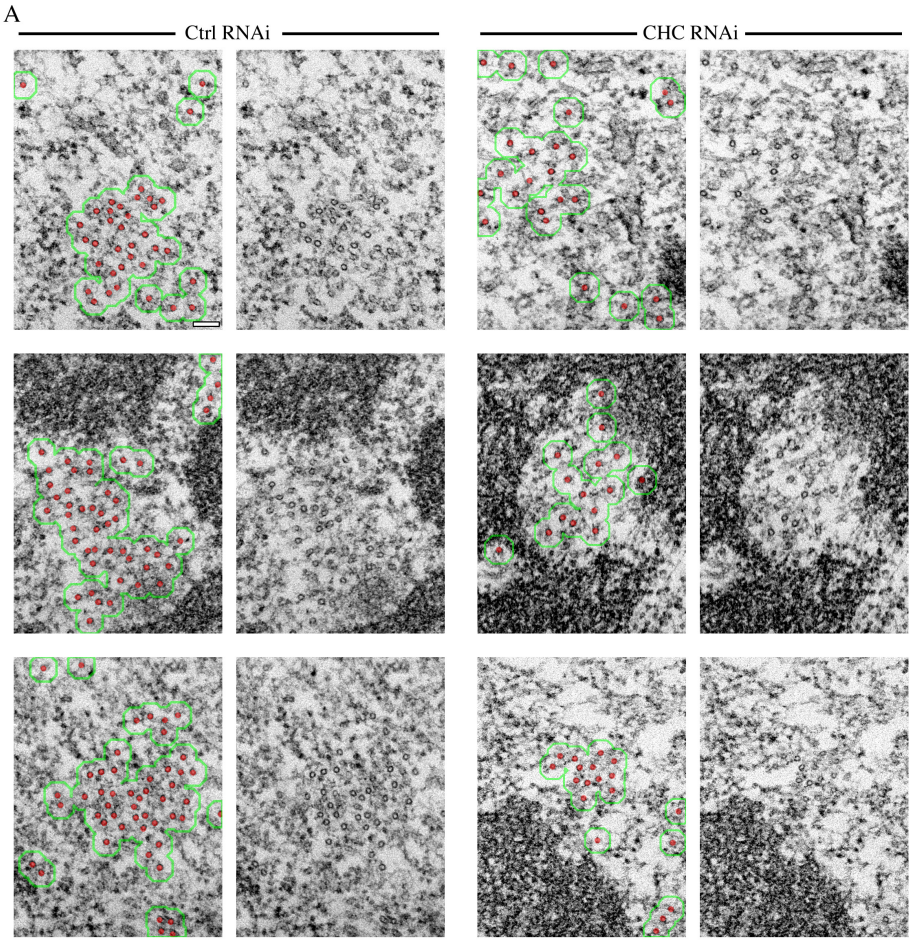
A
Ctrl RNAi
CHC RNAi

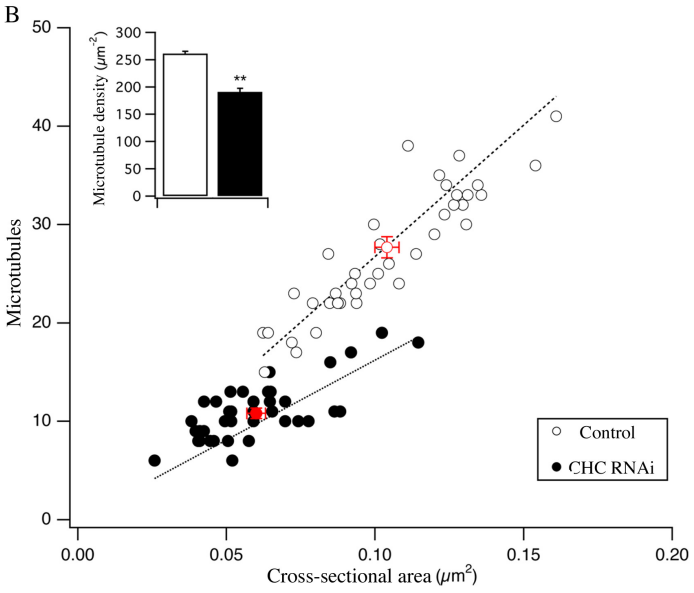
B
Microtubule density (μm-2)
300
250
200
150
100
50
0
**
Microtubules
50
40
30
20
10
0
0.00
0.05
0.10
0.15
0.20
Cross-sectional area (μm2)
Control
CHC RNAi

Figure 4.4 - K-fibres have fewer microtubules following clathrin depletion. (**A)** Representative electron micrographs of orthogonal sections from control or clathrin-depleted HeLa cells. (**A – left**) MTs are annotated in red and the K-fibre perimeter is highlighted in green. (**A – right**) un-annotated micrographs. Scale bar, 100 nm. **(B)** Scatter plot showing the number of kMTs per K-fibre versus cross-sectional area of the fibre. Markers represent the value for individual K-fibres from control RNAi cells (open) or CHC RNAi cells (closed). Red markers represent the mean ± s.e.m. Dashed line is a line of best fit constrained through the origin, the slope of which indicates MT density. (**B - inset**) a bar chart to show MT density, n_{cell} = 4–6; *** = P<0.01.

4.4.4 Depletion of clathrin induces loss of kMTs

To gain a better understanding of clathrin's function at the spindle, the ultrastructure of clathrin-depleted cells was studied. This was achieved using correlative microscopy of pBrain-GFP-CHC transfected HeLa cells. This study reasoned that since clathrin depletion decreased K-fibre stability by light microscopy (Royle et al., 2005), an ultrastructural phenotype may be observed using TEM.

In clathrin depleted cells there was a decrease in the number of kMTs per K-fibre (10.8 ± 0.5) compared with control RNAi cells (27.7 ± 1.1) **(Figure 4.4)**. In addition, the cross-sectional area of K-fibres in clathrin-depleted cells was also decreased, compared with controls **(Figure 4.4 A and B)**. MT loss following clathrin RNAi was not simply a reduction in fibre thickness because the density of kMTs in K-fibres from clathrin-depleted cells was also lower than controls (**Figure 4.4 B – inset**). To gain insight into the change in MT organisation of the K-fibres, the distance between each kMT and its nearest neighbouring kMT was measured. By allocating these measurements into 5 nm bins it was possible to observe the distribution of inter-MT spacing (**Figure 4.5**). The change in MT density (revealed in Figure 4.4) is supported by the histogram in **Figure 4.5 A**, which shows that there is a shift in distribution of inter-MT distances. The mean inter-MT distance was greater in clathrin depleted K-fibres (34.5 nm), compared to fibres from control cells (19.2 nm) (**Figure 4.5 A-inset**). To test whether the kMT loss, observed in clathrin depleted K-fibres, was confined to discrete sections of the bundles, 'heat maps' of four K-fibres were generated to indicate the number of MTs within 80 nm of each other (**Figure 4.5 B**).

A

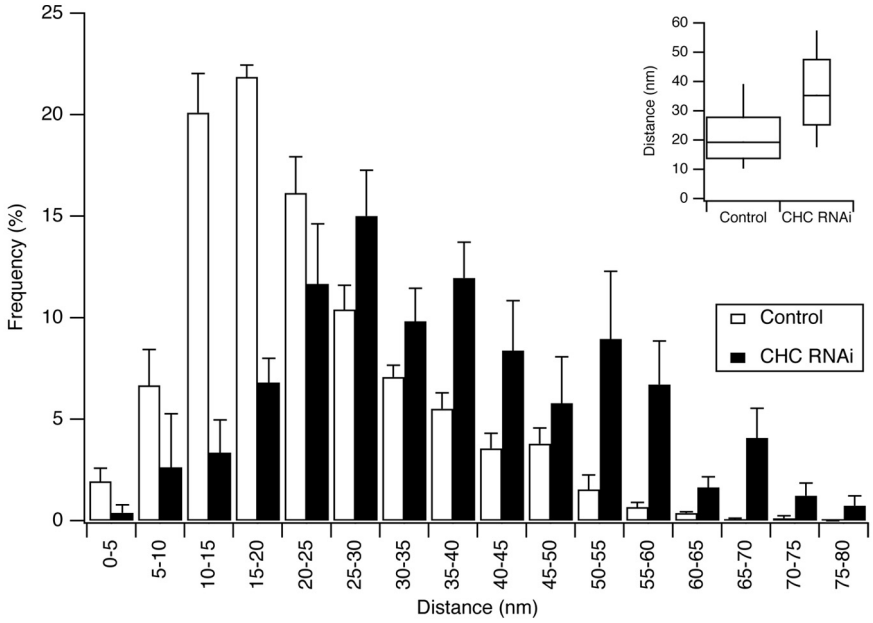
Frequency (%)
25
20
15
10
5
0
0-5
5-10
10-15
15-20
20-25
25-30
30-35
35-40
40-45
45-50
50-55
55-60
60-65
65-70
70-75
75-80
Distance (nm)
Control
CHC RNAi
Distance (nm)
60
50
40
30
20
10
0
Control
CHC RNAi

B

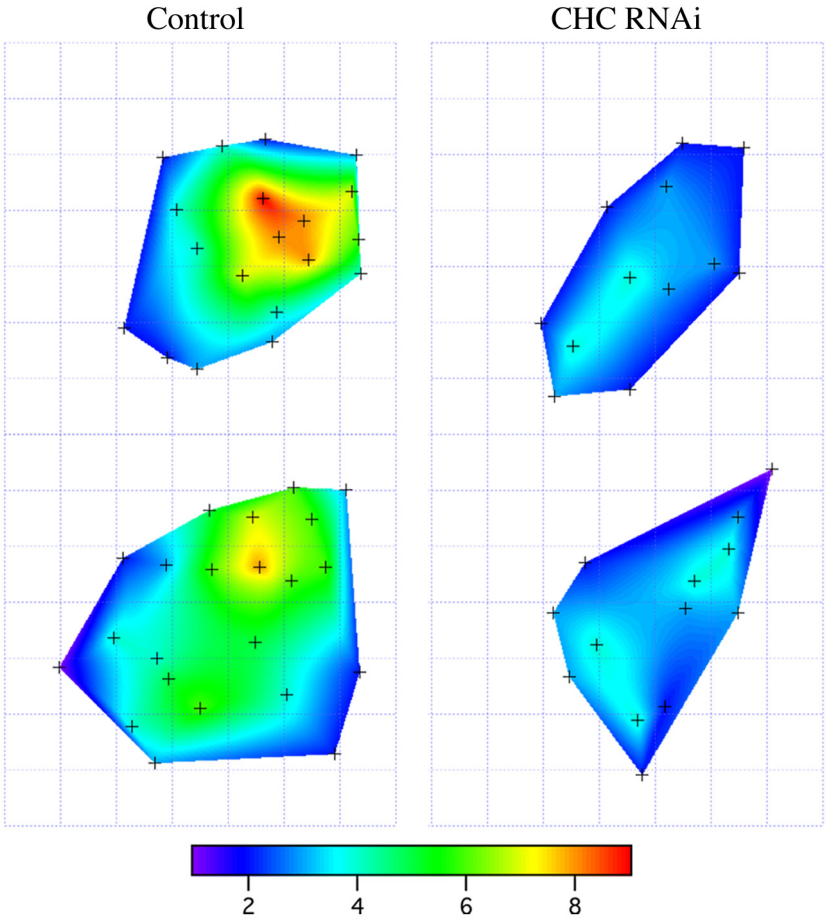
Control
CHC RNAi
2
4
6
8

Figure 4.5 – Clathrin depletion leads to an increase in inter-kMT spacing. (A) A frequency histogram of inter-MT distance between every kMT and their nearest neighbouring kMT within a fibre. Bars represent mean ± s.e.m. n_{cell} = 4–6, n_{fibre} = 41–38 (control versus CHC RNAi). **(A-inset)** A Tukey plot showing median inter-MT nearest neighbour distances, n_{MT} = 1135–420. **(B)** Example 'Heat maps' of typical K-fibres from control or CHC RNAi cells. Every individual MT within a fibre is plotted, assigned with a coordinate. A Voronoi interpolation 2D surface was used to indicate the number of MTs within 80 nm. The largest inter-MT bridge analysed was ~80 nm, this was therefore used as the definition of 'neighbouring MTs within bridging distance of one another'. Tukey plot bar height shows (from bottom) 10^{th}, 25^{th}, 75^{th} and 90^{th} percentiles.

The large areas of light and dark blue found in the heat-maps of clathrin depleted K-fibres, demonstrate that kMT loss occurred equally throughout the K-fibre, as opposed to specific MT loss in certain positions of the bundle. Had the loss observed not been equal, then multiple patches of dense red and yellow regions would have been seen. All of the MTs plotted onto the heat maps were within 80 nm of another MT, this parameter was chosen as this was the largest inter-MT bridge observed during the bridge analysis (data shown in the next section). The heat maps therefore also demonstrate that there was a decrease in the number of neighbouring MTs within bridging distance of one another.

At this stage we have revealed that depletion of clathrin results in a decrease in K-fibre stability and a loss of kMT organisation, demonstrated by a loss of kMTs and an increase in inter-MT spacing.

4.4.5 Clathrin depletion reduces inter-kMT bridge frequency

To directly test the idea that clathrin is a component of inter-kMT bridges we analysed bridges in cells depleted of clathrin. If clathrin is indeed a bridge, then a loss, or perhaps change in bridge structures would be expected.

Figure 4.6 shows that clathrin-depleted K-fibres contained fewer inter-MT bridges compared to controls (4.1 vs 6.9 bridges per μm of total MT). As the depletion of clathrin resulted in a loss of kMTs and an increase in inter-MT spacing it was considered whether this might influence the bridge data, therefore, during the longitudinal bridge analysis the bridge frequency was normlised, not only to total MT length, but also to paired MT regions. The loss of inter-MT bridges was not simply a function of kMT loss as the bridge frequency per μm of paired MTs was also reduced (13.8 vs 15.2 bridges per μm) (**Figure 4.6 B**).

Inter-MT bridges were occasionally observed during the orthogonal analysis and they gave the impression that, compared to control cells, the remaining bridges in clathrin RNAi cells were longer (**Figure 4.6 A & 4.7 A**). Based on this observation it was decided that measurement of inter-MT bridge lengths (from the bridge frequency data) might be useful. The bridge length measurements were allotted into 5 nm bins. In clathrin-depleted cells there was a clear shift in the distribution of bridge lengths, apparently showing that the remaining bridges were longer than bridges from control cells (**Figure 4.7 B**). Indeed, the median bridge length in clathrin-depleted cells had increased from 18.4 to 29.7 nm (**Figure 4.7 B inset**).

4.4.6 Clathrin depleted K-fibres exhibit a loss of a population of short inter-MT bridges

The bridge length data indicated that remaining bridges in clathrin depleted cells were longer than controls, or, an alternative explanation was that a specific population of bridges were removed following clathrin-depletion. To test this, idea a probability density function of bridge lengths between data sets was carried out. Prior to this, to improve histogram resolution, the data was allotted into smaller 2 nm bins (**Figure 4.8 A**). Both the control and clathrin RNAi data sets could not be fitted adequately with a single curve, rather, both sets of data exhibited multiple peaks (**Figure 4.8 B**).

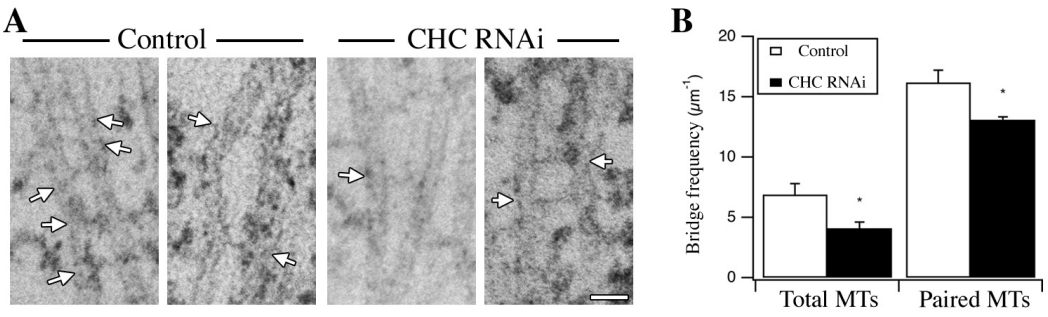

Figure 4.6 – Clathrin depletion reduces inter-MT bridge frequency. (**A**) Representative electron micrographs of longitudinally sectioned kMTs from control and CHC RNAi cells. Clathrin-depleted K-fibres exhibited a loss of inter-MT bridges. Arrows highlight examples of inter-MT bridges. Inter-kMT bridges were identified using established criteria; 2 – 5 nm-thick projections of electron-dense material that connect two microtubules (Hepler et al., 1970). (**B**) A bar chart of inter-MT bridge frequency, normalising the data as bridges per μm of total MT length or per μm of paired MTs (MTs within 80 nm neighbouring distance). Bars show mean ± s.e.m; P = 0.05. Scale bar, 40 nm.

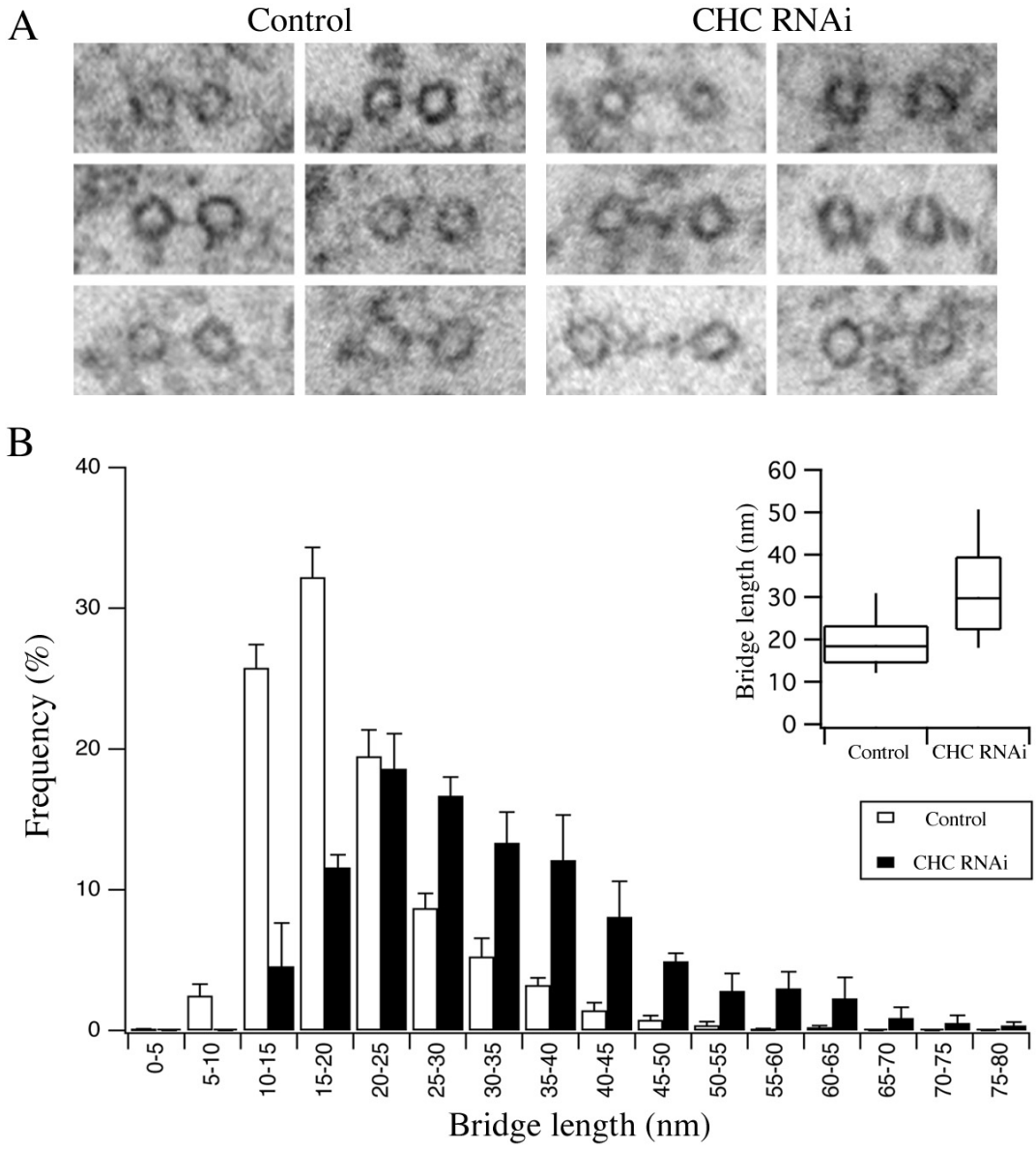

Figure 4.7 – Clathrin-depleted kinetochore fibres show a change in bridge length distribution (**A**) A gallery of electron micrographs, chosen at random, showing orthogonally sectioned microtubules. An apparent increase in inter-kMT bridge length was observed following clathrin RNAi. (**B**) Frequency histogram of inter-MT bridge-length distributions from control and clathrin RNAi cells. Mean ± s.e.m, n_{cell} = 3–4. (**B inset**) A Tukey plot showing median length of all bridges, n_{bridge} = 1335–570. Bar width reflects $n_{bridge.}$ Bar height shows (from bottom) 10th, 25th, 75th and 90th percentiles.

A multi-peak analysis of the bridge distributions revealed four discrete populations of bridge in control data (**Figure 4.8 B**), with mean lengths of 15 nm, 21 nm, 27 nm and 53 nm (**Figure 4.8 C - top**). The same analysis of clathrin-depleted bridge length data, revealed only three populations of inter-MT bridge, with mean lengths of 22 nm, 34 nm and 53 nm. Although there was a small increase in the number of longer bridges in the clathrin RNAi data, the most obvious difference was that a population of short inter-kMT bridges was absent (**Figure 4.8 B & C**). The 15 nm population of bridge present in the control data accounted for ~50% of the total bridges, this subset was almost non-existent following clathrin depletion. A small increase in the 27 and 53 nm bridge subsets could also be seen (**Figure 4.8 C**). Collectively, the alterations in bridge length data, as a consequence of clathrin depletion, account for the 40% reduction in bridge frequency (per μm of total MT) and the apparent shift in bridge length.

To summarise this part of the chapter, an ultrastructural analysis revealed that clathrin depletion leads to: (a) reduction in the number of kMTs in a K-fibre bundle, (b) a change in the kMT organisation, c) loss of a population of clathrin dependent short inter-MT bridges.

4.4.7 Clathrin localises to inter-MT bridges in K-fibres

The ultrastructural analysis so far had uncovered a population of clathrin dependent, short, inter-MT bridges. Although the presence of these bridges is clathrin dependent, the current data do not clarify whether the bridge itself is composed of clathrin. To address this, correlative immunogold-labelling of HeLa cells was carried out (**Figure 4.9**).

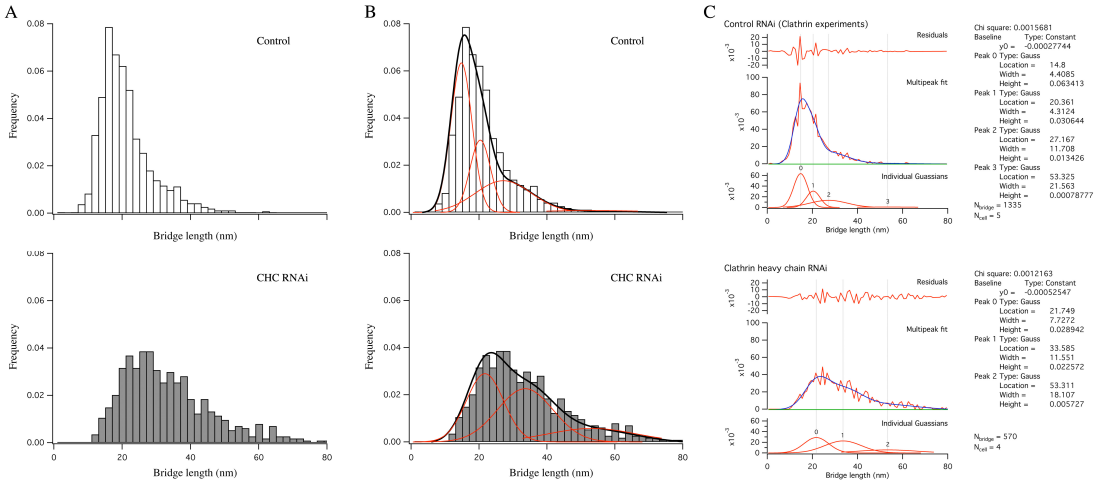

Figure 4.8 – Clathrin-depleted K-fibres exhibit loss of a population of short inter-MT bridges. (**A & B**) Frequency histograms showing the distribution of bridge lengths for all bridges, to indicate putative bridge populations (with and without analytical annotations). A Multi-peak analysis revealed four populations of bridges in control cells and only three populations in clathrin depleted cells (**B**). Individual populations, red; sum of populations, grey/black. (**C**) Histograms showing the individual Gaussian peaks and associated output data, residuals for the peaks are shown at the top. The mean lengths of bridges from control cells were 14.8, 20.7, 27.2 and 53.3 nm. The mean lengths of bridges from clathrin-depleted cells were 21.7, 33.6 and 53.3 nm. The multi-peak analysis of control data uncovered an additional 14.8 nm bridge population. $n_{bridge} = 1335–570$ (control vs RNAi)

The distribution of anti-clathrin immuno-gold was compared with that of anti-tubulin immuno-gold. Mitotic HeLa cells expressing GFP-α-tubulin or GFP-CHC (both constructs expressed a GFP fusion protein where GFP was at the C terminus) were processed for CLEM following a cytosolic wash out and labelled with primary and gold-conjugated secondary antibodies (**Figure 4.9 A**), as described in **2.3.3.3**.

The tubulin labelling was, as expected, closely associated with kMTs (**Figure 4.9 B & C**), with a median distance of 8.9 nm from kMT centres to the gold-labelled tubulin (**Figure 4.9 C, D & F**). In contrast, gold particles labelling clathrin were frequently found positioned more distal from MT edges (**Figure 4.9 B**) with a median distance of 18.8 nm from MT centres (**Figure 4.9 C, D & F**). Interestingly, whereas tubulin labelling was equally associated with all MTs (52.6% paired-MTs & 47.4% single-MTs), clathrin-targeted gold particles were found to show preference for paired MTs (88.8% paired-MTs). The combined length of a primary and secondary antibody complex is estimated at 16 nm (Ottersen, 1989). This was factored into the quantification parameters determining the maximum distance a gold particle could be from an inter-MT bridge before it was considered non-specific. Nearly 54% of clathrin labelled with gold particles were associated with inter-MT bridges, compared to only 8.8% of tubulin labelling (**Figure 4.9 E & F**). The 34.9% of clathrin labelled with gold that was found between paired MTs, but was not associated with inter-MT bridges is likely to be due to: poorly stained bridges, bridges lost in-between sections or due to some bridge structures being only partially assembled. In summary, the immunogold labelling provides evidence suggesting that inter-MT bridges in K-fibres contain clathrin.

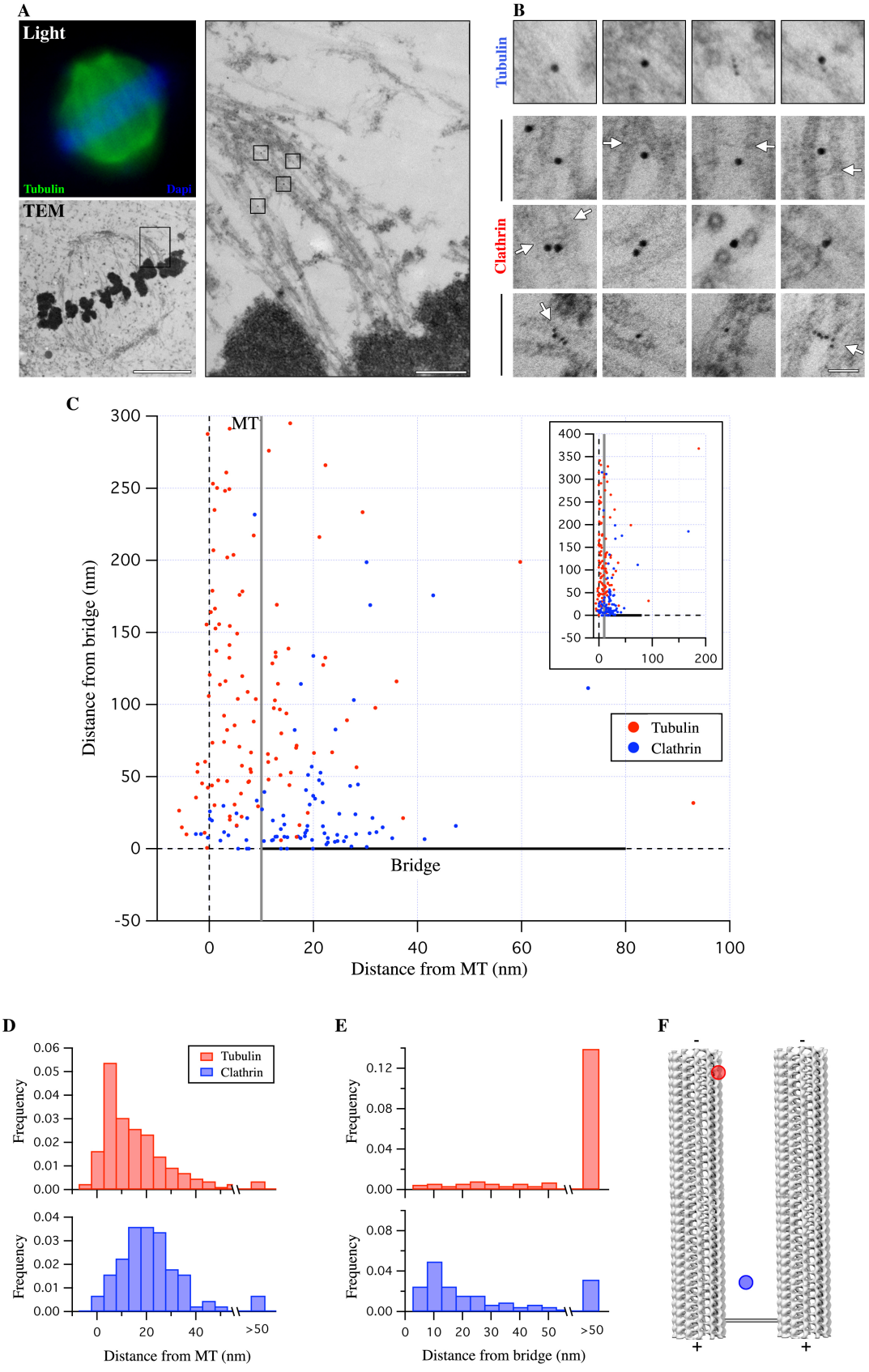
A
Light
Tubulin
Dapi
TEM
B
Tubulin
Clathrin
C
MT
Distance from bridge (nm)
Distance from MT (nm)
Bridge
Tubulin
Clathrin
D
Frequency
Distance from MT (nm)
E
Frequency
Distance from bridge (nm)
F

Figure 4.9 – Clathrin is localised to inter-MT bridges in K-fibres. (**A**) Representative correlative light and electron microscopy images of a mitotic HeLa cell expressing GFP-α-tubulin following a cytosolic 'washout' and immunogold labelled. (**A right**) A zoom of the two K-fibres boxed in the TEM 'cell overview'. Scale bars, 5µm (overview) and 500 nm (zoom). (**B**) Representative electron micrographs showing immunogold labelling of tubulin and clathrin. Cells expressing GFP-α-tubulin or GFP-CHC were probed with anti-GFP and either anti-tubulin or anti-CHC antibodies. Primary antibodies were detected with 5 and 10 nm gold-conjugated secondary antibodies. Bridges are marked with arrows. (**B – tubulin**) High magnification of the four gold-labelled kMTs boxed in **A**. (**B - clathrin**) Representative examples of gold-labelled clathrin. (**C**) A 2D plot illustrating gold particle positioning relative to MTs (x-axis) and the nearest inter-MT bridge (y-axis). MT and bridge edges are represented by grey and black lines, parallel to the x and y axes, respectively. (**C inset**) A condensed overview of the 2D plot in **C**. (**D & E**) Frequency histograms of gold particles relative to MTs (nearest MT centre) and bridges (nearest inter-MT bridge) for tubulin and clathrin gold. $n_{tubulin} = 120$, $n_{clathrin} = 89$. (**F**) A scaled model of two MTs and an idealized inter-MT bridge. Red and blue dots represent the median distances of tubulin and clathrin gold particles, respectively.

4.4.8 Depletion of TACC3 causes loss of inter-kMT bridges

This project has established that there is a clathrin dependent population of short inter-MT bridges, in addition, immunogold labelling has been able to implicate clathrin as part of the bridge structure. During this study, other work in the lab uncovered that clathrin cannot bind directly to MTs *in vitro*, rather it required the presence of mitotic extract, indicating that a binding partner is required. Shortly after, clathrin at the spindle was found to be in a complex with TACC3 and ch-TOG (Royle et al., 2011, Hubner et al., 2010, Lin et al., 2010). As the TACC3/ch-TOG sub-complex was thought to be responsible for clathrin recruitment, it was reasoned that depletion of TACC3 or ch-TOG should yield a similar phenotype to clathrin depleted cells, for example, they should show a loss of inter-MT bridges. This was tested using CLEM to study the ultrastructure of K-fibres from TACC3 and ch-TOG depleted cells. Indeed, the K-fibres of TACC3 depleted cells contained fewer inter-kMT bridges (**Figure 4.10**), where a 35% reduction in bridge frequency per unit length of total MT was seen. Once again this was not a function of change in MT loss or spacing as there was also a decrease in bridge frequency per unit length of paired MTs (**Figure 4.10 B**).

As these results were very similar to those from clathrin-depleted cells, it was reasoned that the loss of bridges maybe a specific population of bridge. The bridge lengths in controls and TACC3 depleted cells were measured and allotted into 5 nm bins (**Figure 4.10 C**). As seen previously with the clathrin analysis, there was a shift to the right in the distribution of bridge lengths, furthermore the median length of inter-MT bridges increased from 19.8 nm in control cells to 30.4 nm in TACC3 RNAi cells (**Figure 4.10 C - inset**).

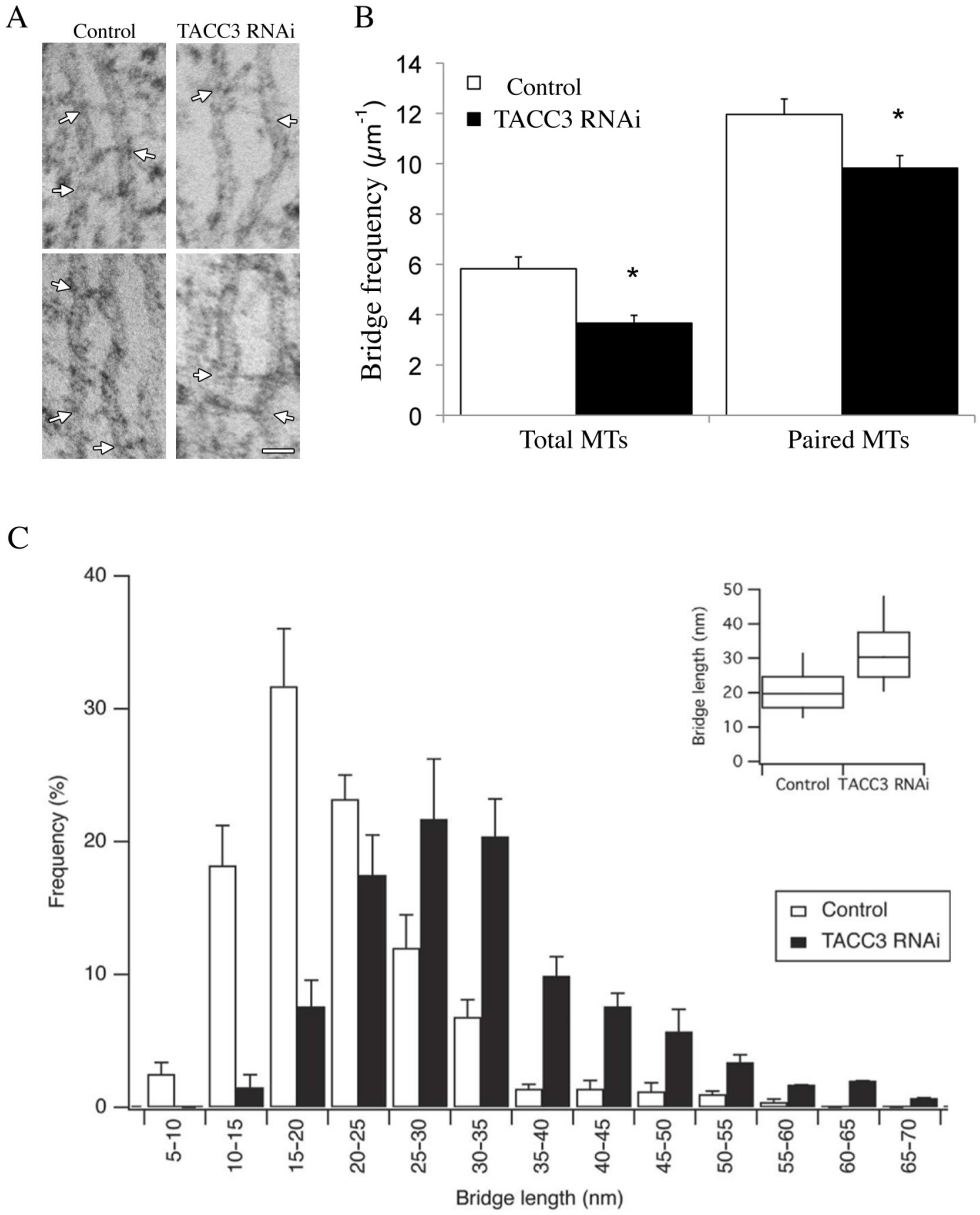

Figure 4.10 – TACC3-depleted K-fibres exhibit a loss of inter-MT bridges. (**A**) Representative electron micrographs of longitudinally sectioned kMTs from control and TACC3 RNAi cells. Arrows mark bridges. Scale bar, 40 nm. (**B**) A bar chart showing bridge frequency normalised to total MTs or paired MTs (MTs within 80 nm of each other). Bars show mean ± s.e.m; p = 0.01. (**C**) A histogram showing the distributions of inter-MT bridge lengths from control or TACC3-depleted cells. Mean ± s.e.m, n_{cell} = 6–7. (**C – inset**) A Tukey plot showing the median bridge length of all bridges from control and TACC3 RNAi cells, n_{bridge} = 732–406.

To reveal whether there was a loss of a discrete population of inter-MT bridges, a multi-peak analysis of bridge distributions was once again carried out (**Figure 4.11**). In controls, the analysis revealed three populations of bridge with mean lengths of 17, 24 and 50nm. The TACC3-depleted multi-peak analysis also uncovered three populations, with mean bridge lengths of 29, 47 and 62 nm (**Figure 4.11 B & C**). The 17 nm bridge population from control data, which comprised 54% of the total bridges, was negligible within the TACC3 RNAi data. These results indicate that, similar to the depletion of clathrin, TACC3 RNAi results in a loss of a population of short inter-MT bridges from K-fibres.

4.4.9 Ch-TOG depleted K-fibres were extremely disorganised

An ultrastructural analysis of K-fibres from ch-TOG depleted cells was also attempted (**Figure 4.12**). This was done with uncertainty as the depletion of ch-TOG is known to induce a change in spindle morphology (Gergely et al., 2003). The phenotype was so severe that the spindles and K-fibres were mostly too disorganised to analyse (**Figure 4.12**). The K-fibres of control cells were regularly lying in the plane of section, indicating stable kMTs. The K-fibres of ch-TOG depleted cells however, did not lie in the plane of section and MTs were frequently in the wrong orientation (**Figure 4.12 D**). In addition, the poor morphology of spindles following ch-TOG RNAi often had various organelles infiltrating the predicated spindle region, limiting the observation of any reasonable stretches of kMT length (**Figure 4.12 C**). Based on these findings it was decided that an analysis of these cells would not be directly comparable with clathrin and TACC3 depleted cells and was therefore not carried out.

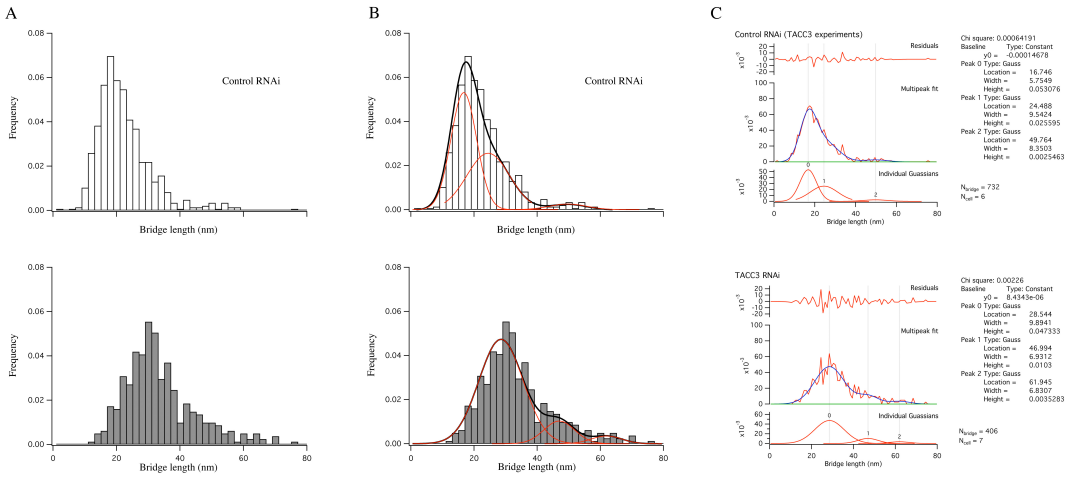

Figure 4.11 - TACC3-depleted K-fibres lack short inter-MT bridges. (**A & B**) Frequency histograms showing the distribution of bridge lengths for all bridges, to indicate putative bridge populations (with and without analytical annotations). A multi-peak analysis revealed three populations of bridges in both control and TACC3-depleted cells (**B**). Individual populations, red; sum of populations, grey/black. (**C**) Histograms showing the individual Gaussian peaks and associated output data, residuals for the peaks are shown at the top. Multi-peak analysis of TACC3 RNAi data (grey, below) indicated three populations with mean lengths of 28.5, 47.0 and 61.9 nm. The multi-peak analysis of control RNAi data revealed an additional 16.7 nm bridge population. n_{bridge} = 732 - 406 (control vs RNAi).

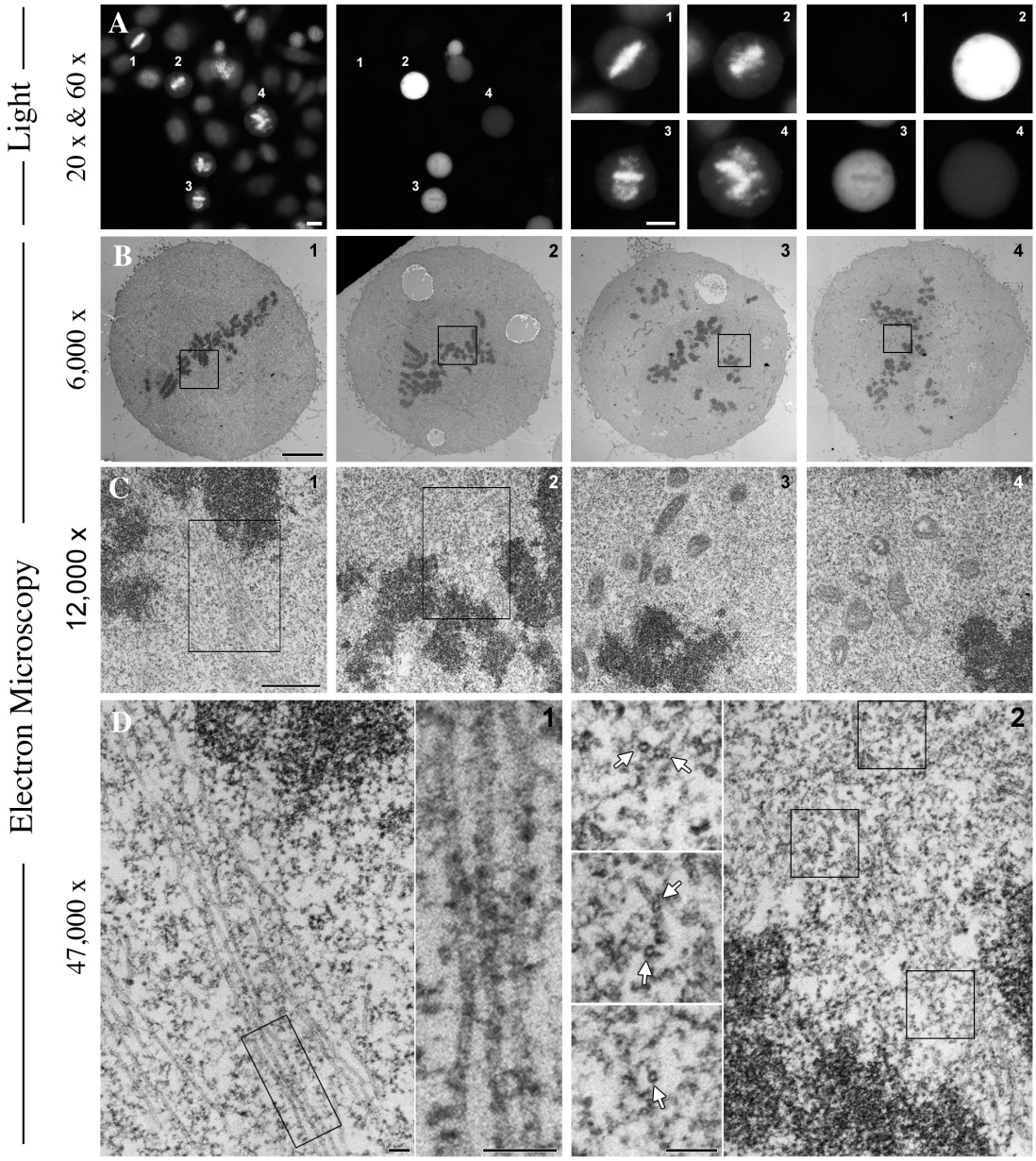
Light
Electron Microscopy
20 x & 60 x
6,000 x
12,000 x
47,000 x
A
B
C
D

Figure 4.12 – Depletion of ch-TOG disrupts spindle morphology. Four cells were studied using correlative light electron microscopy. Cell 1 was un-transfected and acted as an internal control. Cells 2 - 4 show a progressive range of aberrant mitotic phenotypes as a consequence of ch-TOG depletion using RNAi. (**A**) Fluorescence microscopy images of a field containing four cells, which were processed for EM (Left, DNA; Right, GFP). (**B-D**) Electron micrographs. (**B**) Correlative overviews of cells identified in **A**. (**C**) Zoomed views of an area adjacent to the chromosomes that were boxed in **B**. (**D**) High magnification micrographs of the boxed regions from **C**. (**D - inset**) Zoomed views of areas boxed in **D**. Cell #1 (internal control) has a normal K-fibre that can be visualised and analysed normally. Cells #2-4 contain K-fibres that were not parallel to the section and could not be quantified. The zoomed areas in **D** (inset) show MTs that are orthogonal to the longitudinal axis of the spindle. Scale bars, 10 ⌠m (**A**), 4 ⌠m (**B**), 1 ⌠m (**C**), 100 nm (**D**).

4.5 Discussion

The depletion of clathrin induces a number of mitotic defects, including, an increase in misaligned chromosomes and a prolonged mitosis. It is thought that these errors occur as a result of another defect, destabilised K-fibres (Royle et al., 2005). This study has provided an ultrastructural explanation of how clathrin confers kMT stability and organisation. A loss of microtubules (Rubinstein et al., 2009) or inter-MT bridges (Manning and Compton, 2008) has been predicted to reduce K-fibre stability, this ultrastructural study has revealed that clathrin depletion leads to both. A loss of a population of short inter-MT bridges together with fewer MTs per K-fibre was observed. These data suggest that a TACC3/ch-TOG/clathrin complex could promote kMT stability by (i) physically tethering adjacent MTs and (ii) by lowering the rate of MT catastrophe. The latter is a possibility because ch-TOG has a known role as an anti-catastrophe protein (Brouhard et al., 2008).

Other MT cross-linking proteins have been characterised such as PRC1 (Zhu et al., 2006) and KLP-61F (Sharp et al., 1999). These have been found to cross-link anti-parallel MTs at the spindle midzone. In the TACC3/ch-TOG/clathrin complex however, this study has uncovered the first inter-MT bridge in K-fibres.

The lengths of bridges in K-fibres were found to have a complex distribution. A multi-peak analysis was able to resolve this distribution as several discrete populations of bridge. These populations were broadly confirmed in two independent series of experiments. The predicted subsets of bridges can be described as short (14-17 nm), medium (potentially two populations of 20 and 27 nm) and long (>50 nm). The common theme between experiments was a missing population of short inter-MT bridges following clathrin or TACC3-depletion.

Interestingly, these data suggest that bridges of greater lengths are composed of different proteins. Discovering the identity of the other populations of inter-MT bridges would enhance our understanding of how the complete divisions of bridges collectively function to promote kMT stability.

Clathrin only appeared to be associated with short inter-MT bridges, therefore it was necessary to consider how the known dimensions of a clathrin triskelion fit with this population of bridge. The leg of a clathrin triskelion is ~52 nm (Jin and Nossal, 2000) and the short form of inter-MT bridge is <20 nm, at first glance this does not appear a logical fit, however, the analysis carried out during this study measured bridges from the inside edges of adjacent kMTs, meaning clathrin could span a greater distance between the top or bottom edges of kMTs. Indeed the diameter of a MT is ~23 nm (Nogales et al., 1999), therefore two adjacent MTs would provide >45 nm of potential binding ground for clathrin. This hypothesis is supported by the geometric flexibility inferred by the structure of clathrin triskelia (Jin and Nossal, 2000, Heuser and Kirchhausen, 1985, Heuser and Keen, 1988). **Figure 4.13** shows a schematic representation of a model which best reflects the results, where two clathrin legs associate with TACC3/ch-TOG sub-complexes on one MT with the other leg binding to a sub-complex on the adjacent MT.

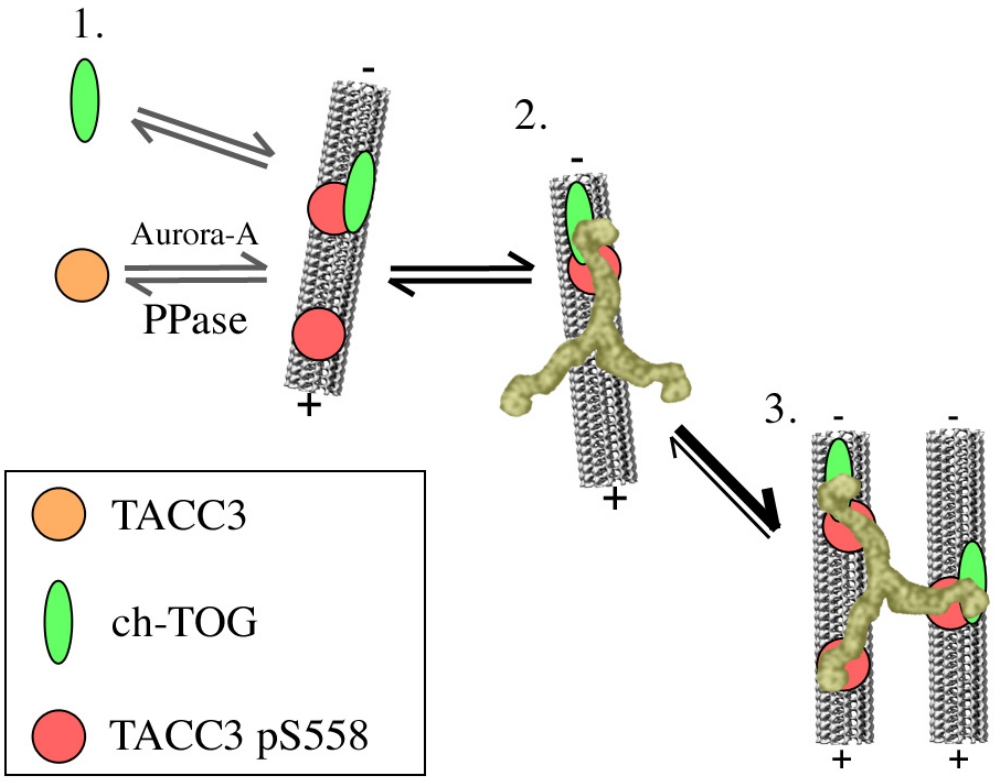

Figure 4.13 – A model demonstrating TACC3/ch-TOG/clathrin and MT binding. Schematic diagram to show the order of recruitment of TACC3/ch-TOG/clathrin complex components. The model is broken down into three stages to show our proposed model of recruitment and accumulation of complexes at the spindle. In this model it is clathrin that is the actual bridge that cross-links parallel MTs. **1. TACC3 recruitment:** aurora-A kinase phosphorylation mediates the recruitment of TACC3 and ch-TOG to MTs, where TACC3 is the primary binding determinant. TACC3 recruits ch-TOG to MTs. **2. Clathrin recruitment:** clathrin binds to TACC3 or TACC3/ch-TOG sub-complexes on MTs. **3. Complex accumulation:** clathrin binds more than one TACC3 or TACC3/ch-TOG sub-complex on adjacent MTs, locking the complex and causing accumulation. The dimensions of clathrin (Heuser and Kirchhausen, 1985) and MTs (Nogales et al., 1999) are approximately to scale.

Collectively the orthogonal and longitudinal analysis of clathrin and TACC3-depleted cells, together with the immunogold labelling, suggest that these proteins are part of a short inter-MT bridge complex that cross-link kMTs. This data is complementary with other work in the lab, which have uncovered the recruitment order of the complex and highlighted the key determinants (**Figure 4.13**). Briefly, TACC3 is phosphorylated on residue S558 by aurora A kinase, promoting binding to MTs and recruitment of ch-TOG (Royle et al., 2011). This sub-complex is now able to recruit clathrin. If there are multiple copies of the TACC3/ch-TOG sub-complex on adjacent MTs this would allow a single clathrin triskelion to make up to three contacts at once, locking it in place and causing accumulation of the complex.

Although the model in **Figure 4.12** is the best interpretation of the data, alternative models could be suggested, such as flexible microtubule associated proteins (MAPs) that link MTs over longer distances. Potentially these MAPs could be compressed, creating the subset of short inter-MT bridges by allowing clathrin to bind TACC3/ch-TOG heterodimers on adjacent MTs. This alternative hypothesis is unlikely as an equivalent number of bridges would have been found, whereas this study observed a net reduction of bridge numbers in K-fibres following depletion of either clathrin or TACC3. A more likely explanation is that remaining bridge complexes are regulated and composed of other protein complexes. Potential candidates could be HURP (Wong and Fang, 2006) and HSET (Mountain et al., 1999). This full cascade of bridge populations and protein complexes could work in cohort, providing a more complete reaction for K-fibre stability.

5 Chapter 5 – K-fibres contain an inter-MT 'mesh'

5.1 Introduction

Inter-kMT bridges are typically defined as electron-dense struts that crosslink parallel MTs (Witt et al., 1981). The descriptions occasionally cover length and diameter of the bridges (Wilson, 1969), but usually offer no further detail. Hepler *et al*. probably provided the most comprehensive detail to date, claiming that bridges can attach to MTs at a variety of angles, form multiple projections on a single kMT and finally, that they sometimes appear 'filamentous' (Hepler et al., 1970). This suggests that inter-MT bridges may not conform to the 'strut' definition.

In keeping with this, during the course of this project it became clear that the inter-MT bridges observed, were not always single 'struts' linking one MT to the next, and instead exhibited structural diversity. A re-review of the literature with this in mind reveals that this is also true of other inter-MT bridges. **Figure 5.1 A** contains a gallery of inter-MT bridges curated from the literature. Some of these bridges conform to the typical definition (**Figure 5.1**). Others show inter-MT structures that would more appropriately fit the descriptions proposed by Hepler *et al*. A more thorough examination of the control RNAi data collected during this project drew similar conclusions. Although a portion of inter-MT bridges were uniform 'struts' (**Figure 5.1 B**), a large number of bridges possessing curves, multiple projections and varying lengths/diameters were also observed (**Figure 5.1 B**). In addition, since clathrin is a three-legged protein it was important to consider why more triskelion shaped bridges were not readily observed. In light of these findings, an improved view of inter-MT cross-linkers was sought.

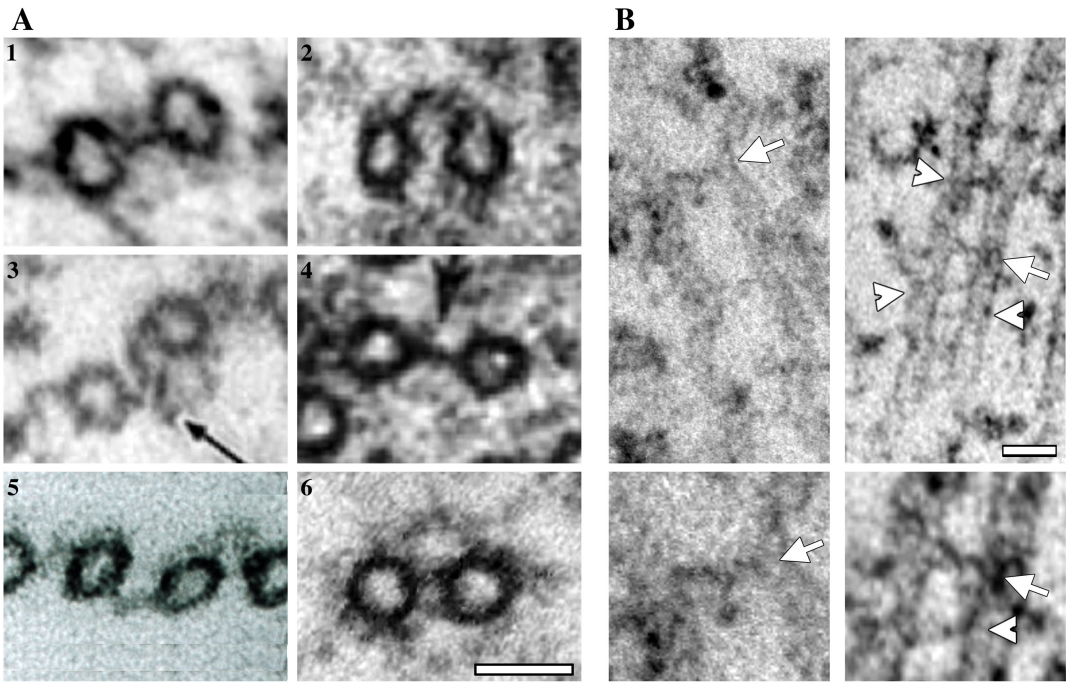

Figure 5.1 – Inter-MT bridges exhibit structural diversity. (**A**) A gallery of electron micrographs showing examples of inter-MT bridges from a variety of species, organelles & cell treatments. **1**) An inter-MT bridge from kinetochore fibres of untreated HeLa cells (Booth et al., 2011). **2**) A curved bridge associated with MTs in the interzone region of the spindle apparatus of the coenocytic green alga *Blastophysa rhizopus* (Wilson, 1969). **3**) An irregular, electron-dense bridge possessing multiple projections. This bridge is from interphase MTs of a cold-treated HeLa cell (Bhisey and Freed, 1971). **4**) An electron dense 'strut' cross-linking MTs from the interzone of a WI-38 cell (Hepler et al., 1970). **5**) MAP65, a cross-linker of cortical microtubules in carrot cells (Chan et al., 1999). **6**) Central MTs from Lamellibranch gill cilia, containing a 'web-like' bridge structures (Warner, 1976). (**B**) Electron micrographs of kMTs longitudinally sectioned containing inter-MT bridges, taken from the RNAi control data in acquired during Chapter 4. Arrows mark bridges that possess geometric variability. Arrowheads mark conventional bridges, described as electron-dense struts. (**B - bottom**) Zoomed examples of bridges marked above. Scale bar, 30 nm.

5.2 Chapter aims

The aim of this chapter was to use advanced methods in electron microscopy to describe the fine structure of inter-kMT bridges. This was attempted using several additional or alternative techniques to those in previous chapters, including:

- High pressure freezing (HPF) and freeze substitution (FS) was used to try and improve the preservation and resolution of bridges
- Electron tomography was used to generate tomographic volumes of kMTs and inter-MT bridges
- Tomograms were used to generate high-resolution 3D models of inter-kMT bridges

5.3 Materials and methods

5.3.1 Indirect immunofluorescence of cold-stable HeLa cells

HeLa cells were transfected (**2.2.4**) to express mCherry-TACC3 for 48 hr, before cold treatment in 4°C DMEM (with supplements) for 5 min. Cells were fixed and processed for immunofluorescence as described in **2.3.2**. Cells were labelled with mouse anti-α-tubulin primary antibody (1:1000) in blocking solution. Fluorophore-conjugated secondary antibody was used to detect the primary antibody. Untransfected control samples were prepared in parallel, these contained cold and non-cold treated cells that were labelled with anti-α-tubulin and anti-TACC3 primary antibodies. Rabbit anti-TACC3 was detected using anti-rabbit fluorophore-conjugated secondary antibody. Once mounted, cells were visualised using an epifluorescence microscope (Olympus).

5.3.2 High pressure freezing and freeze substitution

Two HPF experiments were carried out during Chapter 5. The first used untreated HeLa cells only, these were synchronised and frozen as described in **2.3.3.4** before freeze substitution, as described in **5.3.2.2**. The second experiment contained five batches of HeLa cells, subjected to different treatments, prior to HPF and FS.

5.3.2.1 Preparation of HeLa cells for HPF and FS

Five batches of HeLa cells were conditioned to fulfill three criteria; Control cells (batch 1 & 2), cells depleted of TACC3 (batch 3) and cells overexpressing TACC3 (batch 4 & 5). Each batch of cells was grown in individual 10 cm tissue culture dishes. The conditions were as follows:

1) Untreated HeLa TetOn cells.
2) HeLa TetOn cells transfected with siRNA targeting GL2.
3) HeLa TetOn cells transfected with siRNA targeting TACC3.
4) HeLa TetOn cells, stable with pTRE2hyg-GFP-TACC3(KDP) construct, with no doxycycline treatment for TACC3 induction.
5) HeLa TetOn cells, stable with pTRE2hyg-GFP-TACC3(KDP) construct, treated with 0.1 µg/ml doxycycline, for 48 hr.

The procedure for transfecting cells with siRNA was as follows: 17 µl of oligofectamine (Novagen) was added to 73 µl of Optimem media (containing no supplements), in parallel, 11 µl of siRNA (20 µM), was added to 1000 µl of Optimem media. Both the oligofectamine and siRNA solutions were left to incubate separately for 10 min. The two solutions were then combined and incubated for a

further 10 min. The transfection solution was added to the 10 cm dish (making a total volume of ~5.5 ml). The media was replaced with fresh DMEM (containing supplements) after 6 hr. Cells were depleted of TACC3 for 72 hr.

The GFP-TACC3(KDP) stable-inducible cell line was generated as described in **2.1.2 & 2.2.6**.

5.3.2.2 High pressure freezing and freeze substitution

HeLa cells were synchronised and processed for HPF as described in **2.3.3.4**, before FS and resin embedding. Freeze substitution was carried out as follows: Cells were post-fixed and stained for 26 h in 100% acetone containing 1% OsO_4 and 0.1% UA at -90°C, before incremental temperature ramps to 4°C over a 40 hr period. Two 'stay' periods for 15 hr at temperatures of -60 °C and -30°C were incorporated into the temperature ramps. Cells were washed twice in 100% acetone (30 min), before four resin infiltrations with resin:acetone ratios of 1:2, 1:1, 2:1 and 3:1, for 1 hr per treatment. Samples were brought to RT before 3 washes in 100% resin. The last resin treatment was left on and the samples cured at 60°C for 72 hr. Following polymerisation, resin samples were excised from the FS cast, separated from the copper HPF disks and routinely trimmed and sectioned using a microtome.

5.3.2.3 SDS-PAGE separation of protein

A portion of the cells, synchronised for HPF, were retained for SDS-PAGE separation and Western blotting to determine whether the test conditions were successful. Synchronised, mitotic cells were pelleted by centrifugation at 300 x g for 2 min before resuspension in lysis buffer (20 mM Tris pH 7.5, 150 mM NaCl, 1% Triton-X100, 1X protease inhibitor cocktail (Roche)) and incubated on ice for 30 min. Cell lysates were forced through a 25-gauge needle ten times, before

centrifugation at 16,000 x g for 10 min, after which the supernatant was removed and retained. Protein concentration of lysate was estimated using a BCA assay, according to manufacturers guidelines (Sigma-Aldrich). Approximately 30 µg of protein was prepared for gel loading by the addition of β-ME (to 5%, v/v) and 5 X loading buffer (5 X SDS, 0.5 mM Tris HCL pH 8.0, 5X bromophenol blue, 10% glycerol) before boiling on a dry hot-block for 5 min. Proteins were separated using an 8% resolving polyacrylamide gel, performed using the denaturing and discontinuous system described by Laemmli (Laemmli, 1970). Gels were set-up in BioRad Mini-Protean apparatus, according to the manufacturer's instructions. A 5% stacking gel (2 ml) was made using the following recipe: ddH_2O, 1.4 ml; 30% acryl amide mix, 0.33 ml; 1.0 M Tris.Cl (pH 6.8), 0.25 ml; 10% SDS, 0.02 ml; 10% ammonium persulfate, 0.02 ml; TEMED, 0.002 ml. An 8% resolving gel (5 ml) was made using the following recipe: ddH_2O, 2.3 ml; 30% acrylamide mix, 1.3 ml; 1.5 M Tris.Cl (pH 8.8), 1.3 ml; 10% SDS, 0.05 ml; 10% ammonium persulfate, 0.05 ml; TEMED, 0.003 ml. Protein lysates were loaded onto the gels, alongside Precision Protein All Blue molecular weight standards (Bio-rad). Gels were run for 15 min at 100 V and then 60 min at 150 V in 1 X TGB (50 mM Tris-HCl, 0.1% SDS and 380 mM glycine). Protein was transferred from the gel onto a nitrocellulose membrane (Whatman) using apparatus from Biorad, in transfer buffer. The transfer was for 70 min at 350 mA. Membranes were then processed for Western blotting (**5.3.2.4**).

5.3.2.4 Western blotting

To block non-specific binding of antibodies, nitrocellulose membranes were incubated in 5% fat-free milk (Marvel) in TBS (50mM Tris-HCl, 150mM NaCl, pH7.6) with 0.1% (w/v) Tween 20 for 1 h at RT on a rocker. Membranes were then

incubated overnight (4°C) rocking in primary antibody targeting TACC3 or β-tubulin (1:2000), reconstituted in 2% milk. The following morning, membranes were washed 3 x 5 min with TBS to remove unbound antibody. Primary antibodies were detected using anti-rabbit horse-radish peroxidase (HRP) conjugated secondary antibodies (1:10000) in TBS supplemented with 2% milk for 1 hr at RT. Membranes were washed for 3 X 5 min in TBS to remove unbound antibody. Visualization of protein bands was achieved by incubating membranes in 2 ml enhanced chemiluminescence reagent (ECL) for 5 min, before exposure to X-ray film, which was developed manually.

5.4 Results

5.4.1 Tomography improves the resolution of inter-MT cross-linking structures

To test whether tomography would improve the visualisation of inter-MT bridges, some of the tilt series that were acquired from aldehyde-fixed HeLa cells, were converted into tomograms. Electron tomography is used to generate a 3D reconstruction (tomogram) of a sample from tilted 2D images using IMOD (Kremer et al., 1996, Mastronarde, 1997). The output of a reconstructed tomogram is a computed stack of orthoslices, comparable to the images from a section of confocal Z-stack.

The generation of tomograms offered a more detailed insight of fine sub-cellular structures associated with kMTs (**Figure 5.2**). This was primarily due to the ability of a tomogram to provide depth and volume to the once 2-dimensional electron micrograph. As expected, conventional inter-MT bridges were still observable (**Figure 5.2 A**) and possibly even more frequent, in the tomograms. In addition, analysis of the tomogram orthoslices revealed extra, previously unseen, cross-linking structures (**Figure 5.2 B**). The kMTs and inter-MT bridges could be annotated in a selection of the orthoslices. The painted structures, from individual orthoslices (**Figure 5.2 B**) were reminiscent of the examples shown in **Figure 5.1 or 5.2 A**, however, when the annotations were overlaid, using the MTs as reference points, a more complex structure was revealed (**Figure 5.2 C**). This more highly-resolved bridge appeared to cross-link more than two MTs at one time, exhibiting multiple contact points with three or more kMTs within close proximity.

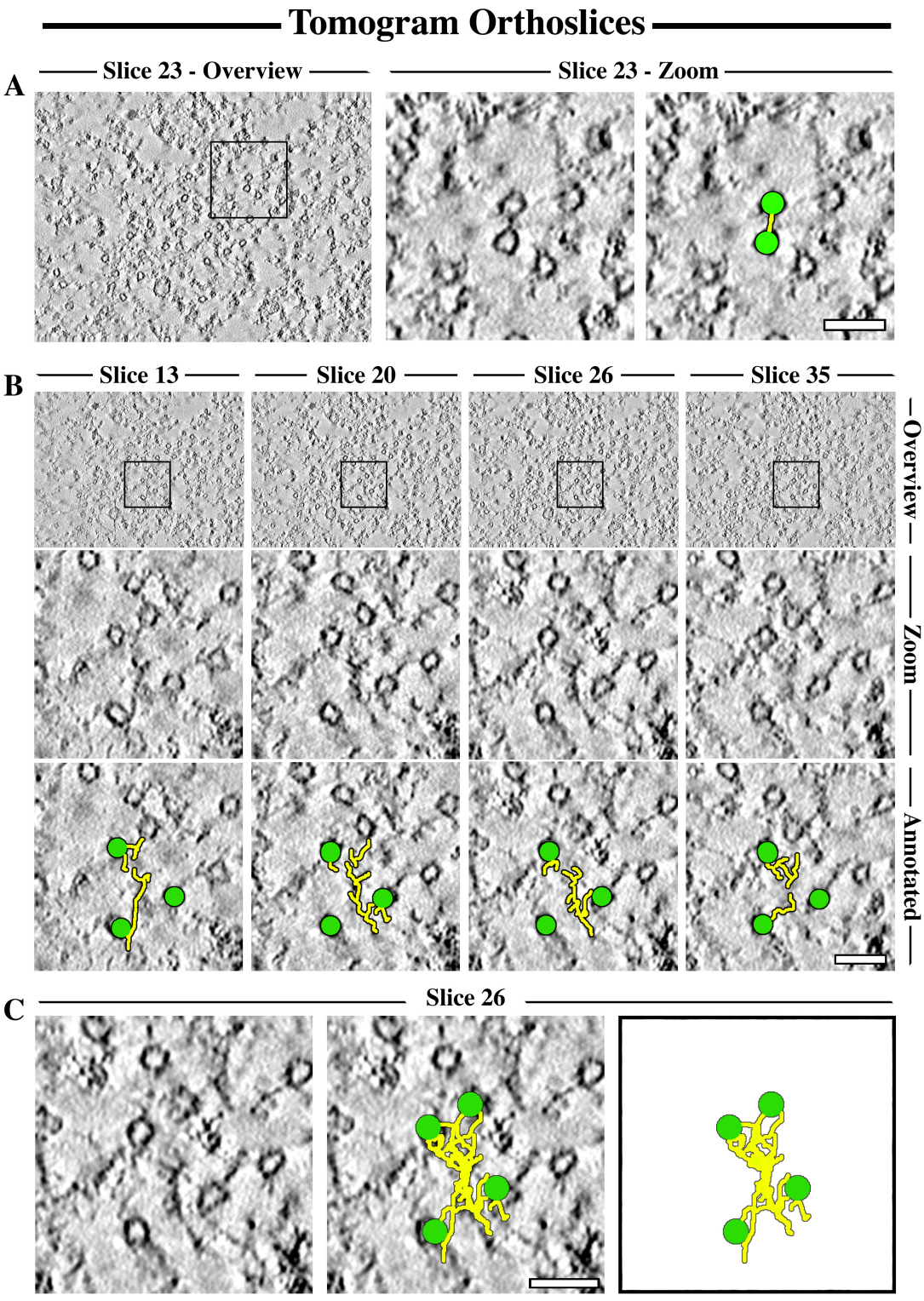
Tomogram Orthoslices
A
Slice 23 - Overview
Slice 23 - Zoom
B
Slice 13
Slice 20
Slice 26
Slice 35
Overview
Zoom
Annotated
C
Slice 26

Figure 5.2 – Tomography of K-fibres reveals complex inter-MT structures. A tomogram was created using a tilt series of a K-fibre acquired for kMT analysis during Chapter 4. The original tomogram contained 50 orthoslices. This figure contains representative orthoslices taken from the tomogram. Annotations were carried out in Adobe Photoshop Elements (PSe). (**A**) A typical orthoslice containing a K-fibre cross-section (**overview**). A zoom reveals a traditional inter-MT bridge. (**B**) Orthoslice numbers 13, 20, 26 and 35 were selected from the tomogram, the K-fibre is present in each slice (**overview**). (**B - zoom**) High magnifications of a region containing several kMTs, and an apparent inter-MT cross-linking structure. (**B - annotated**) Zoomed regions were imported into PSe, where the central kMTs (green) and their associated inter-MT structures (yellow) were annotated on each orthoslice. (**C**) Using the MTs as reference points, the annotations from **B** were aligned and pooled together onto one PSe layer, revealing an inter-MT mesh. The mesh was docked onto a representative orthoslice (**centre**) or onto a clear background (**far right**). Scale bar, 50 nm.

Due to the appearance of these structures, they will be referred to from now on as inter-MT 'mesh'. Although the mesh appeared genuine in the annotated tomogram, it was difficult to define any further properties of the mesh. This was due to two limiting factors: First, using aldehydes for EM fixation is known to limit the resolution of fine, nanometer structures at high magnification. Second, 2-dimensional annotations are not sufficient for a 3D reconstruction of the mesh. In an attempt to overcome these limitations, high-pressure freezing, with freeze substitution (HPF/FS) and 3D rendering were carried out.

5.4.2 Kinetochore MTs are connected by an inter-MT mesh

High-pressure freezing of mitotic cells allowed clear, high-magnification tilt-series of K-fibres to be obtained, resolving fine nanometer structures with greater clarity than aldehyde fixation. This is best demonstrated in **Figure 5.3 A**, where a direct comparison of a kMT fixed using aldehydes (**top**) or HPF (**bottom**) can be seen. The HPF microtubule is perfectly round and allows thirteen protofilaments to be counted. The aldehyde-fixed kMT is comparatively 'fuzzy', meaning that protofilaments cannot be fully resolved.

K-fibres of HPF wild-type HeLa cells appeared even more organised than previously observed, exhibiting more uniformed inter-MT spacing (Compare **Figure 5.3 B** with **Figure 4.4**). More importantly, in addition to conventional inter-MT bridges (**Figure 5.3 B**), tomograms once again revealed an inter-MT mesh (**Figure 5.3 B)**. The extra resolution, as a result of HPF/FS, allowed kMTs and inter-MT mesh in every orthoslice to be annotated with detail, resulting in the generation of a well-smoothed 3D model (**Figure 5.3 C & D**).

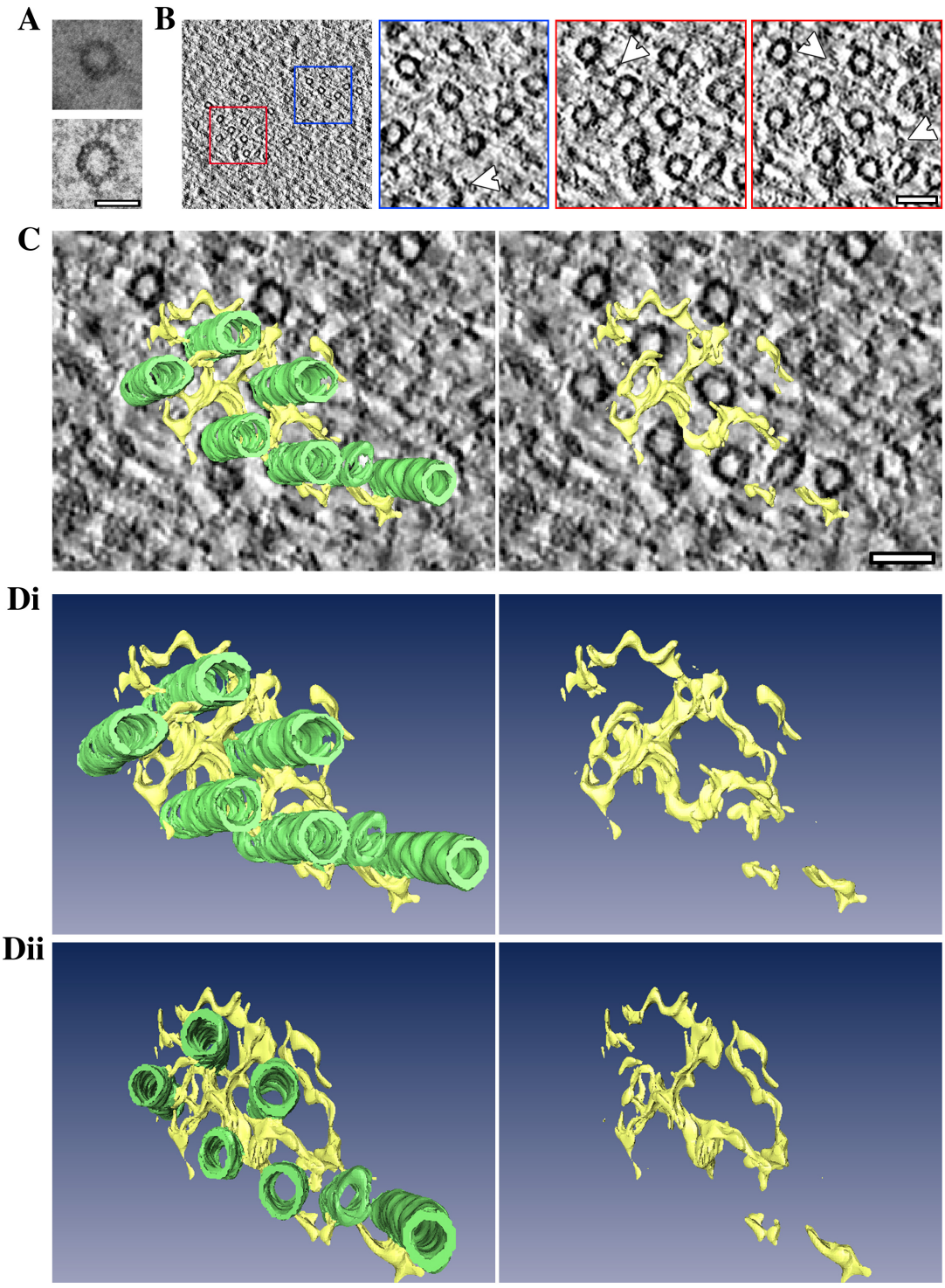
A
B
C
Di
Dii

Figure 5.3 – High pressure freezing allows 3D modelling of inter-MT mesh. **A**) Electron micrographs of two kMTs, one fixed using aldehydes (**top**) and the other using HPF (**bottom**). Magnification, 135,000 X; scale bar, 25 nm. **B)** An orthoslice taken from a tomogram of a K-fibre. Two regions of the overview (**B - left**) that contained kMTs were chosen for high magnification imaging. Zooms show a traditional inter-MT bridge (**blue box**) from one orthoslice and an inter-kMT mesh in two consecutive orthoslices (**red boxes**). Tubulin subunits were also present (**arrow-heads**), found near kMTs and associated with the inter-MT mesh. Scale bar, 50 nm. **C**) Representative, computer-generated, 3D models of kMTs, with inter-MT mesh (**left**) or inter-MT mesh alone (**right**). Figure C shows the kMTs and mesh integrated into the tomogram. **D**) 3D-rendered models of mesh without the tomogram orthoslice. The figure shows the mesh with the kMTs (**left**) or without (**right**), from two different angles; a frontal view (**Dii**) or partially rotated perspective (**Di**). Scale bar, 30 nm.

In generating a 3D model the inter-kMT mesh could be visualised from all angles (**Figure 5.3 C & D**). It is now apparent that the mesh is more convoluted than a simple 'strut', rather, it extends from and contacts several kMTs at once, and also appears to contain mesh 'hubs', found between kMT triangles (**Figure 5.3 C & D**). The mesh appeared to be observable in any area where kMTs were present, exhibiting multiple contact points with the MTs throughout the depth of the tomogram/model. Another interesting observation was the presence of, what appeared to be, tubulin subunits (**Figure 5.3 B**). These were found between kMTs and were usually incorporated into the mesh.

To test whether the mesh was specifically found between kMTs and not present throughout the cytosol, the selection of kMTs modeled in **Figure 5.3** were copied and artificially docked onto random areas where no kMTs were present (**Figure 5.4**). The copied kMTs were not inter-connected by background densities, suggesting that the mesh is specific to the kMTs, as modeled. In addition, the copied kMTs contained electron densities penetrating the MT lumen. In contrast, the genuine control kMTs exhibit clear lumens and had electron dense structures that lead up to and attached to the kMT wall, but do not pass through it (**Figure 5.4**).

5.4.3 Inter-MT mesh promotes kMT organisation

Although HPF and 3D modelling provided good evidence for the existence of an inter-MT mesh, was it possible to assign a function to it? Since previous reports have suggested that inter-MT bridges function in MT organisation (Hepler et al., 1970, Witt et al., 1981, Harada et al., 2002, Zhu et al., 2006, Booth et al., 2011), it would be reasonable to assume that a mesh would perform a similar role.

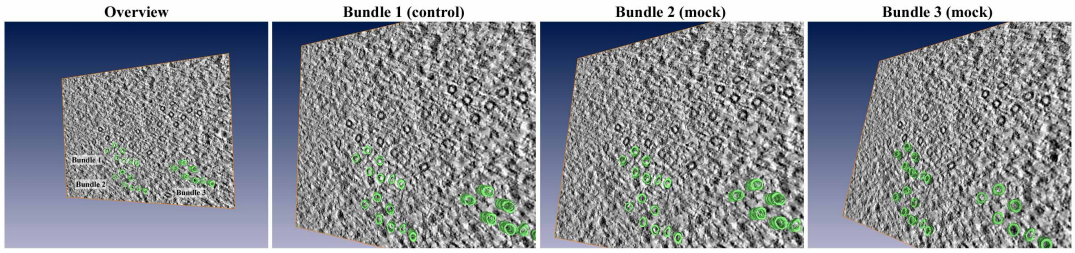

Figure 5.4 – Mesh is found exclusively between kMTs and not throughout the cytosol. MTs rendered in **Figure 5.3** were artificially docked onto random areas of the cytosol, where no MTs were present. Bundle 1 is the original, modeled on genuine MTs. Bundles 2 & 3 are the duplicate 'mock' bundles. The camera viewing angles for the tomogram orthoslices were rotated for bundles 1, 2 and 3 to provide the best camera angle to view the MT lumens in each bundle.

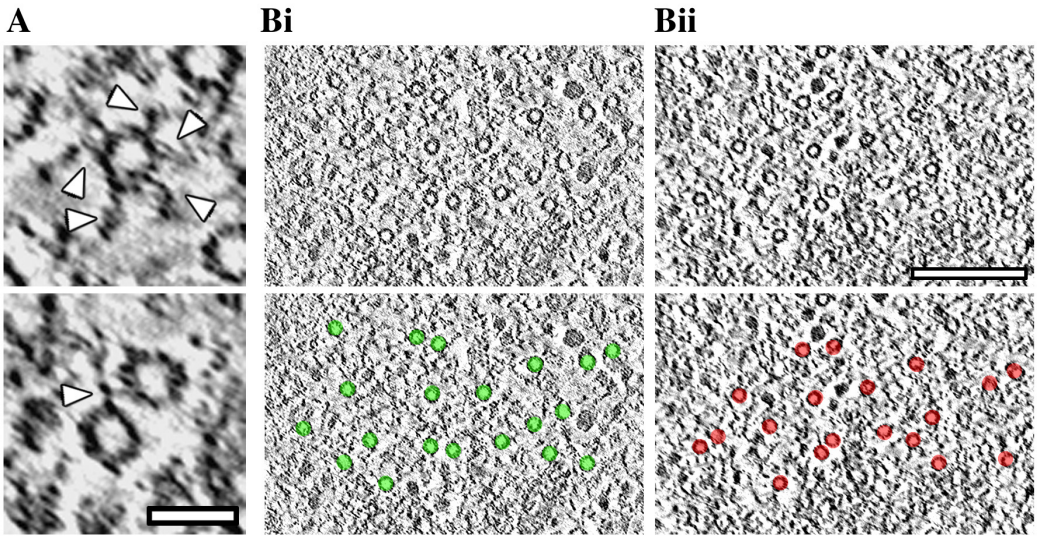
A
Bi
Bii

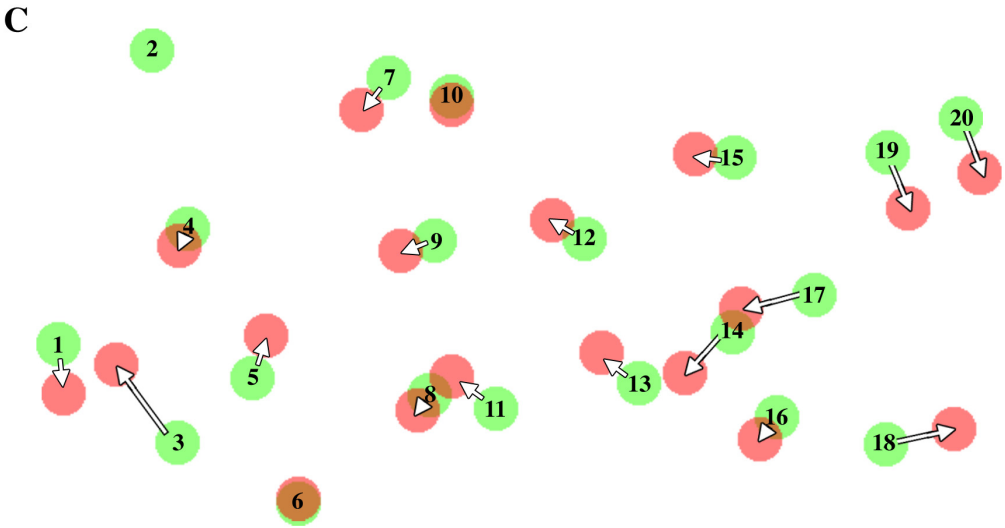
C
2
7
10
20
15
19
4
9
12
17
14
1
5
13
8
11
16
3
18
6

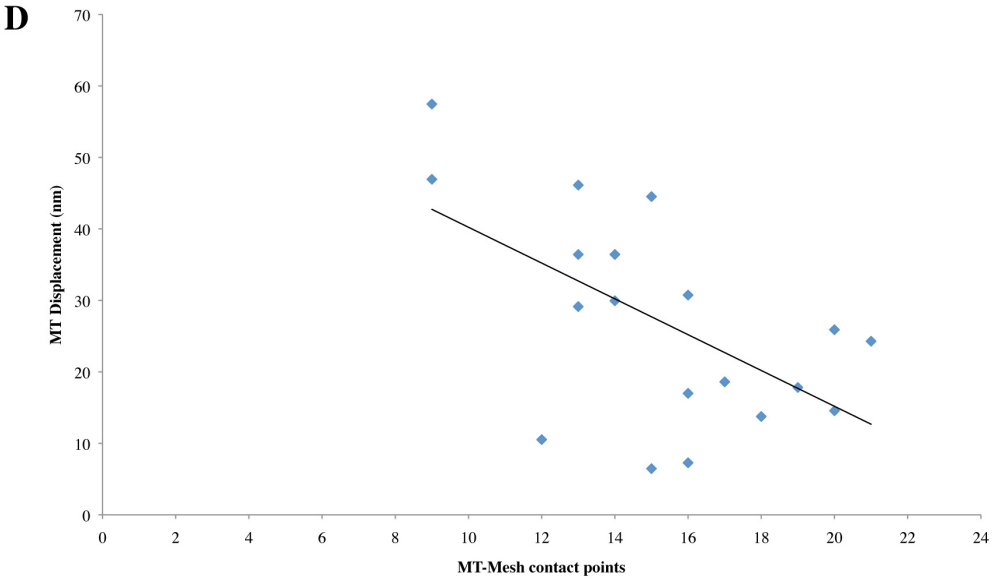
D
MT Displacement (nm)
MT-Mesh contact points
0
10
20
30
40
50
60
70
0
2
4
6
8
10
12
14
16
18
20
22
24

Figure 5.5 – Inter-MT mesh shows a weak association with kMT displacement. A K-fibre was followed through three consecutive sections. A tilt series was taken of each section and reconstructed into a tomogram. The tomograms were aligned using IMOD and concatenated to create a tomographic reconstruction allowing ~300 nm K-fibre cross-section. (**A**) Representative electron micrographs of orthoslices containing MT-mesh contact points (**arrows**). Scale bar, 30 nm. (**B**) Orthoslices from the start (**i**) and end (**ii**) of the tomogram 'join'. MT were marked in orthoslice 1 (**green**) and followed through to orthoslice 90 (**red**). The coordinate position of each kMT was noted in both the first and last orthoslice, from these coordinates, individual kMT displacement was measured. Scale bar, 200 nm. (**C**) A schematic representation of the annotations from **B**, illustrating the amount of MT displacement that occurred throughout the depth of the tomogram. Note that kMT 2 (**top left – green**) was lost in the third tomogram, therefore the displacement and mesh contact was not considered for this MT. (**D**) A scatter plot of MT displacement against the frequency of MT-mesh contact points.

.

To test this, a 'join' of three consecutive tomograms containing a K-fibre were analysed for areas of MT-mesh contact (**Figure 5.5 A**). The serial join allowed the visualisation of ~300 nm of K-fibre cross section. The K-fibre contained 20 kMTs, all of which were monitored for contact points with the mesh. In addition, kMT positions were marked at the start (**Figure 5.5 Bi**) and at the end (**Figure 5.5 Bii**) of the tomogram. Using these positions, MT displacement was calculated (**Figure 5.5 C**). When the frequency of MT-mesh contact points was plotted against level of displacement on (**Figure 5.5 D**) a weak association between frequency of contact points and MT displacement could be seen. The mean kMT displacement was 27.07 ±3.36 and the two kMTs exhibiting the largest amount of displacement (57.47 & 46.95 nm) also had the fewest mesh contact points (9 for both). The mean frequency of mesh contact points was 15, this equates to ~50 mesh contacts points per μm of MT. This is lot higher than the inter-MT bridge frequency uncovered in Chapter 4, this is likely due to the increased resolution of the images as well as the tomographic reconstruction, provided an almost 360° viewing of the kMTs. These preliminary data suggest that the mesh density or level of contact the mesh has with kMTs, directly influences kMT organisation.

To gain more insight, the course of every individual kMT was plotted and annotated to show the frequency of mesh contact points (**Figure 5.6 A**) or number neighbouring MTs (**Figure 5.6 B**). The kMTs with the greatest number of mesh contact points are located towards the centre of the K-fibre bundle, in contrast, the kMTs with the fewest mesh contact points are positioned toward the K-fibre periphery (**Figure 5.6 A**).

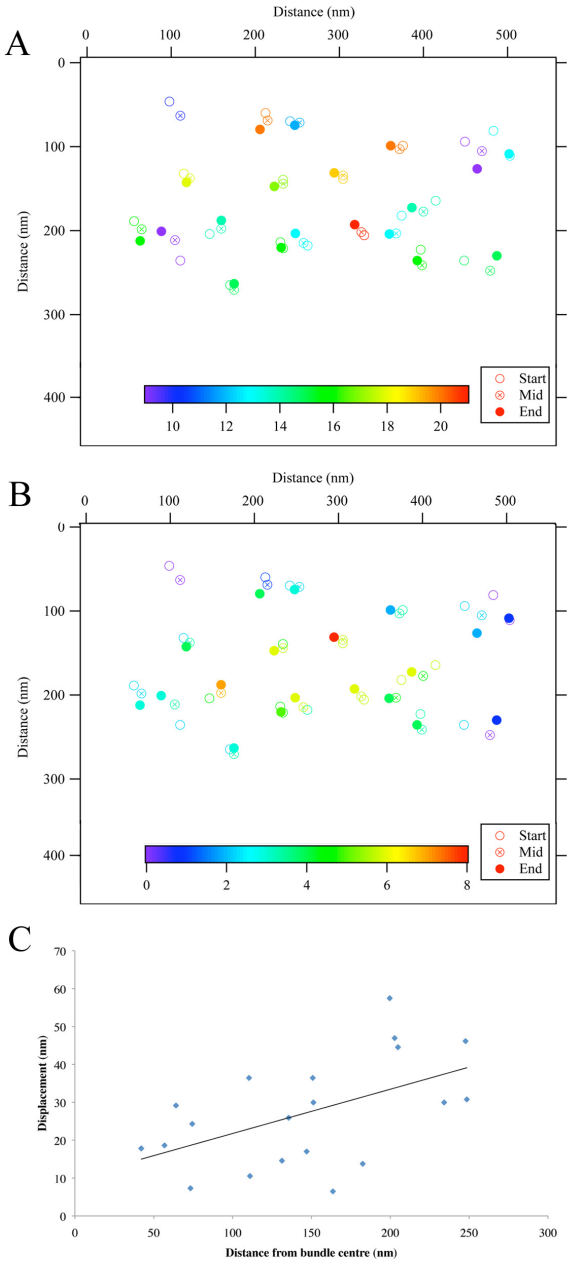

Figure 5.6 – Structural reinforcement is lowest at the K-fibre periphery. A & B) 2D scatter plots containing the 20 individual kMT positions within the tomogram join from **Figure 5.5**. kMT trajectories are shown using a beacon for MT position at the start ○, midpoint ⊗ and end ● of the tomogram. The heat map projections represent, number of mesh contact points (**A**) or number of neighbouring kMTs with 80 nm (**B**). **C**) A scatter plot showing number of mesh contact points against kMT distance from the K-fibre centre.

The heat map of MTs within 80 nm of one another shows, as expected, that the kMT with the lowest neighbour density (purple & blue) are located at the fringes of the bundle, whereas the kMTs with the greatest neighbouring density are positioned at the bundle core (**Figure 5.6 B**). Interestingly, it appeared that the kMTs positioned towards the four corners of the bundle exhibit a greater level of displacement than those in the bundle core (**Figure 5.6 A & B**). To test this, the kMT displacement and proximity to the centre of the fibre was plotted (**Figure 5.6 C**). Indeed it did appear that a weak relationship existed, suggesting that kMTs within close proximity to the bundle centre exhibited less displacement than kMTs positioned more distal from the K-fibre centre. These data imply that, if the mesh does promote MT stability and organisation, the kMTs within the central region of a K-fibre are offered superior reinforcement compared to those at the bundle periphery.

5.4.4 TACC3 expression levels and kMT organisation

In Chapter 4, TACC3 depletion resulted in a loss of a population of short inter-MT bridges in K-fibres. It was considered whether TACC3, in complex with ch-TOG and clathrin influences kMT organisation, possibly via a role in formation or maintenance of inter-MT mesh.

5.4.4.1 Overexpression of TACC3 alters K-fibre morphology

Overexpression of TACC3 has been shown to recruit more ch-TOG and clathrin to the spindle (shown in Booth *et a*l. Figure 3). Using light microscopy it was found that overexpression of mCherry-TACC3 alters K-fibre morphology (**Figure 5.7**). Following overexpression, mCherry-TACC3 concentrated on MTs, making them appear more pronounced. Due to the morphology of these altered MTs, we termed them ‘thread-like’.

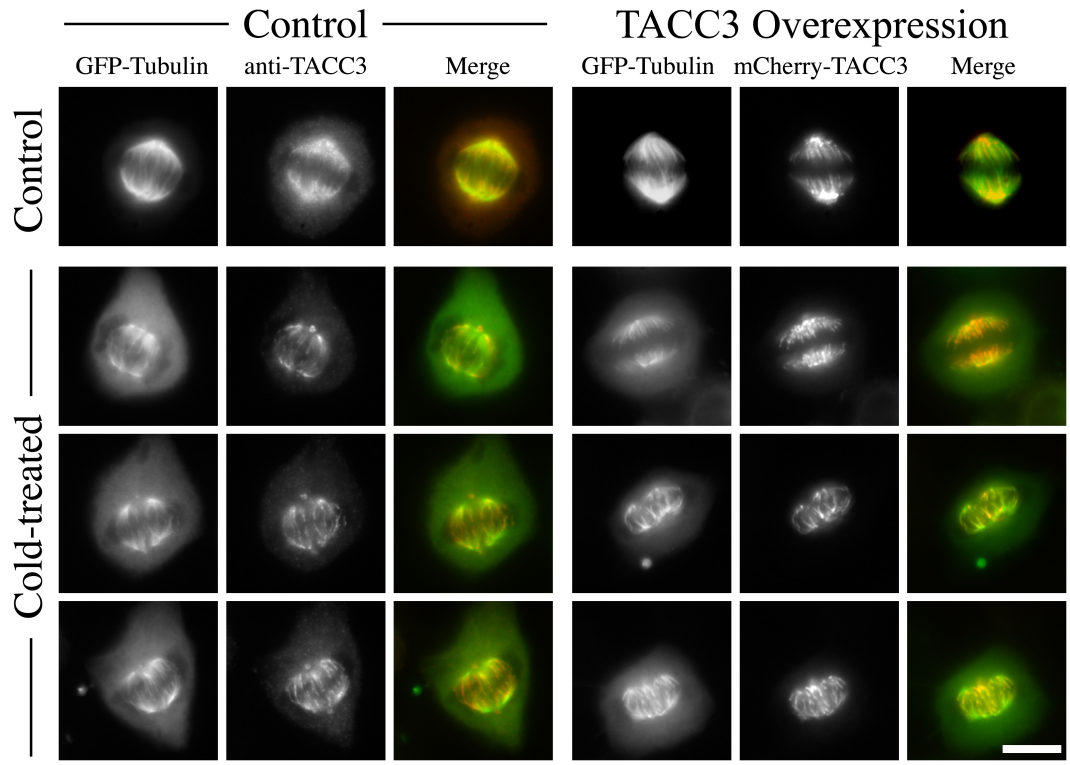

Figure 5.7 – TACC3 overexpression influences K-fibre morphology. Fluorescence micrographs of mitotic HeLa cells showing the effects of TACC3 overexpression. Cells expressed GFP-tubulin (control) or GFP-tubulin and mCherry-TACC3. Following a 48 h expression period cells were cold-treated to selectively depolymerise non-stable MTs before fixation and processing for immunofluorescence. In control cells TACC3 was visualised using anti-TACC3 (rabbit) antibody and an Alexa 568 fluorophore-conjugated secondary antibody targeting rabbit primary. Scale bar, 10 μm.

In contrast, the endogenous TACC3 in control cells was more diffuse throughout the spindle region. The spindle itself, labelled with tubulin, showed typical morphology. To test whether or not the TACC3-positive threads were K-fibres, cells were cold-treated to selectively remove non-stable MTs, such as ipMTs. This revealed three interesting results; first, it was confirmed that overexpressed TACC3 did indeed accumulate specifically on K-fibres. Second, the K-fibres in TACC3 overexpressing cells were more condensed and thread-like than controls. Third, following cold-treatment, spindles of TACC3-overexpressing cells had lost some structural integrity, where spindles appeared to have become compressed. The spindles of control cells showed typical morphology and did not exhibit K-fibre threads. In light of these data, it was considered whether these morphological adaptations, as a result of TACC3 overexpression, were linked to changes in inter-MT bridge or mesh structures. To test this, three categories of HeLa cells; control, TACC3-depleted and TACC3-overexpression, were synchronised, preserved using HPF and analysed using tomography. As CLEM was not compatible with HPF, any cells analysed would have to be a pure population. This was achieved by generating a stable cell line capable of overexpressing GFP-TACC3 following induction with doxycycline (**see 2.1.2**). An attempt was made to generate a stable-inducible, TACC3 knockdown cell line, unfortunately all cell colonies died during clonal expansion. TACC3 depletion was therefore achieved using siRNA, where a high transfection rate was assumed.

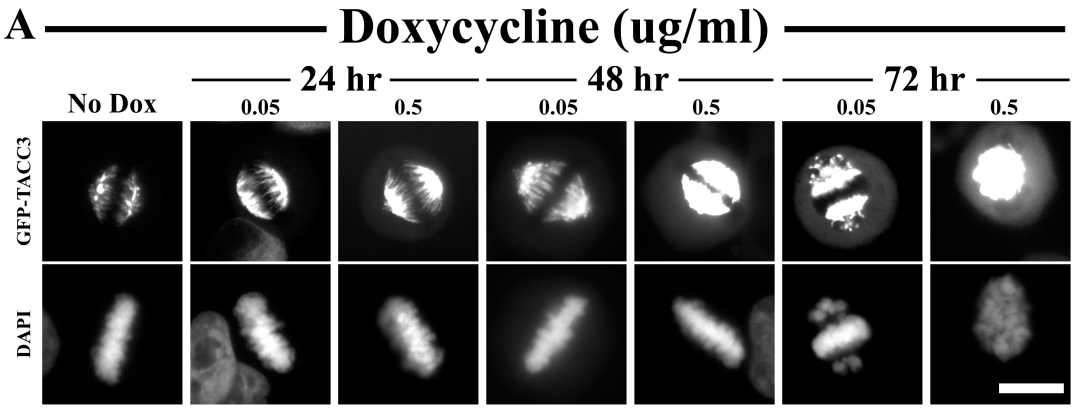

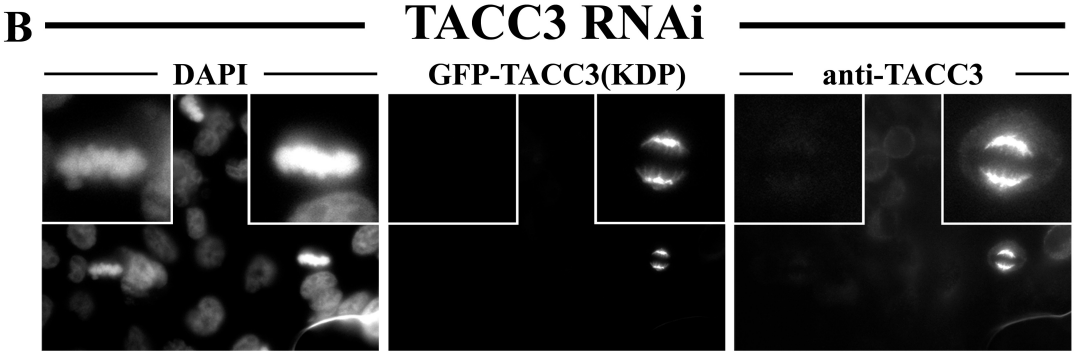

C

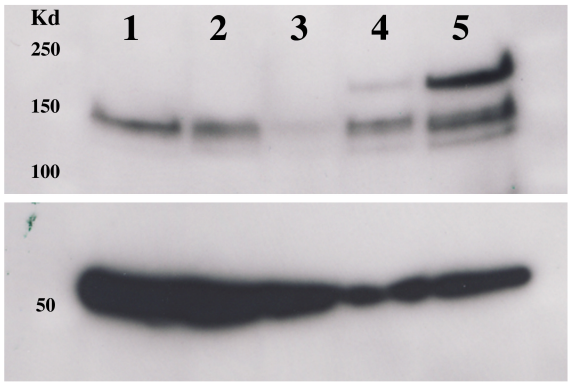

Batch	Endogenous TACC3	GFP-TACC3
1	✓	✗
2	✓	✗
3	↓	✗
4	✓	low
5	✓	high

Figure 5.8 – TACC3 expression levels can be regulated using doxycycline and RNAi. (**A**) Fluorescence micrographs of HeLa cells stably cloned to conditionally express GFP-TACC3(KDP) using doxycycline. A titration of expression periods and two concentrations of doxycycline were tested (0.05 or 0.5 μg/ml) to optimise TACC3 expression. The expression period was set as 24, 48 or 72 hr. Following the desired expression period, cells were fixed and mounted. Control cells with no doxycycline were also prepared. (**B**) Fluorescence micrographs of stable inducible TACC3 HeLa cells, transfected with siRNA targeting TACC3 but no doxycycline treatment. Images contain two mitotic cells; cell one (left) has no GFP-TACC3(KDP) leakage and therefore the siRNA has successfully depleted any endogenous TACC3; cell two (right) shows some GFP-TACC3(KDP) leakage, therefore although the siRNA has likely depleted the endogenous TACC3, the knockdown proof GFP-TACC3 is still present. (**C**) Western analysis of mitotic lysates from HeLa cells. Bands represent TACC3 and β-tubulin. Test conditions for cells are shown in the blot and the table below, these were as follows: Batch/Lanes: **1**) HeLa TetOn cells (untreated); **2**) HeLa TetOn cells transfected with siRNA targeting GL2; **3**) HeLa TetOn cells transfected with siRNA targeting TACC3; **4**) Stable inducible TACC3 cell line (no doxycycline); **5**) Stable inducible TACC3 cell line, treated with 0.1 μg/ml doxycycline for 48 hr.

5.4.4.2 Altering the levels of TACC3 in HeLa cells

To maximise TACC3 overexpression, without causing cell death, a titration of doxycycline and time points was tested (**Figure 5.8 A & B**). A 48 hr treatment of 0.05 µg/ml doxycycline was optimal, yielding a level of TACC3 expression that was high enough to induce a change in K-fibre morphology, but low enough for cells to remain viable (**Figure 5.8 A**). Unfortunately, the cell line was 'leaky': cells perpetually expressed low levels of GFP-TACC3, even without induction (**Figure 5.8 A**). Therefore this cell line, in the absence of doxycycline could not serve as a control in an experiment to test the effects of TACC3 overexpression. Moreover, as the version of GFP-TACC3 that is expressed by the cells is knockdown proof (KDP), then they also could not serve as TACC3 depleted cells either (**Figure 5.8 B**), without using two siRNAs. To overcome this issue, the parental cell line used originally for the generation of the stable GFP-TACC3 cell line, were used for control and for TACC3 RNAi conditions.

When cells were synchronised and processed for HPF/FS a portion of the pelleted cells were set aside to prepare lysates to assess the TACC3 expression status of each HeLa cell sample analysed by EM. **Figure 5.8 C** shows that TACC3 RNAi (lane 3) and TACC3 overexpression (lanes 4 & 5) was successful. The two control lanes (1 & 2) show a similar level of TACC3 expression. Only a very faint band can be seen in lane 3, showing that TACC3 depletion using siRNA had worked efficiently. Doxycycline treatment resulted in GFP-TACC3 overexpression that was ~4-fold greater than the endogenous TACC3 (lane 5). Once the test conditions had been verified, the HPF, resin-embedded samples were prepared for EM analysis.

5.4.4.3 K-fibres overexpressing TACC3 are disorganised

During TEM analysis of TACC3 overexpressing cells three K-fibres, sectioned orthogonally to the spindle axis, were identified and deemed appropriate for study. Individual tilt series and subsequent tomography revealed several morphological aberrancies, some of which were unique to each fibre. The common theme however was a gross change in MT organisation within the K-fibre (**Figures 5.9 & 5.10**). The first K-fibre exhibited severely misshapen MTs (**Figure 5.9 B**), an observation that was partially noticeable in the second K-fibre (**Figure 5.10 A**). The change in shape was not artefactual as perfectly round MTs could clearly be seen nearby (**Figure 5.9 C**). In fact, the lack of distortion of MTs, not associated with the bundle, argues that the distortion of MT shape is bundle-specific and could be caused by the mesh. Interestingly, the kMTs with the greatest distortion also appeared as MT doublets linked by a thick electron-dense bridge (**Figure 5.9 B**). In addition the inter-kMT spacing of the bundle in **Figure 5.9 B** appears less uniform and organised compared to those from the control kMTs (**Figure 5.9 A**). Preliminary spatial analysis using Ripley's L-function confirmed this, showing that control kMTs dispersed as an ordered array with a spacing of ~40 nm. The kMTs in the TACC3 overexpressing K-fibre were less dispersed and had reduced inter-kMT spacing. The irregularities described were confirmed in a rendered 3D model of the MTs (**Figure 5.9 C**).

The second K-fibre analysed from a TACC3 overexpressing cell, displayed poor kMT organisation (**Figure 5.10 A**). This was demonstrated by several incorrectly orientated kMTs within the bundle (**Figure 5.10 A**).

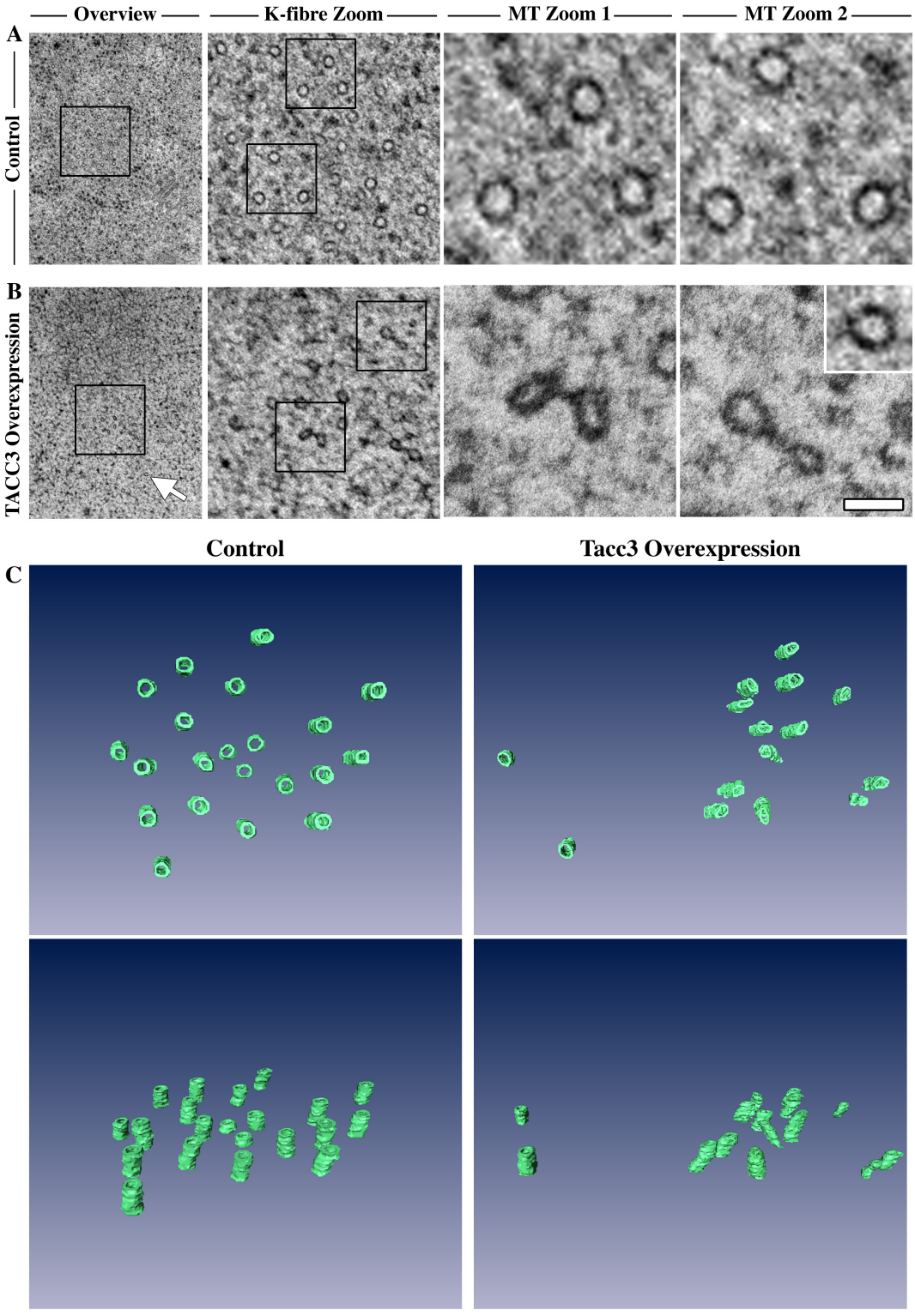
Overview
K-fibre Zoom
MT Zoom 1
MT Zoom 2
A
Control
B
TACC3 Overexpression
Control
Tacc3 Overexpression
C

Figure 5.9 – TACC3 overexpression results in disorganised and misshapen kMTs. Qualitative electron micrographs of K-fibre cross-sections from synchronised control or TACC3-overexpressing cells. Images were taken from tilt series videos. (**A**) Representative images of an orthogonal K-fibre from a control cell. Images from left to right, show progressive zooms of boxed regions of interest. The two zooms show a selection of kMTs that appear well organised. (**B**) Representative images of an orthogonal K-fibre from a cell overexpressing TACC3. Images from left to right, show progressive zooms of boxed regions. The zooms show examples of kMTs with poor organisation and atypically shaped kMTs. The white arrow in the **overview** points to a nearby ipMT, a zoom of this is shown in the top right of **MT Zoom 2**. The ipMT is identical to those from controls, i.e. it does not appear to be elliptical. **C**) Both of the K-fibre tilt series shown in **B** were converted into tomograms and rendered into 3D models. The control and TACC3 overexpressing K-fibre models are shown from both front and side perspectives.

Although some ipMTs are known to infiltrate K-fibres on a regular basis, the level of mis-orientation observed in this K-fibre is unusually high. In contrast, a control K-fibre contained kMTs that appeared well organised and all in same orientation (**Figure 5.10 A**). Finally, the third K-fibre analysed from a TACC3-overexpressing cell appeared to contain an electron-dense inter-MT mesh that was more pronounced than in controls (**Figure 5.10 B**). In addition, similarly to K-fibre two, some kMTs were present that lacked organisation (**Figure 5.10 B**). If the aberrant features observed in the cross-sections of K-fibres from cells overexpressing TACC3 were genuine, then this change in morphology should also be seen in K-fibres sectioned longitudinally to the spindle axis, this was tested. K-fibres of control cells, sectioned longitudinally, showed morphologically typical, well-organised bundles, that extended from the cell pole and terminated at kinetochores (**Figure 5.11 A 1 & 2**). At high magnification it was possible to see that individual kMTs were intact and appeared well arranged with uniform inter-MT spacing (**Figure 5.11 A 3**). In contrast, the K-fibres of cells overexpressing TACC3 were poorly organised (**Figure 5.11 B 1 & 2**). High magnification of these K-fibres revealed that a number of kMTs were, not only poorly arranged, but also, some individual MTs exhibited condensed patches at certain points along their length (**Figure 5.11 B 3-5**). It is likely that these patches of distorted MT are the same misshapen MTs observed in the orthogonal K-fibre from **Figure 5.9**, indeed the 3D model (**Figure 5.9 C**) would support this statement, as the MT distortions can be seen in both the top and side view. In addition, some K-fibres frequently 'weaved' in and out of the plane of section (**Figure 5.11 B 6**), potentially a sign of MT poor organisation or lack of tension.

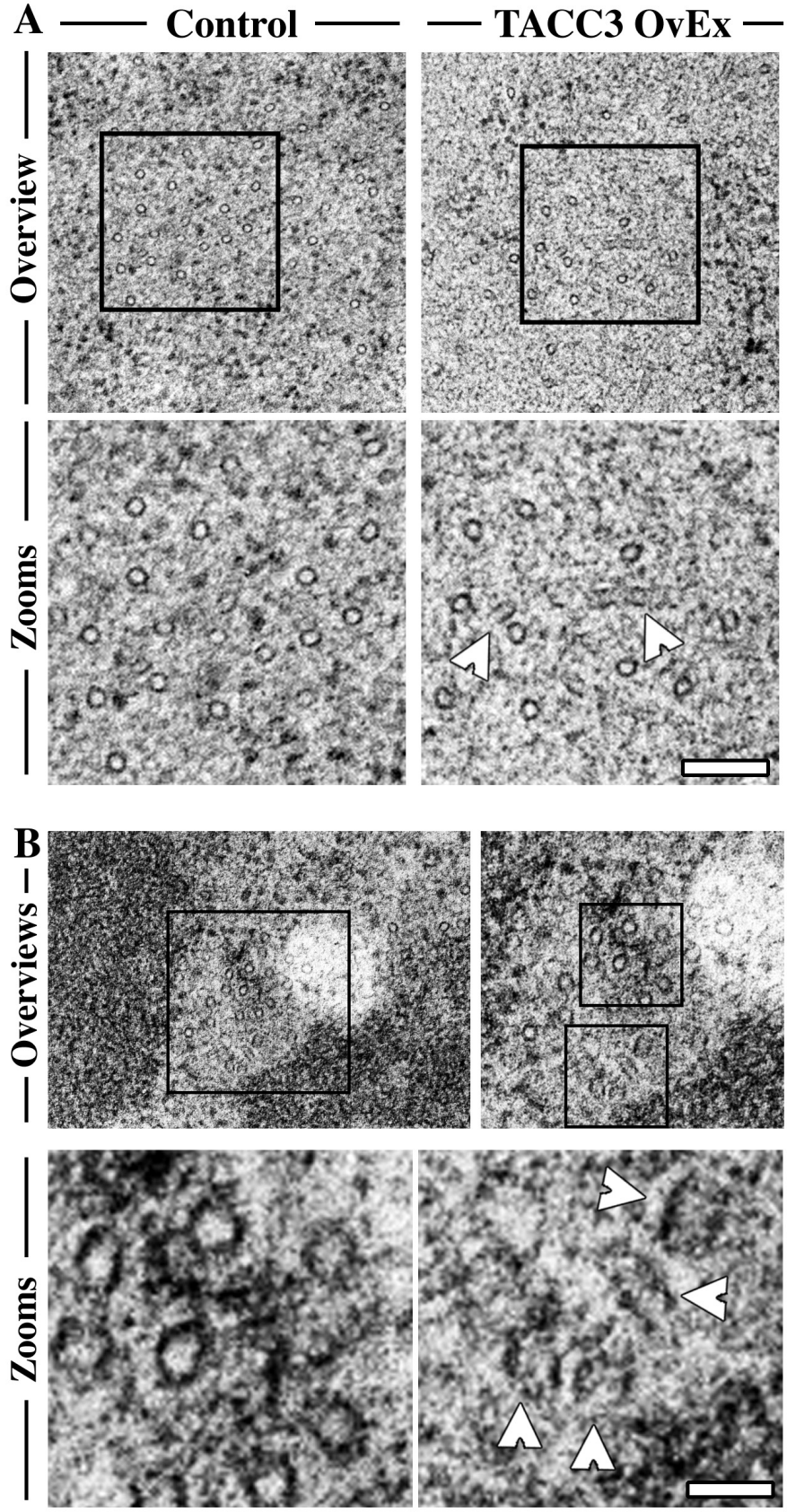
A
Control
TACC3 OvEx
Overview
Zooms
B
Overviews
Zooms

Figure 5.10 – TACC3-overexpressing K-fibres are disorganised and exhibit a dense inter-MT mesh. Electron micrographs of K-fibres orthogonally sectioned from control or TACC3-overexpressing cells. **A**) Control K-fibre showing well-organised and well-rounded kMTs and a K-fibre from TACC3-overexpressing where kMTs appear poorly organised, with several being mis-orientated (**arrow-heads**), in addition the MTs do not appear as well rounded as those from control cells. Scale bar, 100 nm. **B**) A K-fibre from a third TACC3-overexpressing cell. Higher magnifications reveal a dense inter-MT mesh making numerous points of contact with the kMTs. Poorly aligned kMTs are also present within the bundle (**arrow-heads**). Scale bar, 30 nm.

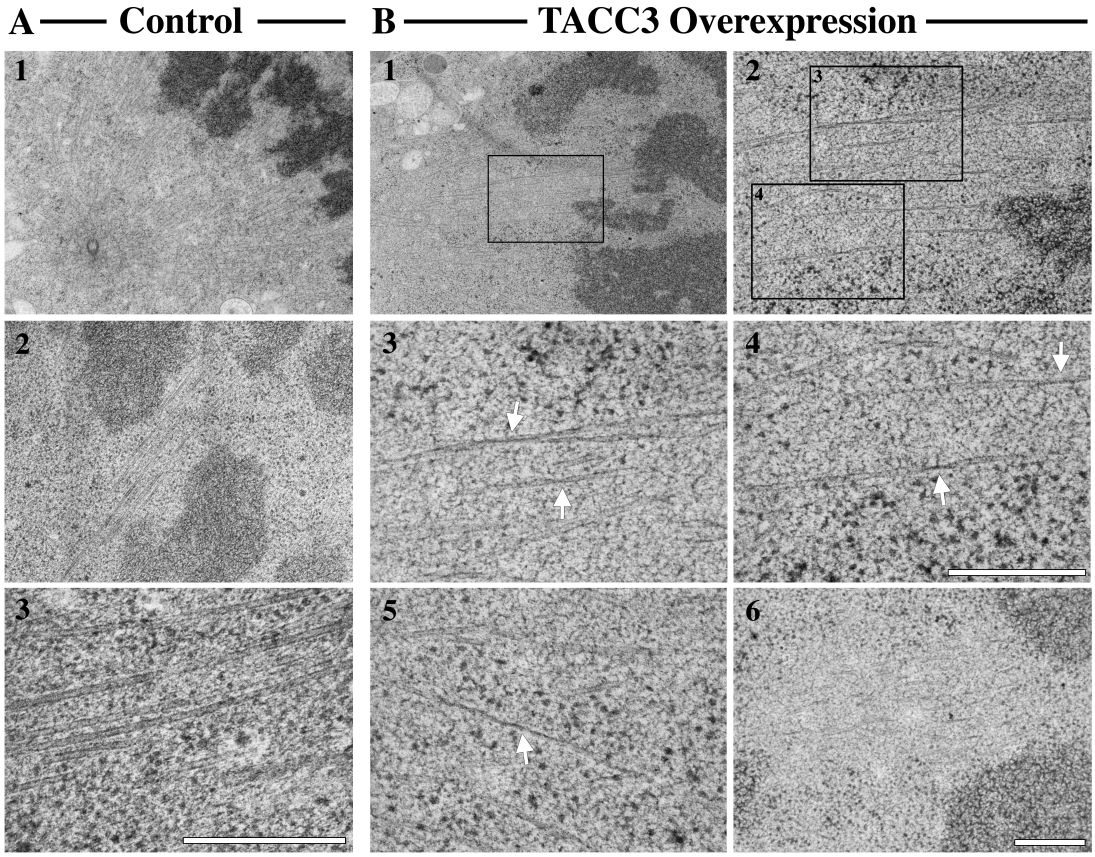

Figure 5.11 – Disorganisation of kMTs in TACC3-overexpressing cells visualised in longitudinal sections. Electron micrographs of K-fibres sectioned longitudinally from control or TACC3-overexpressing cells. **A**) Control K-fibres at low (images 1 & 2) and high (image 3) magnification. **B**) TACC3-overexpressing K-fibres. Part of a K-fibre seen in the overview (image 1) is boxed and magnified (image 2). Two kMTs of interest from image 2 are boxed and magnified in images 3 & 4. Arrows in images 3-5 point to misshapen kMTs. Image 6 shows a poorly organised K-fibre that regularly moves into and out of the plane of section. Scale bars, 400 nm (B 3-5 and A2+B6 are the same magnifications).

5.5 Discussion

The aim of this chapter was to gain a more comprehensive understanding of the fine structure of inter-kMT bridges. In doing so, this study is the first to provide evidence for a complex structure that cross-links kMTs within K-fibres of HeLa cells. We have termed this the inter-MT mesh. Once identified, an attempt was made to manipulate the mesh by altering the expression levels of TACC3. The common theme observed in cells overexpressing TACC3 was poor kMT organisation, as a consequence of mis-orientated kMTs, misshapen kMTs and an enhanced electron-dense inter-kMT mesh. This indicates that TACC3 is an integral component of the mesh.

The techniques used to study the mesh were labour intensive and technically demanding, for these reasons the analyses in this chapter were limited due to time constraints. Only two of the five batches of HPF/FS HeLa cells were analysed, leaving other samples, such as the TACC3 RNAi cells unexplored. To gain a more comprehensive insight in to the function and composition of the mesh, these samples will need to be analysed and experiments repeated. As it stands, an inter-kMT mesh has been observed in seven cells, from three separate experiments, using two different fixation conditions. The presence of this new structure is undeniable, but raises the question, why has it not been seen previously?

Although a majority of studies simply use the term ‘bridges’ it is clear that a few studies were aware of the presence of a more complex inter-kMT cross-linking structure and attempted to describe it. Hepler *et al*. are probably the closest to describing the mesh when they noted that some inter-kMT bridges appeared ‘filamentous’ and contained ‘multiple projections’ (Hepler et al., 1970). Rieder also

reported the presence of a more complex structure present in K-fibres, referring to it as ‘an ill defined electron opaque matrix’. This was observed in cold-stable PtK cells treated with tannic acid (Rieder, 1982). He suggests that this density is not just embedded within the K-fibre, but associated with the walls of the kMTs. Rieder went on to say that this matrix is part of the ‘sleeve element’, a collection of proteins that surround the MTs, which can sometimes form bridges to arms cross-link kMTs (Rieder, 1982). However, as most of the studies investigating inter-kMT bridges were completed in the 1970s and 80s their research was limited by instruments available at the time. That is, the three advanced EM techniques employed here were not available when these classic studies were carried out. It is therefore likely that the inter-kMT mesh resolved during this study is an extension of previously described bridges and its visualisation was only possible having used HPF/FS, tomographic reconstructions and 3D modeling.

The use of cryobiology, as an alternative to aldehydes, improves the resolution of intracellular structures (Landemore et al., 1996, McDonald, 2009) including MTs (Subramanian et al., 2010, O'Toole and Mueller-Reichert, 2009), whilst also reducing artifacts associated with aldehyde fixation and dehydration (Kellenberger et al., 1992). The use of tomography, quite literally adds a new dimension to ultrastructural research by allowing sub-cellular structures (Mader et al., 2010, Medalia et al., 2002) including MTs (Koning, 2010) to be visualised from all angles. Using a tomogram it is possible to render 3D models of structures of interest (Kremer et al., 1996), a technique that has immerged as an important tool in numerous areas of cell biology (McEwen and Marko, 2001) including the study of MTs (Hoeoeg et al., 2011, McIntosh et al., 2008) and even the inter-MT bridges

found in the midbody (Elad et al., 2011). The use of such techniques can now also be considered as a tool for investigating the inter-kMT mesh in K-fibers.

In TACC3 overexpressing K-fibres, misshapen kMTs were observed in both longitudinal and orthogonal sections. Given the dimensions of these distorted kMTs it is likely that they are assembled from fewer than 13 protofilaments, if this is correct, then TACC3 together with ch-TOG and clathrin, could have a role in quality control of MT assembly. An idea that is further supported by the unusually intense inter-kMT bridges observed between the most misshapen kMTs of the bundle (**Figure 5.9 B**). This is an interesting hypothesis, especially given the observation of, what appeared to be, tubulin subunits associated with the inter-kMT mesh in control cells. *In vitro* studies have shown that concentrations of MAPs can influence the number of protofilaments in MTs (Bohm et al., 1984). This can be seen in **Figure 1.3 B**, where MTs with 9 protofilaments are less circular in profile than those with 13 protofilaments. Furthermore, MTs possessing atypical protofilament numbers can also exhibit random bends about their length (Chretien et al., 1992). This could potentially explain the loss of organisation and 'weaving' of kMTs in and out of the plane of section, readily observed in TACC3 overexpressing cells and ch-TOG depleted cells and to a lesser extent, TACC3 or clathrin depleted cells (in Chapter 4). An alternative explanation is that the variation in kMT structure is caused by altered MT polymerisation and that this affects the binding potential of bridges or mesh, resulting in diminished kMT organisation. It is plausible that misshapen kMTs could contain fewer binding sites, have reduced affinity for binding or that an inter-kMT mesh just simply struggles to make contact and reinforce the misshapen MTs. Indeed, one of the K-fibres analysed, in cells overexpressing TACC3, contained morphologically typical kMTs that were inter-connected by an

unusually electron dense, inter-kMT mesh (**Figure 5.10 B**). Whilst the mesh appeared genuine, this particular K-fibre was close to termination at the kinetochore, therefore this mesh could be representing part of the Ndc80 complex, a fibrous network that has been reported to connect kMTs to the outer-kinetochore (Dong et al., 2007).

In summary, the presence of the mesh is undeniable, however its full function and composition have only been partly resolved. Further work needs to be carried out in order to reveal the other mesh components and test their role in the function of the mesh.

6 General discussion

To conclude this thesis I will briefly review the key results and how they have advanced the current knowledge of the function of inter-MT cross-linkers in K-fibres. Methods were established for the ultrastructural, multi-axis analysis of mitotic spindles in conditioned HeLa cells. These methods extend to quantification of numerous kMT and inter-MT bridge parameters as well as the correlative immunogold labelling of mitotic spindles. Using these methods it was revealed that clathrin and TACC3 were components of a TACC3/ch-TOG/clathrin complex that functions as an inter-kMT bridge in K-fibres. More over, this complex accounted for the shortest of several predicted inter-kMT bridge populations in K-fibres. Finally, the use of advanced EM techniques resolved bridging structures to be part of a larger, more complex inter-kMT cross-linking structure that we have termed an inter-kMT mesh. Some evidence was presented to show that TACC3 levels altered the mesh, suggesting that TACC3 is a mesh component and integral to its structure/function. To consider how the inter-MT mesh functions, a better perspective would be to ask *why* there is a mesh in K-fibres? Based on the results acquired during this project we think a mesh could potentially fulfill a number of roles. The depletion of clathrin led to poor kMT organisation and a loss of kMTs, in addition, the overexpression of TACC3 resulted in loss of kMT organisation and misshapen kMTs. Therefore, the mesh could provide a supportive role to limit kMT buckling, twisting and breaking, through the dissipation of forces in the spindle.

The role of the mesh can also be considered from a whole K-fibre perspective. The physical tethering of the individual kMTs would likely make the propagation of poleward forces more efficient, mediating chromosome movement

with a solid K-fibre unit, instead of through individual, small MT units, i.e. the mesh could have a role in the pulling and pushing of chromosomes and maintaining kMT tension. This is an interesting approach given that a lack of kMT tension is associated with MT deploymerisation (Civelekoglu-Scholey and Scholey, 2010). More over, kMTs that are tethered together could also promote the even dispersion of poleward forces, this would avoid extra, uneven force being generated on one side of the K-fibre and therefore the kinetochore. This could explain the problems with chromosome congression following the depletion of TACC3 or clathrin (Royle et al., 2005, Lin et al., 2010)

Clathrin depletion induces a loss of kMTs, this could suggest the mesh functions to reduce MT catastrophe, an event that could be mediated by ch-TOG, since it has previously been shown to function in MT growth and shrinkage (Brouhard et al., 2008). This is even more interesting given that, in control cells, tubulin subunits were regularly observed associated with the mesh. An alternative function could be more specifically related to inter-MT spacing. It has been shown that certain MAPs require different amounts of inter-MT spacing (Chen et al., 1992), therefore another function of the mesh could be to create sufficient room between MTs to allow the translocation of MAPs and motors along the MT length (Amos and Schlieper, 2005, Chen et al., 1992). The data thus far implies that the role of the mesh in kMT organisation, spacing and stability is more convoluted than simply 'bridges hold kMTs together', rather, there is a dynamic equilibrium between pulling and pushing forces to provide these roles. To fully understand the function of the mesh, more work is required to reveal its entire composition.

Finally, all three members of the TACC3/ch-TOG/clathrin complex have been associated with a number of cancers. Therefore the inter-kMT mesh and its

function could be medically relevant. Overexpression of ch-TOG has been observed in both hepatic and colonic tumours (Charrasse et al., 1995), whereas TACC3 is overexpressed in non-small cell lung cancer (Jung et al., 2006). The depletion of TACC3 has been shown to sensitise cells to Paclitaxel, a mitotic inhibitor used in chemotherapy (Schmidt et al., 2010). Furthermore, TACC3 promotes cell survival in cells with centrosome supernumerary, an event that usually triggers apoptosis, but in this situation supports tumourogenesis (Fielding et al., 2011). In addition, gene-fusions of CHC are implicated in the development of anaplastic large-cell lymphoma and renal adenocarcinoma (Pulford et al., 2004, Argani et al., 2003). More research is required to understand if the mesh is directly implicated in any of the occurrences mentioned above.

In summary, the material that holds K-fibres together was first observed over 40 years ago, but has never been fully characterised. As a result of this project we have provided novel insights regarding the; topology, composition and function of inter-MT cross-linkers in human K-fibres.

7 Appendices

7.1 Oligonucleotides for TACC3 and ch-TOG shRNA

A TACC3

Target sequence: 5'- AAGTTACCGGAAGATCGTCTG -3'

Oligo 1 sense

5' GATCCCCgttaccggaagatcgtctgTTCAAGAGAcagacgatcttccggtaacTTTTTGGAAA 3'

Oligo 2 anti-sense (reversed)

5' AGCTTTTCCAAAAAgttaccggaagatcgtctgTCTCTTGAAcagacgatcttccggtaacGGG 3'

(Bgl II)

5' GATCCCCgttaccggaagatcgtctgTTCAAGAGAcagacgatcttccggtaacTTTTTGGAAA 3'

3' GGGcaatggccttctagcagacAAGTTCTCTgtctgctagaaggccattgAAAAACCTTTTCGA 5'

(Hind III)

B chTOG

Target sequence: 5'- AATGCTCCACAGCAAACTCTC -3'

Oligo 1 sense

5' GATCCCCtgctccacagcaaactctcTTCAAGAGAgagagtttgctgtggagcaTTTTTGGAAA 3'

Oligo 2 anti-sense (reversed)

5' AGCTTTTCCAAAAAtgctccacagcaaactctcTCTCTTGAAgagagtttgctgtggagcaGGG 3'

(Bgl II)

5' GATCCCCtgctccacagcaaactctcTTCAAGAGAgagagtttgctgtggagcaTTTTTGGAAA 3'

3' GGGacgaggtgtcgtttgagagAAGTTCTCTctctcaaacgacacctcgtAAAAACCTTTTCGA 5'

(Hind III)

Figure 7.1 – RNAi sequences and shRNA designs for entry into pBrain vector system. RNAi target sequences for TACC3 (**A**) and chTOG (**B**) were taken from published work (Gergely et al., 2003). The RNAi sequences (black-underlined) were incorporated into shRNA oligonucleotides for ligation into the pBrain system of vectors. Both the 5' and 3' oligo nucleotides were designed 100% complementary, apart from the 'sticky ends' which were left as overhangs for direct ligation into vector (green). The BglII site was designed to contain a point mutation (blue) that, once ligated into the vector, would be abolished. The hairpin is shown in red.

7.2 The role of KIF4 in midbody formation

As part of a collaboration that I initiated with Professor Bill Earnshaw (Edinburgh University) an ultrastructural analysis of DT40 cells was carried out. PRC1 is an essential midbody protein, responsible for the organisation of midzone/midbody MTs. The depletion of PRC1 or its binding partner KIF4, as shown by light microscopy, results in a loss of midzone integrity and loss of a docking site for essential midbody proteins required for abscission. TEM analysis of PRC1 depleted cells revealed a loss of the electron-dense midbody. The ultrastructural phenotype of KIF4 depleted midbodies was previously unknown. Using a DT40 cell line, capable of doxycycline inducible KIF4 depletion, I was able to use CLEM to reveal that cells lacking KIF4 were unable to assemble an electron-dense midbody, in addition, poor MT organisation was also observed (**Figure 7.2**). In contrast, normal cytokinesis occurred in control cells, which were able to assemble a typical electron dense-midbody (**Figure 7.2 – far left**). This work is currently being written up for publication.

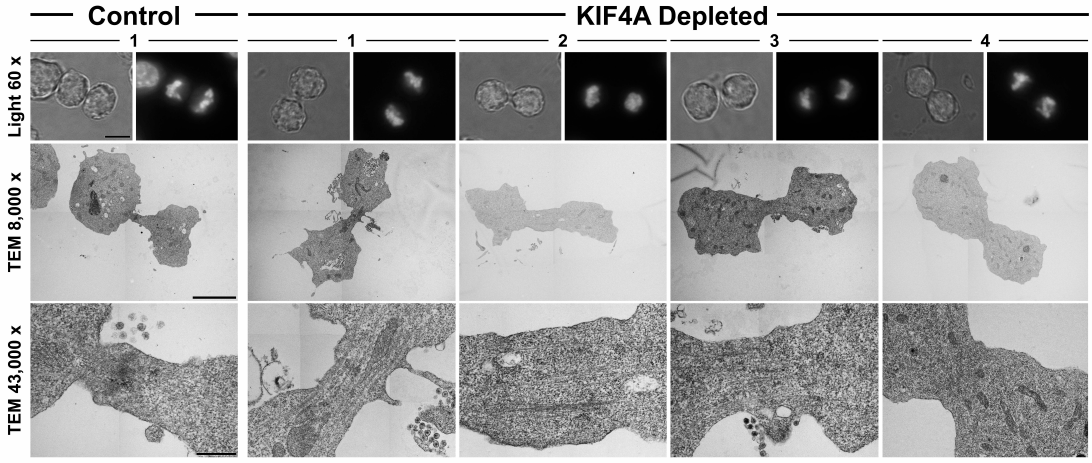

Figure 7.2 – Depletion of KIF4 prevents formation of the midbody. Mitotic DT40 cells were depleted of KIF4 and processed for correlative light electron microscopy. Cells in cytokinesis were identified using DAPI and white light (**top row**) before TEM processing. In a control cell, the midbody microtubules appeared well organised, positioned either side of a well assembled, electron-dense, midbody (**far left column**). Cells depleted of KIF4 often exhibited poorly organised MTs and all of the cells failed to assemble an electron-dense midbody. Scale bar; 10 µm (top & middle rows), 500 nm (bottom row).

7.3 Inhibition of Aurora A kinase destabilises kinetochore fibers

This study revealed a TACC3/ch-TOG/clathrin complex to be a short population of inter-MT bridges in K-fibres. The association of TACC3 with spindle microtubules is mediated by Aurora A kinase, most likely at serine558. If the bridge complex truly were regulated by this kinase, then its inhibition would presumably result in a loss of bridges by EM. This was tested using MLN8237, a specific Aurora A kinase inhibitor. The full results can be seen in the publication shown in Chapter **7.4.2**. I contributed to this publication by testing the effects of MLN8237 on K-fibre stability in HeLa cells, using fluorescence microscopy. Treatment with MLN resulted in problems with chromosome congression and misaligned chromosomes. Following a cold-treatment it became clear that these defects were probably as a consequence of a decrease in K-fibre stability, demonstrated by unattached 'orphan' kinetochores (**Figure 7.3**). In contrast the K-fibres of cold-treated control cells appeared to maintain stable attachments. This phenotype is similar to that of clathrin and TACC3 depleted cells.

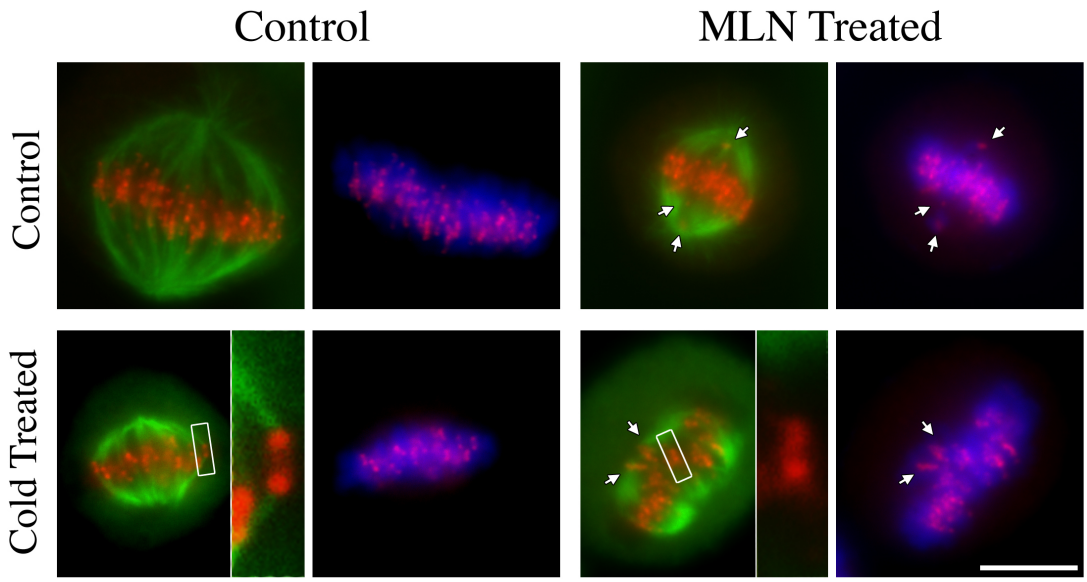

Figure 7.3 - Inhibition of Aurora A kinase destabilises kinetochore fibers. HeLa cells near metaphase were treated with MLN8237 (0.3 μm, 40 min) and either fixed or before fixation, incubated in ice-cold DMEM for 6 min to selectively depolymerise all non-stable MTs. Control cells were prepared in parallel using a vehicle to replace MLN. Cells were labelled with anti-β-tubulin (green), anti-CENP-B (red) and DAPI (blue). White arrows mark 'orphan' chromosomes. Scale bar, 10 μm.

7.4 Publications

BOOTH, D. G., HOOD, F. E., PRIOR, I. A. & ROYLE, S. J. 2011. A TACC3/ch-TOG/clathrin complex stabilises kinetochore fibres by inter-microtubule bridging. *EMBO J,* 30**,** 906-19.

CHEESEMAN, L.P., BOOTH, D.G., HOOD, F.E., PRIOR, I.A. & ROYLE, S.J. (2011) Aurora A kinase activity is required for localisation of TACC3/ch-TOG/clathrin inter-microtubule bridges. Commun. Integr. Biol., 4: 409-12.

8 Bibliography

ALLEN, C. & BORISY, G. G. 1974. Structural Polarity and Directional Growth of Microtubules of Chlamydomonas Flagella. *Journal of Molecular Biology,* 90**,** 381-&.

ALLEN, R. D. 1975. Evidence for Firm Linkages Between Microtubules and Membran-Bounded Vesicles. *Journal of Cell Biology,* 64**,** 497-503.

AMOS, L. A. & SCHLIEPER, D. 2005. Microtubules and maps. *Adv Protein Chem,* 71**,** 257-98.

ARGANI, P., LUI, M. Y., COUTURIER, J., BOUVIER, R., FOURNET, J. C. & LADANYI, M. 2003. A novel CLTC-TFE3 gene fusion in pediatric renal adenocarcinoma with t(X;17)(p11.2;q23). *Oncogene,* 22**,** 5374-8.

AULT, J. G. & RIEDER, C. L. 1994. Centrosome and Kinetochore Movement During Mitosis. *Current Opinion in Cell Biology,* 6**,** 41-49.

BAJER, A. S. 1973. Interaction of microtubules and the mechanism of chromosome movement (zipper hypothesis). 1. General principle. *Cytobios,* 8**,** 139-60.

BALDIN, V., LUKAS, J., MARCOTE, M. J., PAGANO, M. & DRAETTA, G. 1993. Cyclin D1 is a Nuclear-Protein Required For Cell-cycle Progression. *Genes & Development,* 7**,** 812-821.

BANANIS, E., NATH, S., GORDON, K., SATIR, P., STOCKERT, R. J., MURRAY, J. W. & WOLKOFF, A. W. 2004. Microtubule-dependent movement of late endocytic vesicles in vitro: Requirements for dynein and kinesin. *Molecular Biology of the Cell,* 15**,** 3688-3697.

BARTON, R. 1969. Investigation of negatively stained plant flagellar microtubules by optical diffraction. *J Cell Biol,* 41**,** 637-41.

BASTMEYER, M. & FUGE, H. 1986. The Distribution of Intermicrotubular Bridges in Meiotic Spindles of the Crane Fly. *Chromosoma,* 94**,** 419-424.

BHISEY, A. N. & FREED, J. J. 1971. Cross-bridges on Microtubules of Cooled Interphase HeLa Cells. *Journal of Cell Biology,* 50**,** 557-&.

BLIXT, M. K. & ROYLE, S. J. 2011. Clathrin heavy chain gene fusions expressed in human cancers: analysis of cellular functions. *Traffic,* 12**,** 754-61.

BLOOM, K. & JOGLEKAR, A. 2010. Towards building a chromosome segregation machine. *Nature,* 463**,** 446-456.

BOHM, K. J., VATER, W., FENSKE, H. & UNGER, E. 1984. Effect of Microtubule-Associated Proteins on the Protofilament Number of Microtubules Assembled InVitro. *Biochimica Et Biophysica Acta,* 800**,** 119-126.

BONE, Q. & RYAN, K. P. 1972. Osmolarity of osmium tetroxide and glutaraldehyde fixatives. *Histochem J,* 4**,** 331-47.

BOOTH, D. G., HOOD, F. E., PRIOR, I. A. & ROYLE, S. J. 2011. A TACC3/ch-TOG/clathrin complex stabilises kinetochore fibres by inter-microtubule bridging. *EMBO J,* 30**,** 906-19.

BOUCROT, E. & KIRCHHAUSEN, T. 2007. Endosomal recycling controls plasma membrane area during mitosis. *Proceedings of the National Academy of Sciences of the United States of America,* 104**,** 7939-7944.

BRINKLEY, B. R. & CARTWRIGHT, J., JR. 1971. Ultrastructural analysis of mitotic spindle elongation in mammalian cells in vitro. Direct microtubule counts. *J Cell Biol,* 50**,** 416-31.

BRODSKY, F. M., CHEN, C. Y., KNUEHL, C., TOWLER, M. C. & WAKEHAM, D. E. 2001. Biological basket weaving: formation and function of clathrin-coated vesicles. *Annu Rev Cell Dev Biol,* 17**,** 517-68.

BROUHARD, G. J., STEAR, J. H., NOETZEL, T. L., AL-BASSAM, J., KINOSHITA, K., HARRISON, S. C., HOWARD, J. & HYMAN, A. A. 2008. XMAP215 is a processive microtubule polymerase. *Cell,* 132**,** 79-88.

BUCHKOVICH, K., DUFFY, L. A. & HARLOW, E. 1989. The Retinoblastoma Protein is Phosphorylated During Specific Phases of the Cell-cycle. *Cell,* 58**,** 1097-1105.

BURNS, R. G. 1991. Alpha-Tubulin, Beta-Tubulin, and Gamma-Tubulins - Sequence Comparisons and Structural Constraints. *Cell Motility and the Cytoskeleton,* 20**,** 181-189.

CAI, S., WEAVER, L. N., EMS-MCCLUNG, S. C. & WALCZAK, C. E. 2009. Kinesin-14 Family Proteins HSET/XCTK2 Control Spindle Length by Cross-Linking and Sliding Microtubules. *Molecular Biology of the Cell,* 20**,** 1348-1359.

CARLTON, J. G. & MARTIN-SERRANO, J. 2007. Parallels between cytokinesis and retroviral budding: A role for the ESCRT machinery. *Science,* 316**,** 1908-1912.

CARMENA, M., RIPARBELLI, M. G., MINESTRINI, G., TAVARES, A. M., ADAMS, R., CALLAINI, G. & GLOVER, D. M. 1998. Drosophila polo kinase is required for cytokinesis. *J Cell Biol,* 143**,** 659-71.

CHAN, J., JENSEN, C. G., JENSEN, L. C. W., BUSH, M. & LLOYD, C. W. 1999. The 65-kDa carrot microtubule-associated protein forms regularly arranged filamentous cross-bridges between microtubules. *Proceedings of the National Academy of Sciences of the United States of America,* 96**,** 14931-14936.

CHARRASSE, S., MAZEL, M., TAVIAUX, S., BERTA, P., CHOW, T. & LARROQUE, C. 1995. Characterization of the cDNA and pattern of expression of a new gene over-expressed in human hepatomas and colonic tumors. *Eur J Biochem,* 234**,** 406-13.

CHEN, J., KANAI, Y., COWAN, N. J. & HIROKAWA, N. 1992. Projection domains of MAP2 and tau determine spacings between microtubules in dendrites and axons. *Nature,* 360**,** 674-7.

CHERRY, L. M. & JOHNSTON, D. A. 1987. Size variation in kinetochores of human chromosomes. *Hum Genet,* 75**,** 155-8.

CHRETIEN, D., METOZ, F., VERDE, F., KARSENTI, E. & WADE, R. H. 1992. Lattice-Defects in Microtubules - Protofilament Numbers Vary Within Individual Microtubules. *Journal of Cell Biology,* 117**,** 1031-1040.

CIVELEKOGLU-SCHOLEY, G. & SCHOLEY, J. M. 2010. Mitotic force generators and chromosome segregation. *Cellular and Molecular Life Sciences,* 67**,** 2231-2250.

COMPTON, D. A. 2007. Chromosome orientation. *Journal of Cell Biology,* 179**,** 178-181.

COOKE, C. A., HECK, M. M. & EARNSHAW, W. C. 1987. The inner centromere protein (INCENP) antigens: movement from inner centromere to midbody during mitosis. *J Cell Biol,* 105**,** 2053-67.

CYTRYNBAUM, E. N., SCHOLEY, J. M. & MOGILNER, A. 2003. A force balance model of early spindle pole separation in Drosophila embryos. *Biophysical Journal,* 84**,** 757-769.

DESAI, A. & MITCHISON, T. J. 1997. Microtubule polymerization dynamics. *Annual Review of Cell and Developmental Biology,* 13**,** 83-117.

DING, R., MCDONALD, K. L. & MCINTOSH, J. R. 1993. Three-dimensional reconstruction and analysis of mitotic spindles from the yeast, Schizosaccharomyces pombe. *J Cell Biol,* 120**,** 141-51.

DONG, Y., VANDEN BELDT, K. J., MENG, X., KHODJAKOV, A. & MCEWEN, B. F. 2007. The outer plate in vertebrate kinetochores is a flexible network with multiple microtubule interactions. *Nature Cell Biology,* 9**,** 516-22.

EDELING, M. A., SMITH, C. & OWEN, D. 2006. Life of a clathrin coat: insights from clathrin and AP structures. *Nature Reviews Molecular Cell Biology,* 7**,** 32-44.

ELAD, N., ABRAMOVITCH, S., SABANAY, H. & MEDALIA, O. 2011. Microtubule organization in the final stages of cytokinesis as revealed by cryo-electron tomography. *Journal of Cell Science,* 124**,** 207-215.

ENDOW, S. A. & KOMMA, D. J. 1996. Centrosome and spindle function of the Drosophila Ncd microtubule motor visualized in live embryos using Ncd-GFP fusion proteins. *J Cell Sci,* 109 (Pt 10)**,** 2429-42.

ENDOW, S. A. & KOMMA, D. J. 1997. Spindle dynamics during meiosis in Drosophila oocytes. *J Cell Biol,* 137**,** 1321-36.

FIELD, C., LI, R. & OEGEMA, K. 1999. Cytokinesis in eukaryotes: a mechanistic comparison. *Current Opinion in Cell Biology,* 11**,** 68-80.

FIELDING, A. B., LIM, S., MONTGOMERY, K., DOBREVA, I. & DEDHAR, S. 2011. A critical role of integrin-linked kinase, ch-TOG and TACC3 in centrosome clustering in cancer cells. *Oncogene,* 30**,** 521-34.

FOTIN, A., CHENG, Y., SLIZ, P., GRIGORIEFF, N., HARRISON, S. C., KIRCHHAUSEN, T. & WALZ, T. 2004. Molecular model for a complete clathrin lattice from electron cryomicroscopy. *Nature,* 432**,** 573-9.

FRANKE, W. W., KARTENBE.J, ZENTGRAF, H., SCHEER, U. & FALK, H. 1971. Membrane-to-Membrane Cross-Bridges - Means to Orientation and Interaction of Membrane Faces. *Journal of Cell Biology,* 51**,** 881-&.

FRIEDMAN, M. H. 1971. Arm-Bearing Microtubules Associated With An Unusual Desmosome-Like Junction. *Journal of Cell Biology,* 49**,** 916-&.

FU, W., TAO, W., ZHENG, P., FU, J., BIAN, M., JIANG, Q., CLARKE, P. R. & ZHANG, C. 2010. Clathrin recruits phosphorylated TACC3 to spindle poles for bipolar spindle assembly and chromosome alignment. *J Cell Sci,* 123**,** 3645-51.

GERGELY, F., DRAVIAM, V. M. & RAFF, J. W. 2003. The ch-TOG/XMAP215 protein is essential for spindle pole organization in human somatic cells. *Genes & Development,* 17**,** 336-341.

GLOTZER, M. 1997a. Cytokinesis. *Curr Biol,* 7**,** R274-6.

GLOTZER, M. 1997b. The mechanism and control of cytokinesis. *Curr Opin Cell Biol,* 9**,** 815-23.

GRUENBERG, J., GRIFFITHS, G. & HOWELL, K. E. 1989. CHARACTERIZATION OF THE EARLY ENDOSOME AND PUTATIVE ENDOCYTIC CARRIER VESICLES INVIVO AND WITH AN ASSAY OF VESICLE FUSION INVITRO. *Journal of Cell Biology,* 108**,** 1301-1316.

HARADA, A., TENG, J., TAKEI, Y., OGUCHI, K. & HIROKAWA, N. 2002. MAP2 is required for dendrite elongation, PKA anchoring in dendrites, and proper PKA signal transduction. *J Cell Biol,* 158**,** 541-9.

HAYS, T. S. & SALMON, E. D. 1990. Poleward force at the kinetochore in metaphase depends on the number of kinetochore microtubules. *J Cell Biol,* 110**,** 391-404.

HEALD, R. & NOGALES, E. 2002. Microtubule dynamics. *Journal of Cell Science,* 115**,** 3-4.

HEGELEHARTUNG, C., PIEGSA, K. & FISCHER, B. 1989. Effect of Osmolarity of the Fixative on the Ultrastructure of Preimplantation Rabbit Embryos. *Acta Anatomica,* 136**,** 79-88.

HEPLER, P. K., MCINTOSH, J. R. & CLELAND, S. 1970. Intermicrotubule Bridges in Mitotic Spindle Apparatus. *Journal of Cell Biology,* 45**,** 438-&.

HEUSER, J. 1980. 3-Dimensional Visualization of Coated Vesicle Formation in Fibroblasts. *Journal of Cell Biology,* 84**,** 560-583.

HEUSER, J. 1981. Quick-Freeze, Deep Etch, Preparation of Samples for 3-D Electron Microscopy. *Trends in Biochemical Sciences,* 6**,** 64-68.

HEUSER, J. & KIRCHHAUSEN, T. 1985. Deep-etch views of clathrin assemblies. *J Ultrastruct Res,* 92**,** 1-27.

HEUSER, J. E. 2011. The origins and evolution of freeze-etch electron microscopy. *Journal of Electron Microscopy,* 60**,** S3-S29.

HEUSER, J. E. & KEEN, J. 1988. Deep-Etch Visualization of Proteins Involved in Clathrin Assembly. *Journal of Cell Biology,* 107**,** 877-886.

HIRANO, T. 2005. Condensins: Organizing and segregating the genome. *Current Biology,* 15**,** R265-R275.

HIROKAWA, N. 1994. Microtubule organization and dynamics dependent on microtubule-associated proteins. *Curr Opin Cell Biol,* 6**,** 74-81.

HOEOEG, J. L., HUISMAN, S. M., SEBOE-LEMKE, Z., SANDBLAD, L., MCINTOSH, J. R., ANTONY, C. & BRUNNER, D. 2011. Electron tomography reveals a flared morphology on growing microtubule ends. *Journal of Cell Science,* 124**,** 693-698.

HOLZENSPIES, J. J., ROELEN, B. A. J., COLENBRANDER, B., ROMIJN, R. A. P., HEMRIKA, W., STOORVOGEL, W. & VAN HAEFTEN, T. 2010. Clathrin is essential for meiotic spindle function in oocytes. *Reproduction,* 140**,** 223-233.

HOOD, F. E. & ROYLE, S. J. 2009. Functional equivalence of the clathrin heavy chains CHC17 and CHC22 in endocytosis and mitosis. *J Cell Sci,* 122**,** 2185-90.

HOOD, F. E. & ROYLE, S. J. 2011. Pulling it together: The mitotic function of TACC3. *Bioarchitecture,* 1**,** 105-109.

HOWARD, J. & HYMAN, A. A. 2003. Dynamics and mechanics of the microtubule plus end. *Nature,* 422**,** 753-758.

HU, C. K., COUGHLIN, M., FIELD, C. M. & MITCHISON, T. J. 2011. KIF4 regulates midzone length during cytokinesis. *Curr Biol,* 21**,** 815-24.

HUBNER, N. C., BIRD, A. W., COX, J., SPLETTSTOESSER, B., BANDILLA, P., POSER, I., HYMAN, A. & MANN, M. 2010. Quantitative proteomics combined with BAC TransgeneOmics reveals in vivo protein interactions. *J Cell Biol,* 189**,** 739-54.

IMHOF, B. A., MARTI, U., BOLLER, K., FRANK, H. & BIRCHMEIER, W. 1983. Association between coated vesicles and microtubules. *Exp Cell Res,* 145**,** 199-207.

JENSEN, C. G., AIST, J. R., BAYLES, C. J., BOLLARD, S. M. & JENSEN, L. C. W. 1991. Ultrastructural Basis of Mitosis in the Fungus Nectria-Haematococca (Sexual Stage of Fusarium-Solani) .3. Intermicrotubule Bridges. *Protoplasma,* 161**,** 137-149.

JIANG, W., JIMENEZ, G., WELLS, N. J., HOPE, T. J., WAHL, G. M., HUNTER, T. & FUKUNAGA, R. 1998. PRC1: a human mitotic spindle-associated CDK substrate protein required for cytokinesis. *Molecular Cell,* 2**,** 877-85.

JIN, A. J. & NOSSAL, R. 2000. Rigidity of triskelion arms and clathrin nets. *Biophysical Journal,* 78**,** 1183-1194.

JORDAN, M. A. & WILSON, L. 2004. Microtubules as a target for anticancer drugs. *Nat Rev Cancer,* 4**,** 253-265.

JUNG, C. K., JUNG, J. H., PARK, G. S., LEE, A., KANG, C. S. & LEE, K. Y. 2006. Expression of transforming acidic coiled-coil containing protein 3 is a novel independent prognostic marker in non-small cell lung cancer. *Pathol Int,* 56**,** 503-9.

KELLENBERGER, E., JOHANSEN, R., MAEDER, M., BOHRMANN, B., STAUFFER, E. & VILLIGER, W. 1992. Artefacts and morphological changes during chemical fixation. *J Microsc,* 168**,** 181-201.

KIM, H., BINDER, L. I. & ROSENBAUM, J. L. 1979. The periodic association of MAP2 with brain microtubules in vitro. *J Cell Biol,* 80**,** 266-76.

KING, R. W., DESHAIES, R. J., PETERS, J. M. & KIRSCHNER, M. W. 1996. How proteolysis drives the cell cycle. *Science,* 274**,** 1652-1659.

KINOSHITA, K., NOETZEL, T. L., PELLETIER, L., MECHTLER, K., DRECHSEL, D. N., SCHWAGER, A., LEE, M., RAFF, J. W. & HYMAN, A. A. 2005. Aurora A phosphorylation of TACC3/maskin is required for centrosome-dependent microtubule assembly in mitosis. *J Cell Biol,* 170**,** 1047-55.

KIRCHHAUSEN, T. & HARRISON, S. C. 1981. Protein organization in clathrin trimers. *Cell,* 23**,** 755-61.

KOFFA, M. D., CASANOVA, C. M., SANTARELLA, R., KOCHER, T., WILM, M. & MATTAJ, I. W. 2006. HURP is part of a Ran-dependent complex involved in spindle formation. *Curr Biol,* 16**,** 743-54.

KONING, R. I. 2010. Cryo-electron tomography of cellular microtubules. *Methods Cell Biol,* 97**,** 455-73.

KOSHLAND, D. & STRUNNIKOV, A. 1996. Mitotic chromosome condensation. *Annu Rev Cell Dev Biol,* 12**,** 305-33.

KREMER, J. R., MASTRONARDE, D. N. & MCINTOSH, J. R. 1996. Computer visualization of three-dimensional image data using IMOD. *Journal of Structural Biology,* 116**,** 71-76.

KUNDA, P. & BAUM, B. 2009. The actin cytoskeleton in spindle assembly and positioning. *Trends in Cell Biology,* 19**,** 174-179.

KURASAWA, Y., EARNSHAW, W. C., MOCHIZUKI, Y., DOHMAE, N. & TODOKORO, K. 2004. Essential roles of KIF4 and its binding partner PRC1 in organized central spindle midzone formation. *Embo Journal,* 23**,** 3237-3248.

LAEMMLI, U. K. 1970. Cleavage of structural proteins during the assembly of the head of bacteriophage T4. *Nature,* 227**,** 680-5.

LAMOND, A. I. & EARNSHAW, W. C. 1998. Structure and function in the nucleus. *Science,* 280**,** 547-553.

LANDEMORE, G., QUILLEC, M. & IZARD, J. 1996. Ultrastructure of Kurloff body proteoglycans after high pressure freezing, cryosubstitution and postembedding staining with cuprolinic blue. *Glycobiology,* 6**,** 817-22.

LARIJANI, B. & POCCIA, D. L. 2009. Nuclear Envelope Formation: Mind the Gaps. *Annual Review of Biophysics,* 38**,** 107-124.

LIN, C. H., HU, C. K. & SHIH, H. M. 2010. Clathrin heavy chain mediates TACC3 targeting to mitotic spindles to ensure spindle stability. *J Cell Biol,* 189**,** 1097-105.

LOQMAN, M. Y., BUSH, P. G., FARQUHARSON, C. & HALL, A. C. 2010. A cell shrinkage artefact in growth plate chondrocytes with common fixative solutions: importance of fixative osmolarity for maintaining morphology. *Eur Cell Mater,* 19**,** 214-27.

MACK, G. J. & COMPTON, D. A. 2001. Analysis of mitotic microtubule-associated proteins using mass spectrometry identifies astrin, a spindle-associated protein. *Proc Natl Acad Sci U S A,* 98**,** 14434-9.

MADER, A., ELAD, N. & MEDALIA, O. 2010. Cryoelectron tomography of eukaryotic cells. *Methods Enzymol,* 483**,** 245-65.

MAHADEVAN, L. & MITCHISON, T. J. 2005. Cell biology: powerful curves. *Nature,* 435**,** 895-7.

MAIATO, H., HERGERT, P. J., MOUTINHO-PEREIRA, S., DONG, Y., VANDENBELDT, K. J., RIEDER, C. L. & MCEWEN, B. F. 2006. The ultrastructure of the kinetochore and kinetochore fiber in Drosophila somatic cells. *Chromosoma,* 115**,** 469-80.

MANDELKOW, E. & MANDELKOW, E. M. 1995. Microtubules and microtubule-associated proteins. *Curr Opin Cell Biol,* 7**,** 72-81.

MANNING, A. L. & COMPTON, D. A. 2008. Structural and regulatory roles of nonmotor spindle proteins. *Current Opinion in Cell Biology,* 20**,** 101-106.

MARKUS, S. M. & LEE, W. L. 2011. Regulated Offloading of Cytoplasmic Dynein from Microtubule Plus Ends to the Cortex. *Developmental Cell,* 20**,** 639-651.

MARO, B., JOHNSON, M. H., PICKERING, S. J. & LOUVARD, D. 1985. Changes in the distribution of membranous organelles during mouse early development. *J Embryol Exp Morphol,* 90**,** 287-309.

MARTIN, M. A., OSMANI, S. A. & OAKLEY, B. R. 1997. The role of gamma-tubulin in mitotic spindle formation and cell cycle progression in Aspergillus nidulans. *Journal of Cell Science,* 110**,** 623-633.

MASTRONARDE, D. N. 1997. Dual-axis tomography: an approach with alignment methods that preserve resolution. *Journal of Structural Biology,* 120**,** 343-52.

MASTRONARDE, D. N., MCDONALD, K. L., DING, R. & MCINTOSH, J. R. 1993. Interpolar Spindle Microtubules in Ptk Cells. *Journal of Cell Biology,* 123**,** 1475-1489.

MATHIEU, O., CLAASSEN, H. & WEIBEL, E. R. 1978. Differential effect of glutaraldehyde and buffer osmolarity on cell dimensions: a study on lung tissue. *J Ultrastruct Res,* 63**,** 20-34.

MATUS, A. 1994. Stiff microtubules and neuronal morphology. *Trends Neurosci,* 17**,** 19-22.

MCDONALD, K. L. 2009. A review of high-pressure freezing preparation techniques for correlative light and electron microscopy of the same cells and tissues. *J Microsc,* 235**,** 273-81.

MCDONALD, K. L., OTOOLE, E. T., MASTRONARDE, D. N. & MCINTOSH, J. R. 1992. Kinetochore Microtubules in Ptk Cells. *Journal of Cell Biology,* 118**,** 369-383.

MCEWEN, B. F., DING, Y. & HEAGLE, A. B. 1998. Relevance of kinetochore size and microtubule-binding capacity for stable chromosome attachment during mitosis in PtK1 cells. *Chromosome Res,* 6**,** 123-32.

MCEWEN, B. F. & MARKO, M. 2001. The emergence of electron tomography as an important tool for investigating cellular ultrastructure. *Journal of Histochemistry & Cytochemistry,* 49**,** 553-64.

MCINTOSH, J. R., CANDE, Z., SYNDER, J. & VANDERSLICE, K. 1975. Studies on Mechanism of Mitosis. *Annals of the New York Academy of Sciences,* 253**,** 407-427.

MCINTOSH, J. R., GRISHCHUK, E. L., MORPHEW, M. K., EFREMOV, A. K., ZHUDENKOV, K., VOLKOV, V. A., CHEESEMAN, I. M., DESAI, A., MASTRONARDE, D. N. & ATAULLAKHANOV, F. I. 2008. Fibrils Connect Microtubule Tips with Kinetochores: A Mechanism to Couple Tubulin Dynamics to Chromosome Motion. *Cell,* 135**,** 322-333.

MCINTOSH, J. R. & LANDIS, S. C. 1971. Distribution of Spindle Microtubules during Mitosis in Cultured Human Cells. *Journal of Cell Biology,* 49**,** 468-&.

MCINTOSH, J. R., SISKEN, J. E. & CHU, L. K. 1979. Structural Studies on Mitotic Spindles Isolated from Cultured Human Cells. *Journal of Ultrastructure Research,* 66**,** 40-52.

MCNIVEN, M. A. & THOMPSON, H. M. 2006. Vesicle formation at the plasma membrane and trans-Golgi network: The same but different. *Science,* 313**,** 1591-1594.

MEDALIA, O., WEBER, I., FRANGAKIS, A. S., NICASTRO, D., GERISCH, G. & BAUMEISTER, W. 2002. Macromolecular architecture in eukaryotic cells visualized by cryoelectron tomography. *Science,* 298**,** 1209-13.

MILLAR, J. B. A., TOURNIER, S., GACHET, Y., BUCK, V. & HYAMS, J. S. 2004. Disruption of astral microtubule contact with the cell cortex activates a Bub1, Bub3, and Mad3-dependent checkpoint in fission yeast. *Molecular Biology of the Cell,* 15**,** 3345-3356.

MITCHISON, T. J. 1988. Microtubule dynamics and kinetochore function in mitosis. *Annual Review of Cell Biology,* 4**,** 527-49.

MITCHISON, T. J. & KIRSCHNER, M. W. 1985. Properties of the kinetochore in vitro. II. Microtubule capture and ATP-dependent translocation. *J Cell Biol,* 101**,** 766-77.

MOLLINARI, C., KLEMAN, J. P., JIANG, W., SCHOEHN, G., HUNTER, T. & MARGOLIS, R. L. 2002. PRC1 is a microtubule binding and bundling protein essential to maintain the mitotic spindle midzone. *Journal of Cell Biology,* 157**,** 1175-1186.

MORGAN, D. O. 1995. Principles of CDK regulation. *Nature,* 374**,** 131-4.

MORITZ, M. & AGARD, D. A. 2001. Gamma-tubulin complexes and microtubule nucleation. *Curr Opin Struct Biol,* 11**,** 174-81.

MOUNTAIN, V., SIMERLY, C., HOWARD, L., ANDO, A., SCHATTEN, G. & COMPTON, D. A. 1999. The kinesin-related protein, HSET, opposes the activity of Eg5 and cross-links microtubules in the mammalian mitotic spindle. *Journal of Cell Biology,* 147**,** 351-365.

MOUSAVI, S. A., MALEROD, L., BERG, T. & KJEKEN, R. 2004. Clathrin-dependent endocytosis. *Biochem J,* 377**,** 1-16.

MUKHERJEE, S., GHOSH, R. N. & MAXFIELD, F. R. 1997. Endocytosis. *Physiological Reviews,* 77**,** 759-803.

NAKAYAMA, K. I., HATAKEYAMA, S. & NAKAYAMA, K. 2001. Regulation of the cell cycle at the G1-S transition by proteolysis of cyclin E and p27Kip1. *Biochem Biophys Res Commun,* 282**,** 853-60.

NAKAYAMA, K. I. & NAKAYAMA, K. 2005. Regulation of the cell cycle by SCF-type ubiquitin ligases. *Semin Cell Dev Biol,* 16**,** 323-33.

NATHKE, I. S., HEUSER, J., LUPAS, A., STOCK, J., TURCK, C. W. & BRODSKY, F. M. 1992. FOLDING AND TRIMERIZATION OF CLATHRIN SUBUNITS AT THE TRISKELION HUB. *Cell,* 68**,** 899-910.

NEEF, R., PREISINGER, C., SUTCLIFFE, J., KOPAJTICH, R., NIGG, E. A., MAYER, T. U. & BARR, F. A. 2003. Phosphorylation of mitotic kinesin-like protein 2 by polo-like kinase 1 is required for cytokinesis. *J Cell Biol,* 162**,** 863-75.

NICKLAS, R. B. 1988. Chance encounters and precision in mitosis. *J Cell Sci,* 89 (Pt 3)**,** 283-5.

NISLOW, C., LOMBILLO, V. A., KURIYAMA, R. & MCINTOSH, J. R. 1992. A plus-end-directed motor enzyme that moves antiparallel microtubules in vitro localizes to the interzone of mitotic spindles. *Nature,* 359**,** 543-7.

NOGALES, E., WHITTAKER, M., MILLIGAN, R. A. & DOWNING, K. H. 1999. High-resolution model of the microtubule. *Cell,* 96**,** 79-88.

NORBURY, C. & NURSE, P. 1992. Animal-Cell Cycles and Their Control. *Annual Review of Biochemistry,* 61**,** 441-470.

O'BRIEN, L. L., ALBEE, A. J., LIU, L., TAO, W., DOBRZYN, P., LIZARRAGA, S. B. & WIESE, C. 2005. The Xenopus TACC homologue, maskin, functions in mitotic spindle assembly. *Molecular Biology of the Cell,* 16**,** 2836-47.

O'TOOLE, E. & MUELLER-REICHERT, T. 2009. Electron Tomography of Microtubule End-Morphologies in C. elegans Embryos. *In:* MCAINSH, A. D. (ed.) *Mitosis: Methods and Protocols.* Humana Press Inc, 999 Riverview Dr, Ste 208, Totowa, Nj 07512-1165 USA.

OHNUMA, K., YOMO, T., ASASHIMA, M. & KANEKO, K. 2006. Sorting of cells of the same size, shape, and cell cycle stage for a single cell level assay without staining. *Bmc Cell Biology,* 7**,** 25.

OKAMOTO, C. T., MCKINNEY, J. & JENG, Y. Y. 2000. Clathrin in mitotic spindles. *Am J Physiol Cell Physiol,* 279**,** C369-74.

OTTERSEN, O. P. 1989. Quantitative Electron-Microscopic Immunocytochemistry of Neuroactive Amino-Acids. *Anatomy and Embryology,* 180**,** 1-15.

PESET, I., SEILER, J., SARDON, T., BEJARANO, L. A., RYBINA, S. & VERNOS, I. 2005. Function and regulation of Maskin, a TACC family protein, in microtubule growth during mitosis. *J Cell Biol,* 170**,** 1057-66.

PETERMAN, E. J. G. & SCHOLEY, J. M. 2009. Mitotic Microtubule Crosslinkers: Insights from Mechanistic Studies. *Current Biology,* 19**,** R1089-R1094.

PETERS, J. M. 2002. The anaphase-promoting complex: proteolysis in mitosis and beyond. *Molecular Cell,* 9**,** 931-43.

PUERTOLLANO, R., RANDAZZO, P. A., PRESLEY, J. F., HARTNELL, L. M. & BONIFACINO, J. S. 2001. The GGAs promote ARF-dependent recruitment of clathrin to the TGN. *Cell,* 105**,** 93-102.

PULFORD, K., MORRIS, S. W. & TURTURRO, F. 2004. Anaplastic lymphoma kinase proteins in growth control and cancer. *Journal of Cellular Physiology,* 199**,** 330-58.

RIEDER, C. L. 1981. The structure of the cold-stable kinetochore fiber in metaphase PtK1 cells. *Chromosoma,* 84**,** 145-58.

RIEDER, C. L. 1982. The Formation, Structure, and Composition of the Mammalian Kinetochore and Kinetochore Fibre. *International Review of Cytology-a Survey of Cell Biology,* 79**,** 1-58.

RIEDER, C. L. 2005. Kinetochore fiber formation in animal somatic cells: dueling mechanisms come to a draw. *Chromosoma,* 114**,** 310-8.

RIEDER, C. L. 2011. Mitosis in vertebrates: the G2/M and M/A transitions and their associated checkpoints. *Chromosome Research,* 19**,** 291-306.

RIEDER, C. L. & KHODJAKOV, A. 1997. Mitosis and checkpoints that control progression through mitosis in vertebrate somatic cells. *Progress in cell cycle research,* 3**,** 301-12.

ROBBINS, E. & JENTZSCH, G. 1969. Ultrastructural changes in the mitotic apparatus at the metaphase-to-anaphase transition. *J Cell Biol,* 40**,** 678-91.

ROBBINS, E. & MARCUS, P. I. 1964. Mitotically Synchronized Mammalian Cells: A Simple Method for Obtaining Large Populations. *Science,* 144**,** 1152-3.

ROBINSON, M. S. 1994. The role of clathrin, adaptors and dynamin in endocytosis. *Curr Opin Cell Biol,* 6**,** 538-44.

ROBINSON, M. S. 2004. Adaptable adaptors for coated vesicles. *Trends in Cell Biology,* 14**,** 167-74.

ROBINSON, M. S. & BONIFACINO, J. S. 2001. Adaptor-related proteins. *Current Opinion in Cell Biology,* 13**,** 444-453.

ROTH, L. E., PIHLAJA, D. J. & SHIGENAKA, Y. 1970. Microtubules in the heliozoan axopodium. I. The gradion hypothesis of allosterism in structural proteins. *J Ultrastruct Res,* 30**,** 7-37.

ROYLE, S. J. 2006. The cellular functions of clathrin. *Cell Mol Life Sci,* 63**,** 1823-32.

ROYLE, S. J., BRIGHT, N. A. & LAGNADO, L. 2005. Clathrin is required for the function of the mitotic spindle. *Nature,* 434**,** 1152-7.

ROYLE, S. J. & LAGNADO, L. 2006. Trimerisation is important for the function of clathrin at the mitotic spindle. *J Cell Sci,* 119**,** 4071-8.

RUBINSTEIN, B., LARRIPA, K., SOMMI, P. & MOGILNER, A. 2009. The elasticity of motor-microtubule bundles and shape of the mitotic spindle. *Physical Biology,* 6.

SALMON, E. D. 1989. Cytokinesis in Animal Cells. *Current Opinion in Cell Biology,* 1**,** 541-547.

SALMON, E. D. & WOLNIAK, S. M. 1990. *Role of Microtubules in Stimulating Cytokinesis in Animal Cells*.

SANCAR, A., LINDSEY-BOLTZ, L. A., UNSAL-KACMAZ, K. & LINN, S. 2004. Molecular mechanisms of mammalian DNA repair and the DNA damage checkpoints. *Annual Review of Biochemistry,* 73**,** 39-85.

SCHIEL, J. A. & PREKERIS, R. 2010. Making the Final Cut - Mechanisms Mediating the Abscission Step of Cytokinesis. *Thescientificworldjournal,* 10**,** 1424-1434.

SCHMIDT, S., SCHNEIDER, L., ESSMANN, F., CIRSTEA, I. C., KUCK, F., KLETKE, A., JANICKE, R. U., WIEK, C., HANENBERG, H., AHMADIAN, M. R., SCHULZE-OSTHOFF, K., NURNBERG, B. & PIEKORZ, R. P. 2010. The centrosomal protein TACC3 controls paclitaxel sensitivity by modulating a premature senescence program. *Oncogene,* 29**,** 6184-92.

SCHOLEY, J. M., BRUST-MASCHER, I. & MOGILNER, A. 2003. Cell division. *Nature,* 422**,** 746-752.

SHARP, D. J., MCDONALD, K. L., BROWN, H. M., MATTHIES, H. J., WALCZAK, C., VALE, R. D., MITCHISON, T. J. & SCHOLEY, J. M. 1999. The bipolar kinesin, KLP61F, cross-links microtubules within interpolar microtubule bundles of Drosophila embryonic mitotic spindles. *Journal of Cell Biology,* 144**,** 125-138.

SHERR, C. J. & ROBERTS, J. M. 1999. CDK inhibitors: positive and negative regulators of G(1)-phase progression. *Genes & Development,* 13**,** 1501-1512.

SILLJE, H. H., NAGEL, S., KORNER, R. & NIGG, E. A. 2006. HURP is a Ran-importin beta-regulated protein that stabilizes kinetochore microtubules in the vicinity of chromosomes. *Curr Biol,* 16**,** 731-42.

SMITH, D. S. 1971. Significance of Cross-Bridges Between Microtubules and Synaptic Vesicles. *Philosophical Transactions of the Royal Society of London Series B-Biological Sciences,* 261**,** 395-&.

SMITH, D. S., JARLFORS, U., CAYER, M. L. & CAMERON, B. F. 1977. Structural Cross-Bridges Between Microtubules and Mitochondria in Central Axons of an Insect (Periplaneta-Americana). *Journal of Cell Science,* 27**,** 255-272.

SNYDER, J. A., GOLUB, R. J. & BERG, S. P. 1986. Role of non-kinetochore microtubules in spindle elongation in mitotic PtK1 cells. *Eur J Cell Biol,* 39**,** 373-9.

STRAIGHT, A. F. & FIELD, C. M. 2000. Microtubules, membranes and cytokinesis. *Current Biology,* 10**,** R760-R770.

SUBRAMANIAN, R., WILSON-KUBALEK, E. M., ARTHUR, C. P., BICK, M. J., CAMPBELL, E. A., DARST, S. A., MILLIGAN, R. A. & KAPOOR, T. M. 2010. Insights into antiparallel microtubule crosslinking by PRC1, a conserved nonmotor microtubule binding protein. *Cell,* 142**,** 433-43.

SULLIVAN, B. A., BLOWER, M. D. & KARPEN, G. H. 2001. Determining centromere identity: cyclical stories and forking paths. *Nat Rev Genet,* 2**,** 584-96.

SULLIVAN, K. F. 1988. STRUCTURE AND UTILIZATION OF TUBULIN ISOTYPES. *Annual Review of Cell Biology,* 4**,** 687-716.

TAHARA, H., YOKOTA, E., IGARASHI, H., ORII, H., YAO, M., SONOBE, S., HASHIMOTO, T., HUSSEY, P. J. & SHIMMEN, T. 2007. Clathrin is involved in organization of mitotic spindle and phragmoplast as well as in endocytosis in tobacco cell cultures. *Protoplasma,* 230**,** 1-11.

TAKEMURA, R., OKABE, S., UMEYAMA, T., KANAI, Y., COWAN, N. J. & HIROKAWA, N. 1992. Increased microtubule stability and alpha tubulin acetylation in cells transfected with microtubule-associated proteins MAP1B, MAP2 or tau. *J Cell Sci,* 103 (Pt 4)**,** 953-64.

TANAKA, T. U. 2010. Kinetochore-microtubule interactions: steps towards bi-orientation. *Embo Journal,* 29**,** 4070-4082.

TERADA, Y., TATSUKA, M., SUZUKI, F., YASUDA, Y., FUJITA, S. & OTSU, M. 1998. AIM-1: a mammalian midbody-associated protein required for cytokinesis. *EMBO J,* 17**,** 667-76.

TILNEY, L. G. 1971. How microtubule patterns are generated. The relative importance of nucleation and bridging of microtubules in the formation of the axoneme of Raphidiophrys. *J Cell Biol,* 51**,** 837-54.

TOOZE, J. & HOLLINSHEAD, M. 1992. Evidence that globular Golgi clusters in mitotic HeLa cells are clustered tubular endosomes. *Eur J Cell Biol,* 58**,** 228-42.

UHLMANN, F., LOTTSPEICH, F. & NASMYTH, K. 1999. Sister-chromatid separation at anaphase onset is promoted by cleavage of the cohesin subunit Scc1. *Nature,* 400**,** 37-42.

UHLMANN, F., WERNIC, D., POUPART, M. A., KOONIN, E. V. & NASMYTH, K. 2000. Cleavage of cohesin by the CD clan protease separin triggers anaphase in yeast. *Cell,* 103**,** 375-386.

VAN RIJNSOEVER, C., OORSCHOT, V. & KLUMPERMAN, J. 2008. Correlative light-electron microscopy (CLEM) combining live-cell imaging and immunolabeling of ultrathin cryosections. *Nat Methods,* 5**,** 973-80.

VITRE, B., COQUELLE, F. M., HEICHETTE, C., GARNIER, C., CHRETIEN, D. & ARNAL, I. 2008. EB1 regulates microtubule dynamics and tubulin sheet closure in vitro. *Nature Cell Biology,* 10**,** 415-21.

VOGEL, S. K., RAABE, I., DERELI, A., MAGHELLI, N. & TOLIC-NORRELYKKE, I. 2007. Interphase microtubules determine the initial alignment of the mitotic spindle. *Current Biology,* 17**,** 438-444.

WALCZAK, C. E., VERMA, S. & MITCHISON, T. J. 1997. XCTK2: a kinesin-related protein that promotes mitotic spindle assembly in Xenopus laevis egg extracts. *J Cell Biol,* 136**,** 859-70.

WARNER, F. D. 1976. Ciliary Inter-Microtubule Bridges. *Journal of Cell Science,* 20**,** 101-114.

WARREN, G. 1993. Membrane partitioning during cell division. *Annual Review of Biochemistry,* 62**,** 323-48.

WATERMAN-STORER, C. M., SANGER, J. W. & SANGER, J. M. 1993. Dynamics of organelles in the mitotic spindles of living cells: membrane and microtubule interactions. *Cell Motil Cytoskeleton,* 26**,** 19-39.

WATERS, J. C., COLE, R. W. & RIEDER, C. L. 1993. The Force-Producing Mechanism for Centrosome Separation During Spindle Formation in Vertebrates is Intrinsic to Each Aster. *Journal of Cell Biology,* 122**,** 361-372.

WATERS, J. C., SKIBBENS, R. V. & SALMON, E. D. 1996. Oscillating mitotic newt lung cell kinetochores are, on average, under tension and rarely push. *J Cell Sci,* 109 (Pt 12)**,** 2823-31.

WHEATLEY, S. P. & WANG, Y. 1996. Midzone microtubule bundles are continuously required for cytokinesis in cultured epithelial cells. *J Cell Biol,* 135**,** 981-9.

WILSON, H. J. 1969. Arms and Cross-Bridges on Microtubules in Mitotic Apparatus. *Journal of Cell Biology,* 40**,** 854-&.

WITT, P. L., RIS, H. & BORISY, G. G. 1980. Origin of kinetochore microtubules in Chinese hamster ovary cells. *Chromosoma,* 81**,** 483-505.

WITT, P. L., RIS, H. & BORISY, G. G. 1981. Structure of Kinetochore Fibers - Microtubule Continuity and Inter-Microtubule Bridges. *Chromosoma,* 83**,** 523-540.

WONG, J. & FANG, G. W. 2006. HURP controls spindle dynamics to promote proper interkinetochore tension and efficient kinetochore capture. *Journal of Cell Biology,* 173**,** 879-891.

WU, X. F., ZHAO, X. H., PUERTOLLANO, R., BONIFACINO, J. S., EISENBERG, E. & GREENE, L. E. 2003. Adaptor and clathrin exchange at the plasma membrane and trans-golgi network. *Molecular Biology of the Cell,* 14**,** 516-528.

WUHR, M., DUMONT, S., GROEN, A. C., NEEDLEMAN, D. J. & MITCHISON, T. J. 2009. How does a millimeter-sized cell find its center? *Cell Cycle,* 8**,** 1115-1121.

ZHENG, Y. 2010. A membranous spindle matrix orchestrates cell division. *Nat Rev Mol Cell Biol,* 11**,** 529-35.

ZHU, C. J., LAU, E., SCHWARZENBACHER, R., BOSSY-WETZEL, E. & JIANG, W. 2006. Spatiotemporal control of spindle midzone formation by

PRC1 in human cells. *Proceedings of the National Academy of Sciences of the United States of America,* 103**,** 6196-6201.